

IntechOpen

Power System Stability

Edited by Kenneth Eloghene Okedu



Power System Stability

Edited by Kenneth Elohene Okedu

Published in London, United Kingdom



IntechOpen





Supporting open minds since 2005



Power System Stability

<http://dx.doi.org/10.5772/intechopen.78487>

Edited by Kenneth Eloghene Okedu

Contributors

Salman Rezaei, Hui Cai, Enrique Zamora, Claudio Fuerte, Alejandro Pizano, Daniel Tomas Burillo, Kenneth Eloghene Okedu

© The Editor(s) and the Author(s) 2019

The rights of the editor(s) and the author(s) have been asserted in accordance with the Copyright, Designs and Patents Act 1988. All rights to the book as a whole are reserved by INTECHOPEN LIMITED. The book as a whole (compilation) cannot be reproduced, distributed or used for commercial or non-commercial purposes without INTECHOPEN LIMITED's written permission. Enquiries concerning the use of the book should be directed to INTECHOPEN LIMITED rights and permissions department (permissions@intechopen.com).

Violations are liable to prosecution under the governing Copyright Law.



Individual chapters of this publication are distributed under the terms of the Creative Commons Attribution 3.0 Unported License which permits commercial use, distribution and reproduction of the individual chapters, provided the original author(s) and source publication are appropriately acknowledged. If so indicated, certain images may not be included under the Creative Commons license. In such cases users will need to obtain permission from the license holder to reproduce the material. More details and guidelines concerning content reuse and adaptation can be found at <http://www.intechopen.com/copyright-policy.html>.

Notice

Statements and opinions expressed in the chapters are those of the individual contributors and not necessarily those of the editors or publisher. No responsibility is accepted for the accuracy of information contained in the published chapters. The publisher assumes no responsibility for any damage or injury to persons or property arising out of the use of any materials, instructions, methods or ideas contained in the book.

First published in London, United Kingdom, 2019 by IntechOpen

eBook (PDF) Published by IntechOpen, 2019

IntechOpen is the global imprint of INTECHOPEN LIMITED, registered in England and Wales,

registration number: 11086078, The Shard, 25th floor, 32 London Bridge Street

London, SE19SG – United Kingdom

Printed in Croatia

British Library Cataloguing-in-Publication Data

A catalogue record for this book is available from the British Library

Additional hard and PDF copies can be obtained from orders@intechopen.com

Power System Stability

Edited by Kenneth Eloghene Okedu

p. cm.

Print ISBN 978-1-78985-797-9

Online ISBN 978-1-78985-798-6

eBook (PDF) ISBN 978-1-83962-114-7

We are IntechOpen, the world's leading publisher of Open Access books Built by scientists, for scientists

4,100+

Open access books available

116,000+

International authors and editors

120M+

Downloads

151

Countries delivered to

Our authors are among the
Top 1%

most cited scientists

12.2%

Contributors from top 500 universities



WEB OF SCIENCE™

Selection of our books indexed in the Book Citation Index
in Web of Science™ Core Collection (BKCI)

Interested in publishing with us?
Contact book.department@intechopen.com

Numbers displayed above are based on latest data collected.
For more information visit www.intechopen.com



Meet the editor



Kenneth Eloghene Okedu was a Massachusetts Institute of Technology (MIT) Research Fellow in the department of Electrical and Computer Engineering, 2013 at Cambridge, Boston, USA. He obtained his Ph.D. from the Department of Electrical and Electronic Engineering, Kitami Institute of Technology, Hokkaido, Japan in 2012. He received his B.Sc. and M. Eng. degrees in Electrical and Electronic Engineering from the University of Port Harcourt, Nigeria in 2003 and 2007, respectively, where he was retained as a Faculty member from 2005 until the present day. He was also a visiting Faculty member to The Petroleum Institute, (ADNOAC), Abu Dhabi. He was also a visiting Faculty member to the Caledonian College of Engineering, Muscat, Oman (a university college with Glasgow Caledonian University, UK). He is presently a visiting Professor to the National University of Science and Technology (NUST), Muscat, Oman in the Department of Electrical and Computer Engineering. His research interests include power system stability, renewable energy systems, stabilization of wind farms using doubly fed induction generator variable speed wind turbine, augmentation and integration of renewable energy into power systems, grid frequency dynamics, wind energy penetration, FACTS devices and power electronics, renewable energy storage, hydrogen and fuel cells.

Contents

Preface	XIII
Section 1 Small Signal Stability and Dynamics	1
Chapter 1 Introductory Chapter: Power System Stability <i>by Kenneth Eloghene Okedu</i>	3
Chapter 2 Application of the Trajectory Sensitivity Theory to Small Signal Stability Analysis <i>by Enrique Arnoldo Zamora Cárdenas, Alejandro Pizano Martínez and Claudio Rubén Fuerte Esquivel</i>	15
Chapter 3 Power System Small-Signal Stability as Affected by Grid-Connected SmartPark <i>by Cai Hui</i>	33
Section 2 Power Oscillations and Electrical Infrastructures	53
Chapter 4 Power Oscillation Due to Ferroresonance and Subsynchronous Resonance <i>by Salman Rezaei</i>	55
Chapter 5 Effects of Climate Change in Electric Power Infrastructures <i>by Daniel Burillo</i>	75

Preface

This book contains two sections: Section 1 ‘Power System Stability - Small Signal Stability and Dynamics’ and Section 2 ‘Power System Stability - Power Oscillations and Electrical Infrastructures’. The book is relevant to academia and industries because it contains information from several authors with sound academic and industrial background in the field of power system technology.

Section 1 *Power System Stability - Small Signal Stability and Dynamics* - This section has three chapters. Chapter 1 introduces the book by giving an overview of power systems and stability criteria. This chapter presents a brief overview of power system structure, power system components and power system stability based on the swing equation. Stability studies considering synchronous generator models are also discussed. Steady state small disturbances and transient stability studies are also covered. The equal area criterion could be used for a quick prediction of stability. In this chapter, the various scenarios for stability analysis in a power network considering the equal area criterion for sudden change of load, maximum power limit, three phase fault at the sending end and three phase fault away from the sending end are presented for a one machine connected system to an infinite bus. Chapter 2 describes the application of the trajectory sensitivity theory to small signal stability analysis. This chapter presents a practical approach for assessing the stability of power system equilibrium points in real time based on the concept of trajectory sensitivity theory. The Mexican power system was used as a case study to evaluate and demonstrate the approach in a general sense and also to show how power systems could be effectively operated and control, considering effective energy management systems. Complementary information to those given by selective modal analysis is also obtained using this approach in order to find how the state variables that are linked with critical eigenvalues are affected by the parameters of the system. Also, this chapter provides solutions for how to evaluate the oscillatory behavior of a power system based on the parameters of the system. In Chapter 3, power system small signal stability as affected by grid-connected Smart Park is investigated. In this chapter, Damping Torque Analysis (DTA) was employed to examine the effects of the integration of smart charging station on the dynamic stability of transmission system. A single-machine infinite bus power system with a smart charging station was used in this work as an aggregate of several charging stations. The results obtained from DTA, according to this chapter, show that the damping ratio and optimal charging capacity should be considered in the design of the smart charging station. This is because the power system that can achieve the best maintained dynamic stability and damping ratio would be able to reach the crest value. The chapter further proposes the Phillips-Heffron model to design the stabilizer through regulation of the active and reactive power of the smart charging station, considering phase compensation methods. The power oscillation in tie-line can be suppressed more quickly and accurately with the help of the stabilizer, damping of the system oscillation under certain operating conditions.

Section 2 *Power System Stability- Power Oscillations and Electrical Infrastructures* - This section has two chapters. Power oscillations due to ferroresonance and Sub Synchronous Resonance (SSR) is presented in Chapter 4. Ferroresonance and SSR

are the phenomena that cause power oscillation of rotary systems. These ideas are presented in this chapter of the book. Ferroresonance is likely to occur due to traversing capacitance line of the system across non-linear area of transformer saturation curve as a result of several configurations such as; breaker failure, voltage transformer connected to grading capacitor circuit breaker, line and plant outage, and others. This chapter argues that changes in these variables cause misshaping of the waveforms and frequency differences between points in the network. In addition, the chapter addresses the issue of SSR causing an increase of the magnitudes of voltage and current in the network. Consequently, increasing the voltage causes saturation of iron core of the transformers or reactors, which leads to the occurrence of ferroresonance in the presence of series capacitance connected in the network. The effects of climate change in electric power infrastructures are addressed in Chapter 5. The chapter explains several ways in which electric power infrastructure has contributed to climate change, how climate change affects electric power infrastructures, the mitigation options to reduce its effects and adaptation methods to be implemented. The electricity infrastructures considered in this study include; the technologies of power generation, transmission lines, substations and loads. The following climate change categories were used; atmospheric greenhouse gas concentration levels, rising sea levels, changes in precipitation patterns, river flows, and extreme air temperatures. The United States of America desert southwest was considered as a case study. Based on long-term forecasting of infrastructure performance, various supply and demand side strategic options to maintain reliable operations, were considered as quantitative studies, in providing estimated vulnerability from heat waves.

Dr. Kenneth Eloghene Okedu
National University of Science and Technology
Glasgow Caledonian University
Muscat, Oman

Section 1

Small Signal Stability and Dynamics

Introductory Chapter: Power System Stability

Kenneth Eloghene Okedu

1. Technical Background

Among the various available energy systems, electrical energy is the most popular form, because it can be transported easily at high efficiency and reasonable cost from one place to the other. Electrical machine is a device that converts mechanical energy to electrical energy or vice versa. In the earlier case, the machine is known as a generator, while in the latter case, it is called a motor. The action of magnetic field is used in both machines for the conversion of energy from one form to the other. A power system is a network of components that is well designed and structured to efficiently transmit and distribute electrical energy produced by generators to locations where they are utilized. Generators, motors and other utility loads are connected by a power system.

1.1 Overview of power system structure

Earlier electric network stations supplied DC (direct current) power for lighting. The power was generated by DC generators and distributed by underground cables. Due to excessive power loss (I^2R), at low voltage, the energy delivered from such system could only travel short distances from their stations. When electrical transformers were invented, it created room for the prevalence of the AC (alternating current) system over the DC system. This is because the electrical transformers were able to raise the level of AC voltage for transmission and distribution. The AC system was further boosted with the invention of induction motors to replace DC motors. In addition, the merits of the AC system became apparent due to the fact that more power can be produced at higher voltages at convenience because of the lack of commutators in the AC generators [1].

As a result of the apparent advantages of the AC system, the single-phase and three-phase AC systems emerged. Many electric companies and independent power producers were operating at different frequencies. However, as the need for interconnection and parallel operation became imperative, a standard frequency of either 50 or 60Hz was adopted. Consequently, transmission voltages rose steadily and gave birth to extra high voltages (EHVs) mostly used for commercial purposes.

It may be more economical to convert EHV based on AC to EHV based on DC, when considering power transmission over long distances. This would involve transmission of the power via a two-line system and its inversion from DC back to AC at the other terminal. From the literature, it was reported that it is of more benefit to consider DC lines when the transmission distance is 500 km or more. It should be noted that DC lines possess no reactance and they have the ability of transferring more power considering the same conductor size than AC lines. The

main advantage of DC transmission is in the scenario where two remotely located large power systems are to be connected via a tie line. In this case, the DC tie line transmission system acts as a synchronous link between the two rigid power systems eliminating the instability problem that is common with the AC links. However, the production of harmonics that requires filtering in addition to the large amount of reactive power compensation required at both ends of the line is a major setback of the DC link system [1, 2].

The interconnection of the entire or overall network system is known as the power grid. When the system is divided into several geographical regions, they are called power pools. In an interconnected system or grid network, there exist fewer generators that are required as reserve for peak load and spinning reserve. The power grid allows energy penetration and transmission in a more reliable and economical way due to the fact that power can readily be transferred from one area to another. Most times, it may be cheaper for a power-producing company to purchase bulk power from the interconnected system instead of generating its own power.

1.2 Power system components

The major components of modern power systems are as follows.

1.2.1 Generators

Generators are one of the essential components of a power system. They produce electrical energy distributed by a power system. Most generators produce electrical energy by converting mechanical energy to electrical energy through the action of a magnetic field. The converted mechanical energy comes from a prime mover, which is a device that spins the generator. Steam and water turbines are some usual forms of prime movers, but in remote locations diesel engines have been used. Prime movers can operate based on many energy sources like water, coal, natural gas, oil, and nuclear energy. The prime mover based on water appears to be one of the best because it is non-polluting and requires no fuel cost. Nuclear power plants are expensive to construct and elaborate safety measures are required. Although, the cost of fuel is low and they are non-polluting energy sources in nature. Therefore, a combination of hydroelectric and nuclear power generators to power a given system would result in low fuel cost and the system can effectively run for long at full power rating. Coal plants are the most common source of electrical power generation because coal is a relatively cheap fuel. But it is unfortunate that coal is one of the most polluting fuel sources. Antipollution features are required in coal-fired plants in order to control pollution. Natural gas is a much cleaner and better energy source compared to coal. Its burning process emits little pollution and it is relatively cheaper. The main drawback of natural gas is that it is difficult to transport over long distances due to the fact that it is flammable in nature. Oil is much easier to transport; however, it is more polluting and more expensive than natural gas. Generally, coal, oil, and natural gas are the traditional non-renewable energy sources and this is a demerit of these energy sources. Wind, solar, biomass, and geothermal resources are other sources of energy that are renewable in nature; however, they are not yet economical when compared to the traditional sources of energy [1–3]. It should be noted that no source of electrical energy has all it takes to be perfect in producing electricity. All the available sources have their pros and cons and sometimes, a combination of two or more energy mix used in hybrid energy system is encouraged.

1.2.2 Transformers

Transformers are another major component of a power system that allows power to be transmitted with minimal loss over a long distance. Power is transferred with very high efficiency from one level of voltage to another level by the use of the transformers. In a transformer, the power transferred to the secondary side is almost the same as the primary side except for losses in the transformer. The product VI on the secondary side of the transformer is approximately same as that of the primary side. Hence, a step-up transformer of turns ratio a will reduce the secondary current by a ratio of $1/a$. Consequently, this will reduce losses in the line, which makes the transmission of power over long distance possible. Due to the insulation requirements and practical design problems, the generated voltage is limited to low values. Therefore, the step-up transformers are used for transmission of power, while at the receiving end of the transmission line, the step-down transformers are used to reduce the voltage to the required values for distribution and utilization. The transmitted power might undergo several transformations between generator and end users. Recent generators usually generate electrical power at voltages of 13.8–24 kV and transmission lines operate at very high voltages in order to reduce transmission losses. Electrical loads consume power at various voltage levels of 110 and 220 V, for residential and up to 4160 V for industrial applications [1, 2, 4].

1.2.3 Transmission and distribution (power lines)

The transmission and distribution lines are also known as power lines. They connect generators to loads, and transmit electrical power from one place to the other at minimal loss. Transmission lines also interconnect neighboring utilities, which permits not only economic dispatch of power within regions during steady-state or normal working conditions but also transfer of power between regions during emergencies. Thus, transmission lines are designed to efficiently transfer electrical power over long distances. In order to reduce resistive losses (I^2R) in the lines, they run at very high voltages [1, 2]. Upon receiving the power at the area of the end user, the transmission voltage is stepped down and the power is supplied through distribution lines to the final customer. Much less power is carried by the distribution lines and they operate for shorter distances at lower voltages without prohibitive losses compared to the transmission lines. The distribution system could be either overhead or underground. In recent times, the growth of the underground distribution has been rapid in modern residential constructions.

1.2.4 Loads

The loads on a power system are of different types. These loads could be electric motors, electric lighting, and others. However, a broad division of loads in a power system could be: industrial, commercial, and residential. The transmission system could serve very large industrial loads directly, while small industrial loads are served by the primary distribution network. The industrial loads are mainly composite loads and induction motors. The composite loads depend on voltage and frequency and they form bulk of the system load. Commercial and residential loads are made of lighting, heating, and cooling loads and they are independent of frequency with small or negligible reactive power consumption. Kilowatts or megawatts are used to define and express the real power of loads. The real power should be available to the end users and the magnitude of the load varies throughout the day. A composite of the demands made by various classes of utility end users gives

the daily load curve, and the greatest value of load during a period of 24 h is known as maximum or peak demand. Some key factors like the load factor (ratio of average load over a designated period of time to the peak load occurring in that period), utilization factor (ratio of maximum demand to the installed capacity), and plant factor (product of 8760 h and the ratio of annual energy generation to the plant capacity) help judge the performance of the system. In order for the a power system plant to operate economically, the load factor must be high, while the utilization and plant factors indicate how well the system capacity is usually operated and utilized [1, 5, 6].

1.2.5 Protection system

The protection system for a power system involves a variety of protective devices like current, voltage, power sensors, relays, fuses, and circuit breakers. The protective devices that are connected directly to the circuits are known as switchgears (e.g., instrument transformers, circuit breakers, disconnect switches, fuses, and lighting arresters). The presence of these devices is required in order to de-energize the power system either in scenarios of normal operation or in the occurrence of faults [1, 2]. The control house contains the associated control equipment and protective relays. There are basically two types of failures in a power system: overloads and faults. Overload conditions occur when the components in the power system are supplying more power than they were designed to carry safely. This scenario usually occurs when the total demand on the power system surpasses the capability of the system to supply power. Overloads often occur in new residential or industrial construction areas of the power system due to expansion. There are measures in place for the power system operator to immediately correct and control overload conditions due to the robustness of the system in order to avoid damage to the power network. On the other hand, fault conditions occur when one or more of the phases in a power system are shorted to ground or to each other (i.e., single phase to ground, three phases to ground, line to line, etc.). When a phase is open circuited, faults also occur in such situation. During periods of short circuit, very large currents flow and damage the entire power system if no measures are in place to quickly stop it. Faults must be cleared as quickly as possible in a power system when they occur, unlike overloads. For this reason, relays are employed to automatically open circuit breakers and isolate faulty areas; then, they are sensed in a power system [7, 8].

1.3 Power system stability

The tendency of a power system to develop restoring forces equal to or greater than the disturbing forces to maintain the state of equilibrium is known as stability. Power system stability problems are usually divided into two parts: steady state and transient. Steady-state stability refers to the ability of the power system to regain synchronism after small or slow disturbances like gradual power change. An extension of steady-state stability is dynamic stability [1]. Dynamic stability is concerned with small disturbances lasting for a long time with inclusion of automatic control devices. Transient stability deals with effects of large, sudden disturbances like fault occurrence, sudden outage of a line, and sudden application or removal of loads.

1.4 The swing equation

The position of the rotor axis and the resultant magnetic field axis is fixed under normal working conditions based on their relations. The angle between the two is

called the power angle or torque angle. During disturbances, the rotor accelerates/ decelerates with respect to the synchronously rotating air gap, thus a relative motion begins. The equation describing this relative motion is known as the swing equation given below [1, 2].

$$\frac{H}{\pi f_0} \frac{d^2 \delta}{dt^2} = P_m - P_e \quad (1)$$

where δ is the electrical radian; H is the per unit inertia constant; $P_m \wedge P_e$ are the per unit mechanical and electrical power, respectively; and f_0 is the frequency of the system. With δ in degrees, then

$$\frac{H}{180 f_0} \frac{d^2 \delta}{dt^2} = P_m - P_e \quad (2)$$

1.5 Stability studies for synchronous generator models

Consider a generator connected to a major substation of a very large system via a transmission line as shown below (**Figures 1** and **2**).

The substation bus voltage and frequency are assumed to remain constant (infinite bus). This is because its characteristics do not change regardless of power supplied or consumed by it. The generator is represented by a constant voltage behind the direct axis transient reactance X'_d . The node representing the generator terminal voltage V_g can be eliminated by converting the Y connected impedances to Δ with admittances as [1]

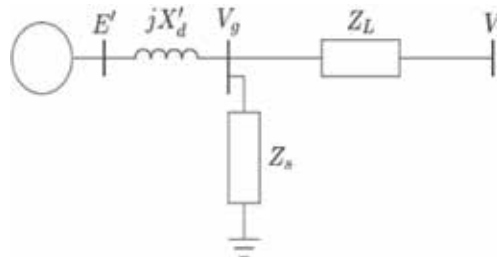


Figure 1.
 One machine connected to an infinite bus.

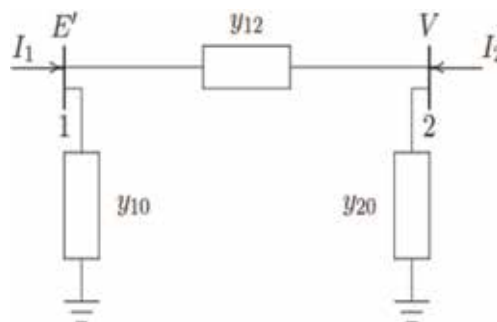


Figure 2.
 Equivalent circuit of one machine connected to an infinite bus.

$$\begin{aligned}
 y_{10} &= \frac{Z_L}{jX'_d Z_s + jX'_d Z_L + Z_L Z_s} \\
 y_{20} &= \frac{jX'_d}{jX'_d Z_s + jX'_d Z_L + Z_L Z_s} \\
 y_{12} &= \frac{Z_s}{jX'_d Z_s + jX'_d Z_L + Z_L Z_s}
 \end{aligned} \tag{3}$$

Writing the node equations for the above diagram gives

$$\begin{aligned}
 I_1 &= (y_{10} + y_{12})E' - y_{12}V \\
 I_2 &= -y_{12}E' + (y_{20} + y_{12})V
 \end{aligned} \tag{4}$$

The above equations can be written in terms of the bus admittance matrix

$$\begin{bmatrix} I_1 \\ I_2 \end{bmatrix} = \begin{bmatrix} Y_{11} & Y_{12} \\ Y_{21} & Y_{22} \end{bmatrix} \begin{bmatrix} E' \\ V \end{bmatrix} \tag{5}$$

The diagonal elements of the bus admittance are $Y_{11} = y_{10} + y_{12}$ and $Y_{22} = y_{20} + y_{12}$. The off-diagonal elements are $Y_{12} = Y_{21} = -y_{12}$. Expressing the voltages and admittances in polar form, the real power at node 1 is given by the following expression [1, 6].

$$\begin{aligned}
 P_e &= \Re[E'I_1^*] \\
 &= \Re[|E'|\angle\delta(|Y_{11}|\angle-\theta_{11}|E'|\angle-\delta + |Y_{12}|\angle-\theta_{12}|V|\angle 0)]
 \end{aligned} \tag{6}$$

In most systems, $Z_L \wedge Z_S$ are predominantly inductive. If all resistances are neglected, $\theta_{11} = \theta_{12} = 90^\circ$, then $Y_{12} = B_{12} = 1/X_{12}$. The simplified expression for power is

$$P_e = |E'||V||B_{12}|\cos(\delta - 90^\circ)$$

or

$$P_e = \frac{|E'||V|}{X_{12}}\sin\delta \tag{7}$$

The above equation is the simplified form of the power equation and basic to the understanding of all stability problems. The equation shows that the power transferred depends upon the transfer reactance and the angle between the two voltages. The curve P_e versus δ is known as the *power angle curve* shown below (**Figure 3**).

Maximum power is transferred at a displacement of 90° . The maximum power is called the steady-state stability limit and is given by:

$$P_{max} = \frac{|E'||V|}{X_{12}} \tag{8}$$

A further increase of the electrical power causes loss of synchronism, thus,

$$P_e = P_{max}\sin\delta \tag{9}$$

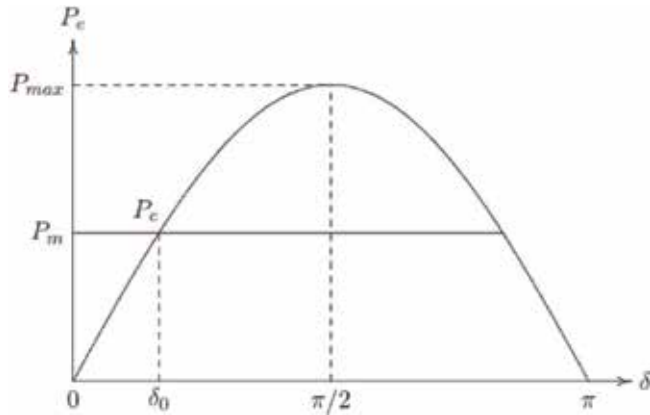


Figure 3.
 Power angle curve.

1.6 Small disturbances' steady-state stability

The steady-state stability refers to the ability of the power system to remain in synchronism when subjected to small disturbances. Substituting the electrical power in Eq. (9) into Eq. (1) gives [1]

$$\frac{H}{\pi f_0} \frac{d^2 \delta}{dt^2} = P_m - P_{max} \sin \delta \quad (10)$$

Solving the above differential equation results in synchronizing coefficient denoted by P_s . This coefficient plays an important part in determining the system stability and is given by:

$$P_s = \left. \frac{dP}{d\delta} \right|_{\delta_0} = P_{max} \cos \delta_0 \quad (11)$$

The natural frequency of the marginally stable oscillation is

$$\omega_n = \sqrt{\frac{\pi f_0}{H} P_s} \quad (12)$$

The damping power and dimensionless damping ratio are respectively defined as

$$P_d = D \frac{d\delta}{dt} \quad (13)$$

$$\zeta = \frac{D}{2} \sqrt{\frac{\pi f_0}{H P_s}} \quad (14)$$

where δ is the damping coefficient. The response time constant and settling time for the system are given respectively by

$$\tau = \frac{1}{\zeta\omega_n} = \frac{2H}{\pi f_0 D^2} \quad (15)$$

$$t_s \cong 4\tau \quad (16)$$

1.7 Transient stability

Transient stability studies involve the determination of whether or not synchronism is maintained after the machine has been subjected to severe disturbances. A method known as the equal area criterion can be used for a quick prediction of stability. Consider a synchronous machine connected to an infinite bus bar. The swing equation with damping neglected is given by

$$\frac{H}{\pi f_0} \frac{d^2\delta}{dt^2} = P_m - P_e = P_a \quad (17)$$

where P_a is the accelerating power. Scenarios for the equal area criterion are described below (**Figure 4**).

For a sudden step increase in input power, this is represented by the horizontal line P_{m1} . Since $P_{m1} > P_{e0}$, the accelerating power on the rotor is positive and the power angle δ increases. The excess energy stored in the rotor during the initial acceleration is [1]

$$\int_{\delta_0}^{\delta_1} (P_{m1} - P_e) d\delta = \text{area } abc = \text{area } A_1 \quad (18)$$

With increase in δ , the electrical power increases, and when $\delta = \delta_1$, the electrical power matches the new input power P_{m1} . For a situation where $P_m < P_e$, the rotor decelerates toward synchronous speed until $\delta = \delta_{max}$. The energy given up by the rotor as it decelerates back to synchronous speed is

$$\int_{\delta_0}^{\delta_1} (P_{m1} - P_e) d\delta = \text{area } abc = \text{area } A_1 \quad (19)$$

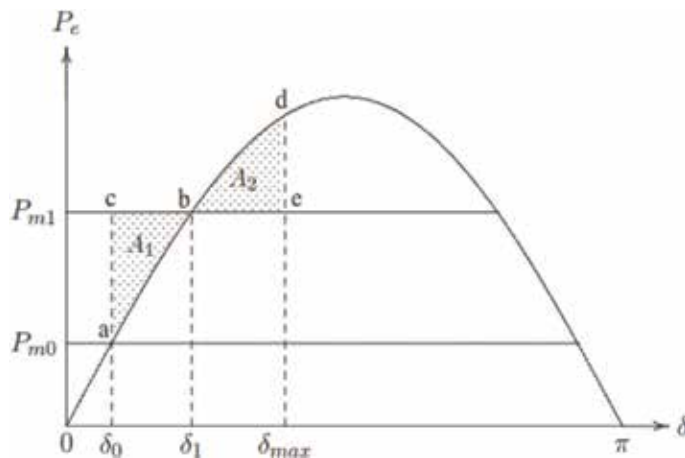


Figure 4.
Equal area criterion—sudden change of load.

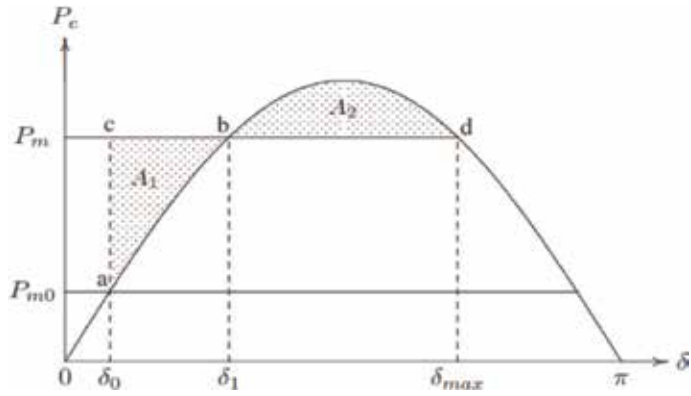


Figure 5.
 Equal area criterion—maximum power limit.

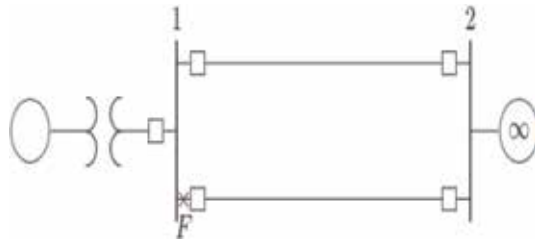


Figure 6.
 One machine system connected to infinite bus, three-phase fault at F, at the sending end.

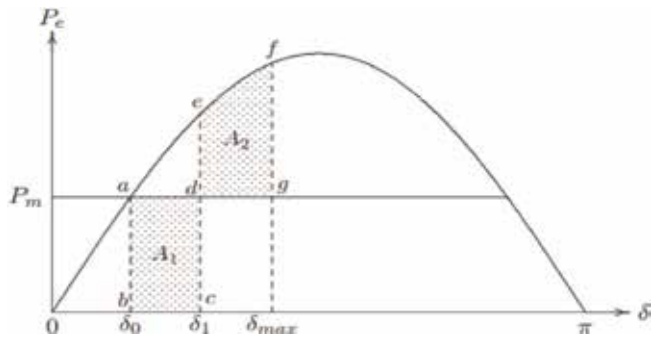


Figure 7.
 Equal area criterion for a three-phase fault at the sending end.

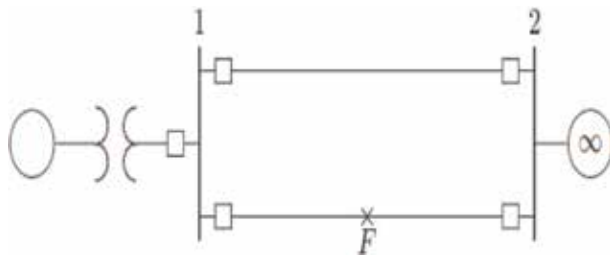


Figure 8.
 One machine system connected to infinite bus, three-phase fault at F, away from the sending end.

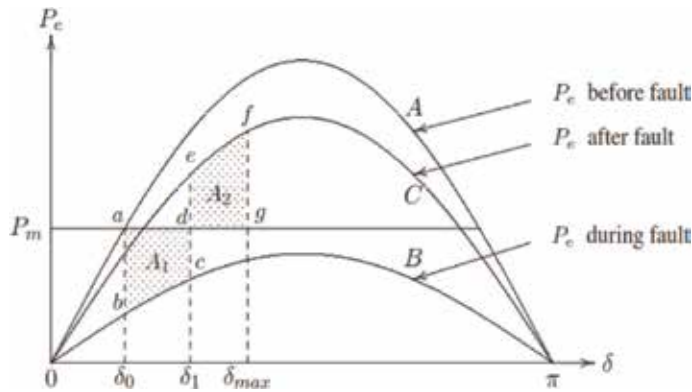


Figure 9. Equal area criterion for a three-phase fault away from the sending end.


The equal area criterion is used to determine the maximum additional power P_m which can be applied for stability to be maintained. This could be termed as application to sudden increase in power input as shown in **Figure 5**. **Figures 6–9** show the application to three-phase fault considering the equal area criterion [1].

Author details

Kenneth Eloghene Okedu
 Department of Electrical and Electronic Engineering, National University of
 Science and Technology (Glasgow Caledonian University), Muscat, Oman

*Address all correspondence to: kenokedu@yahoo.com

IntechOpen

© 2019 The Author(s). Licensee IntechOpen. This chapter is distributed under the terms of the Creative Commons Attribution License (<http://creativecommons.org/licenses/by/3.0>), which permits unrestricted use, distribution, and reproduction in any medium, provided the original work is properly cited. 

References

- [1] Saadat H. Power System Analysis. International Student Edition. New York, United States of America: McGraw-Hill; 2005
- [2] Chapman SJ. Electrical Machinery & Power System Fundamentals. New York, United States of America: McGraw-Hill; 2005
- [3] Painthankar YG, Bhide SR. Fundamentals of Power System Protection. New Delhi, India: Prentice Hall of India; 2003
- [4] Narendra K, Sanjiv K. Power System Analysis. West Sussex, United Kingdom: Global Media; 2010
- [5] Pdiyar KR. Power Systems Dynamics: Stability and Control. West Sussex, United Kingdom: Global Media; 2008
- [6] JanBialek M, Janusz Bumby J. Power Systems Dynamics: Stability and Control. 2nd ed. West Sussex, United Kingdom: John Wiley & Sons; 2009
- [7] Balakrishnan BM, Hewitson R. Leslie, Practical Power System Protection. United States: Newnes; 2005
- [8] Horowitz S, Phadke AG, Niemira JK. Power System Relaying. 4th ed. West Sussex, United Kingdom: John Wiley & Sons; 2013

Application of the Trajectory Sensitivity Theory to Small Signal Stability Analysis

*Enrique Arnaldo Zamora Cárdenas,
Alejandro Pizano Martínez
and Claudio Rubén Fuerte Esquivel*

Abstract

The security assessment of power systems represents one of the principal studies that must be carried out in energy control centers. In this context, small-signal stability analysis is very important to determine the corresponding control strategies to improve security under stressed operating conditions of power systems. This chapter details a practical approach for assessing the stability of power system's equilibrium points in real time based on the concept of trajectory sensitivity theory. This approach provides complementary information to that given by selective modal analysis: it determines how the state variables linked with the critical eigenvalues are affected by the system's parameters and also determines the way of judging how the system's parameters affect the oscillatory behavior of a power system. The WSCC 9-bus and a 190-buses equivalent system of the Mexican power system are used to demonstrate the generality of the approach as well as how its application in energy management systems is suitable for power system operation and control.

Keywords: small-signal stability, equilibrium points, selective modal analysis, Hopf bifurcation, parameter sensitivities

1. Introduction

Small-signal stability (SSS) is the ability of a power system to maintain synchronism when subjected to small disturbances such as small load and/or generation changes [1]. The analysis of SSS consists of assessing the stability of an equilibrium point (EP), as well as determining the most influential state variables in the stability of the operating point. For small enough disturbances, the system behavior can be studied via the theory of linear systems around an equilibrium point [2]. The stability of an EP is assessed by eigenvalue analysis (eigenanalysis) according to the Lyapunov criterion [3], which states that an EP will be stable in the small-signal sense, if all system eigenvalues of the system matrix are located on the left side of the complex plane. On the contrary, the EP will be unstable if at least one eigenvalue is located on the right side of the imaginary axis. In this context, the resulting dominant eigenvalue from the eigen-analysis is called the critical eigenvalue, and its association to the state variables is investigated by selective modal analysis (SMA)

[4, 5]. Based on the participation factors analysis (PFA), the SMA provides those state variables having the highest influence in the EP stability by means of their coupling to the critical eigenvalue [6, 7]. Since the system eigenvalues are directly related to its dynamic performance, different forms of instability in a power system can be studied by means of well-defined structures of eigenvalues which are called bifurcations.

The theory of bifurcations is a powerful mathematical tool based on eigen-analysis to assess the stability of EPs in nonlinear systems [8]. This theory consists of searching for specific eigenvalue structures associated to different instability forms that appear on power systems [9]. One of the most common local bifurcations that can appear in the power system operation is the Hopf bifurcation (HB), which occurs when the system matrix contains a pair of purely imaginary eigenvalues causing undamped oscillatory behavior [10–13]. Any parameter variation in the system may result in complicated behavior until the system stability changes. This point, where the stability changes, is defined as a bifurcation point. In this chapter the system loads are changed in order to analyze the stability of the EPs. The maximum load in a specific direction that a power system can provide before the appearance of a bifurcation point establishes the loading limit in that direction. Thus, the loading limit is directly associated with the stability margin of the system. The critical eigenvalue of an EP is used as an index of the stability margin. After a load change, an eigen-analysis permits us to assess the stability margin closeness. A small margin indicates closeness to a bifurcation point (instability).

SSS analysis is very important to determine the corresponding control strategies to improve security under stressed operating conditions of power systems. Control strategies employed in electric power systems are usually tested by means of an assessment of the stability improvement. Thus, the influence of parameters and components in the EP stability provides an insight to achieve the best control. In this context, the participation factors let us know the highest association between state variables and the critical eigenvalue dominating the EP stability [6, 7]. In this way, PFA allows the selection via the associated states to the critical eigenvalue of those components that will provide the best control in EP stability. Although the PFA selects the most sensitive states in the EP stability, it is not possible to identify in a direct form the most influential parameters, e.g., those most sensitive loads influencing the stability. In order to achieve this, the PFA must be combined with other methods providing parameter sensitivity features. In [14, 15] the authors combined the PFA and modal controllability of the weak damping oscillatory modes to obtain an optimal location of static VAR compensators (SVCs). In [16] the authors presented an approach to examine the effect of loads in the system stability by using participation factors and mode shape analysis. In Ref. [7], both a voltage stability analysis and a low-frequency oscillation analysis were performed by using the SSS analysis in the EPs. As the system faces increased loading conditions, bifurcation points appear, and the participating generators are identified by means of the most associated states obtained from the SMA.

This chapter presents an alternative method based on the trajectory sensitivity (TS) theory [17, 18] to investigate the stability of the EPs by using a time-domain simulation. In this approach which will be referred to as selective modal analysis and trajectory sensitivities (SMA-TS), the TS were computed with respect to the load parameters; therefore, besides the stability assessment and the participating states, this approach also has the ability to identify those most sensitive load parameters influencing the critical states. The stability assessment consists of just examining the TS oscillations. However, the stability analysis of the EP is never perturbed. The TS oscillations required for the stability assessment are produced by means of the initial condition values selected for the sensitivity variables. The

SMA-TS approach uses an index of sensitivity quantification, which facilitates identifying the influence of the system loads around the HB points. The index allows to rank the power system loads in order to predict the most critical loading directions toward a B point. Its application is suitable to monitoring in real time the power system operation and improve the security. The results of the study cases of two real systems, i.e., WSCC 9-bus and an equivalent of the Mexican power system of 190-buses, are used to show the performance and applicability of the proposed approach.

2. Trajectory sensitivity theory

An electric power system can be represented analytically by a set of differential-algebraic equations (DAEs), as given by (1), where x is a n -dimensional vector of dynamic state variables with initial conditions $x(t_0) = x_0$, y is a m -dimensional vector of instantaneous state (algebraic) variables, (usually the real and imaginary parts or the magnitudes and phase angles of the complex node voltages) with initial conditions $y(t_0) = y_0$, and β is a set of time-invariant parameters of the system. The dynamics of the equipment, e.g., generators and controls, is explicitly modeled by the set of differential equations through the function $f(\cdot)$. The set of algebraic equations $0 = g(\cdot)$ represents the stator algebraic equations and mismatch power flow equations at each node:

$$\begin{aligned} \dot{x} &= f(x, y, \beta) & f : \mathfrak{R}^{n+m+p} &\rightarrow \mathfrak{R}^n \\ 0 &= g(x, y, \beta) & g : \mathfrak{R}^{n+m+p} &\rightarrow \mathfrak{R}^m \\ x &\in X \subset \mathfrak{R}^n & y &\in Y \subset \mathfrak{R}^m & \beta &\in \beta \subset \mathfrak{R}^p. \end{aligned} \quad (1)$$

2.1 Analytical formulation

Let β_0 be the nominal values of β , and assume that the nominal set of DAEs $\dot{x} = f(x, y, \beta_0)$, $0 = g(x, y, \beta_0)$ has a unique nominal trajectory solution $x(t, x_0, y_0, \beta_0)$ and $y(t, x_0, y_0, \beta_0)$ over $t \in [t_0, t_{end}]$, where t_0 and t_{end} are the initial and final times, respectively, of the study time period. Thus, for all β sufficiently close to β_0 , the set of DAEs (1) has a unique perturbed trajectory solution $x(t, x_0, y_0, \beta)$ and $y(t, x_0, y_0, \beta)$ over $t \in [t_0, t_{end}]$ that is close to the nominal trajectory solution. This perturbed solution is given by (2) and (3) [19, 20]:

$$x(\cdot) = x_0 + \int_{t_0}^{t_{end}} f(x(\cdot), y(\cdot), \beta) ds \quad (2)$$

$$0 = g(x(\cdot), y(\cdot), \beta). \quad (3)$$

The sensitivities of the dynamic and algebraic state vectors with respect to a chosen system's parameter, $x_\beta = dx(\cdot)/d\beta$ and $y_\beta = dy(\cdot)/d\beta$, at a time t along the trajectory are obtained from (4) and (5), which in turn are obtained from the partial derivative of (2) and (3) with respect to β :

$$\frac{dx(\cdot)}{d\beta} = \int_{t_0}^{t_{end}} \left(\frac{\partial f(\cdot)}{\partial x} \frac{dx}{d\beta} + \frac{\partial f(\cdot)}{\partial y} \frac{dy}{d\beta} + \frac{\partial f(\cdot)}{\partial \beta} \right) ds \quad (4)$$

$$0 = \frac{\partial g(\cdot)}{\partial x} \frac{dx}{d\beta} + \frac{\partial g(\cdot)}{\partial y} \frac{dy}{d\beta} + \frac{\partial g(\cdot)}{\partial \beta}. \quad (5)$$

Lastly, the smooth evolution of the sensitivities along the trajectory (6) and (7) is obtained by differentiating (4) and (5) with respect to t :

$$\dot{x}_\beta = \frac{\partial f(\cdot)}{\partial x} \frac{\partial x}{\partial \beta} + \frac{\partial f(\cdot)}{\partial y} \frac{\partial y}{\partial \beta} + \frac{\partial f(\cdot)}{\partial \beta} \equiv f_x x_\beta + f_y y_\beta + f_\beta; \quad x_\beta(t_0) = 0 \quad (6)$$

$$0 = \frac{\partial g(\cdot)}{\partial x} \frac{\partial x}{\partial \beta} + \frac{\partial g(\cdot)}{\partial y} \frac{\partial y}{\partial \beta} + \frac{\partial g(\cdot)}{\partial \beta} \equiv g_x x_\beta + g_y y_\beta + g_\beta; \quad y_\beta(t_0) = 0 \quad (7)$$

where $f_x, f_y, f_\beta, g_x, g_y,$ and g_β are time-varying matrices computed along the system trajectories.

3. Trajectory sensitivity analysis

3.1 Sensitivity discretization

TS computation is obtained by means of the sequential solution of the nonlinear DAE system (1) and the linear time-varying DAE system (6) and (7). By applying the trapezoidal rule to algebraize the differential equations, both DAE systems are converted into the following systems of algebraic difference Eqs. (8)–(11).

$$F_1(\cdot) = x^{k+1} - x^k - \frac{\Delta t}{2} (f^{k+1} + f^k) = 0 \quad (8)$$

$$F_2(\cdot) = g^{k+1} = 0 \quad (9)$$

$$F_3(\cdot) = x_\beta^{k+1} - x_\beta^k - \frac{\Delta t}{2} (f_x^{k+1} x_\beta^{k+1} + f_y^{k+1} y_\beta^{k+1} + f_\beta^{k+1} + f_x^k x_\beta^k + f_y^k y_\beta^k + f_\beta^k) = 0 \quad (10)$$

$$F_4(\cdot) = g_x^{k+1} x_\beta^{k+1} + g_y^{k+1} y_\beta^{k+1} + g_\beta^{k+1} = 0 \quad (11)$$

where Δt is the integration time step and the superscript k is an index for the time instant t_k at which variables and functions are evaluated, e.g., $x^k = x(t_k)$ and $f^k = f(x^k, y^k)$.

3.2 Linear sensitivity computation

Once algebraized both DAE systems (8)–(11), the Newton-Raphson (NR) algorithm is used to provide an approximate solution of the algebraized nonlinear systems (8) and (9). In this case, the resulting linearized system $J^i \Delta X^i = -F(X)^i$, whose representation in expanded form is given in (12), provides the approximate solution $\Delta X^i = [\Delta x^k \ \Delta y^k]^T$, which is updated at each NR i th iteration, i.e., $[x^{k+1} = x^k + \Delta x^k \quad y^{k+1} = y^k + \Delta y^k]^T$, until a selected convergence criterion is satisfied. Note also that J is the Jacobian matrix resulting of the linearization around an EP.

The initial guess $[x_0^{k+1} = x^k \quad y_0^{k+1} = y^k]^T$ is used to start the NR algorithm from given values $[x^k \quad y^k]^T$:

$$\underbrace{\begin{bmatrix} I - \frac{\Delta t}{2} f_x^{k+1} & -\frac{\Delta t}{2} f_y^{k+1} \\ g_x^{k+1} & g_y^{k+1} \end{bmatrix}}_{J^i} \underbrace{\begin{bmatrix} \Delta x^k \\ \Delta y^k \end{bmatrix}}_{\Delta X^i} = - \underbrace{\begin{bmatrix} F_1(\cdot) \\ F_2(\cdot) \end{bmatrix}}_{F(\cdot)^i}. \quad (12)$$

Once the states have been computed for a new time step, the TS can be calculated. To do this, the linear time-varying systems (10) and (11) rearranged as indicated in (13) should be evaluated with the recently computed states and solved for the TS $\begin{bmatrix} x_\beta^{k+1} & y_\beta^{k+1} \end{bmatrix}^T$:

$$\underbrace{\begin{bmatrix} I - \frac{\Delta t}{2} f_x^{k+1} & -\frac{\Delta t}{2} f_y^{k+1} \\ g_x^{k+1} & g_y^{k+1} \end{bmatrix}}_J \underbrace{\begin{bmatrix} x_\beta^{k+1} \\ y_\beta^{k+1} \end{bmatrix}}_S = \underbrace{\begin{bmatrix} x_\beta^k + \frac{\Delta t}{2} (f_x^k x_\beta^k + f_y^k y_\beta^k + f_\beta^k + f_\beta^{k+1}) \\ -g_\beta^{k+1} \end{bmatrix}}_B. \quad (13)$$

It is very important to note that at each time step Δt , the solution of (13) for the TS calculation x_β^{k+1} and y_β^{k+1} uniquely requires a forward/backward substitution, which represents a very small computational burden [17]. This is because the coefficient matrix on the left side of (13) corresponds to the Jacobian matrix already factored used in the final NR iteration to solve (12).

3.3 Multiparameter sensitivity

It is clear that the solution of the linear time-varying system (13) uses the same Jacobian matrix already factored for solving the TS calculation with respect to any β parameter. Taking advantage of this observation, the solution approach described in Section 3.2 can be directly extended to provide an efficient linear computation of multiparameter trajectory sensitivities, as shown in (14). In this case, it is only necessary to carry out N_p forward/backward substitutions to calculate all TS vectors with respect to N_p parameters of the system, i.e., $x_{\beta_i}^{k+1}$ and $y_{\beta_i}^{k+1} \forall i = 1, \dots, N_p$, where S is a $(n+m) \times N_p$ sensitivity matrix whose N_p columns are the $(n+m)$ -dimension TS vectors with respect to N_p parameters:

$$\underbrace{\begin{bmatrix} I - \frac{\Delta t}{2} f_x^{k+1} & -\frac{\Delta t}{2} f_y^{k+1} \\ g_x^{k+1} & g_y^{k+1} \end{bmatrix}}_J \underbrace{\begin{bmatrix} S_{\beta_1} & S_{\beta_2} & \dots & S_{\beta_{N_p}} \end{bmatrix}}_S = \underbrace{\begin{bmatrix} B_{\beta_1} & B_{\beta_2} & \dots & B_{\beta_{N_p}} \end{bmatrix}}_B. \quad (14)$$

3.4 Sensitivity quantification

As numerically demonstrated in [19–23], when the system approaches an unstable operation condition, the sensitivities of state trajectories have more rapid changes in magnitudes and larger excursions than the state trajectories. Hence, as the system approaches its stability boundary, the TS approach infinity [19]. In this sense, it is possible to associate the sensitivity information with the stability level of the system for a particular system parameter. For this purpose, an Euclidian norm of the trajectory sensitivity vector, referred to as a sensitivity norm, is proposed in [23] as a measure of proximity to instability. This sensitivity norm also permits the computation of the critical parameters whose variations steer the system much faster to an unstable operation condition. In this chapter, such a sensitivity norm is used to provide a time-varying index of proximity to oscillatory instability for a n_g -generator system defined at each integration time step Δt , as shown in (15), which by computing sensitivities of rotor angle and speed trajectories with respect to active power loads measures the load power's effect on the system's small-signal stability:

$$SN_\rho(t_k) = \sqrt{\sum_{m=1}^{n_g} \left(\left(\frac{\partial \delta_m(t_k)}{\partial \beta_\rho} - \frac{\partial \delta_j(t_k)}{\partial \beta_\rho} \right)^2 + \left(\frac{\partial \omega_m(t_k)}{\partial \beta_\rho} \right)^2 \right)} \quad \forall \rho = 1, \dots, Np, \quad (15)$$

where j denotes the reference generator.

In this case, the time evolution of sensitivities is necessary to quantify the loads' influence on the possible occurrence of an oscillatory instability, where the highest values of the sensitivity norms SN_ρ indicate the most sensitive loads for the EP's stability. Thus, it should be noted that the critical load powers are those with the largest values of sensitivity index within the integration period, not the largest final value.

Note that this sensitivity norm has been successfully applied before for developing suitable approaches to improve the transient stability of power systems, e.g., for the estimation of the critical clearing time of a faulted system [23], the best possible location of FACTS controllers for transient stability enhancement [24–26], and the thyristor-controlled series compensator (TCSC) control design to enhance transient stability [27].

3.5 Sensitivity initial conditions

The analysis of a stationary operating point based on this approach is performed by keeping the corresponding EP constant during the whole simulation. Thus, during this simulation period with no perturbation, which is considered from the instant of time t_0 and the infinity t_∞ , the TS also remain into the same stationary behavior established at nonzero constant values $x_\beta(t_\infty) \neq 0$ and $y_\beta(t_\infty) \neq 0$. However, as our approach is based on catching the oscillatory behavior of trajectory sensitivities, the values $x_\beta(t_0) = y_\beta(t_0) = 0$ are arbitrarily used as the initial conditions of the sensitivity variables. Then, such an initial condition perturbation starts an oscillatory behavior on the TS, whose transient period evolves from the perturbed initial condition $x_\beta(t_0) = y_\beta(t_0) = 0$ to the stationary final condition $(x_\beta(t_\infty), y_\beta(t_\infty))$. Such a transient behavior provides the necessary TS information to assess the influence of the states and parameters (load powers) in the stability of the analyzed EP. It is important to note that because of the EP stay undisturbed during the TS transient simulation, f_x, f_y, f_β and g_x, g_y, g_β are considered time-invariant matrices in the linear sensitivity model (13), where only the TS $\begin{bmatrix} x_\beta^{k+1} & y_\beta^{k+1} \end{bmatrix}^T$ are time-varying. Thus, a reduced computational burden is required for the TS simulation.

3.6 Approach for small-signal stability with trajectory sensitivities

The application of the SMA-TS approach to assess the effect of a set of system's parameters on the stability of the equilibrium points is summarized as follows:

Step 1. For an arbitrary set of fixed parameters β , the system's equilibrium is computed by solving the set of nonlinear algebraic equations (1) for x and y considering $\dot{x} = 0$. The NR algorithm is applied to obtain this solution given by the values x_e and y_e that satisfy $0 = f(x_e, y_e, \beta)$ and $0 = g(x_e, y_e, \beta)$.

Step 2. Based on the Schur and the implicit function theorems [28, 29], compute the reduced Jacobian matrix $J_R = \left(f_x - f_y g_y^{-1} g_x \right) \Big|_{(x_e, y_e, \beta)}$ that has the same dynamic and algebraic properties of the system's Jacobian matrix.

Step 3. Determine the critical eigenvalues of J_R , and perform a SMA to identify the associate state variables.

Step 4. Compute the sensitivities of associated state variables with respect to the selected system's parameters (load powers) at the equilibrium point, $x_\beta^{t \rightarrow \infty}$ and $y_\beta^{t \rightarrow \infty}$, by solving (16). The integration process is started with initial conditions $x_\beta(t_0) = y_\beta(t_0) = 0$ for the parameter sensitivities, while the state and algebraic variables are set at their equilibrium values during the solution process. The time evolution of sensitivities is computed under the assumption that a very small perturbation is carried out in the system such that the state and algebraic variables are infinitesimally perturbed; their values, therefore, can be considered constant during the computation of the sensitivity index. These assumptions permit us to directly relate our proposal to the theory of trajectory sensitivities:

$$\underbrace{\begin{bmatrix} I - \frac{\Delta t}{2} f_x & -\frac{\Delta t}{2} f_y \\ g_x & g_y \end{bmatrix}}_J \Big|_{(x_e, y_e, \beta)} \underbrace{\begin{bmatrix} x_\beta^{k+1} \\ y_\beta^{k+1} \end{bmatrix}}_S = \underbrace{\begin{bmatrix} x_\beta^k + \frac{\Delta t}{2} (f_x x_\beta^k + f_y y_\beta^k + 2f_\beta) \\ -g_\beta \end{bmatrix}}_B \quad (16)$$

Step 5. Quantify the interaction between the system parameters and the associated state variables by using the sensitivity index (15). Since this index is a function of the sensitivities of those state variables directly associated with the oscillatory modes and the critical eigenvalues, it can be used to quantify the effect of the i th parameter on these variables. In this case, the highest values of the sensitivity norms indicate the most sensitive parameters. Furthermore, the sensitivity index value increases as the system is approaching an oscillatory stability problem.

4. Small-signal stability analysis

This section presents the analysis of the TS applied on assessing the SSS analysis. The effectiveness of the SMA-TS approach is numerically tested by analyzing the WSCC 9-buses and 3-generator systems [7] and a reduced equivalent system corresponding to the Mexican power system consisting of 190-buses with 46 generators. For the purpose of the studies presented in this section, the system generators are represented by means of the two-axis model with a simple fast exciter loop containing max/min ceiling limits. For this case the system loads are represented by means of the constant power load model; however, the generality of the method allows to consider any load model.

4.1 Modal analysis WSCC system

In this subsection the conventional modal analysis is employed in order to investigate the small-signal stability of the WSCC power system, whose diagram is given in **Figure 1**. **Table 1** presents the modal analysis for different EPs as the active power at bus 5 is increasing.

SSS and SMA were performed to investigate the different operating points corresponding to the different levels of loading. Eigen-analysis revealed the SSS of EPs, whereas participation factors were used to identify the most associated states to the critical eigenvalue at each EP, as given in **Table 1**. The first column represents the load changes at bus 5. The second column presents the critical eigenvalue for the EP. The third column presents the most associated states to the critical mode

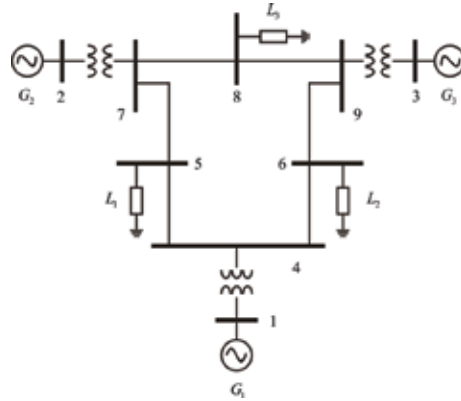


Figure 1.
WSCC 9-buses, 3-generators.

$P_{L5}(pu)$	λ_{crit}	Associated states	PF
4.2	$-0.5085 \pm 7.3001i$	$\omega_2, \delta_2, E'_{d2}, E'_{q1}, E_{fd1}$	1.0, 0.99, 0.18, 0.18, 0.16
4.3	$-0.5395 \pm 6.8512i$	$\omega_2, \delta_2, E'_{d2}, E'_{q1}, E_{fd1}$	1.0, 0.99, 0.28, 0.39, 0.35
4.4	$-0.0305 \pm 6.1462i$	$\delta_2, \omega_2, E'_{d2}, E'_{q1}, E_{fd1}$	1.0, 0.99, 0.46, 0.99, 0.83
4.5	$0.7064 \pm 5.8935i$	$E'_{q1}, \delta_2, \omega_2, E_{fd1}, E'_{d2}$	1.0, 0.85, 0.85, 0.79, 0.38
4.6	$1.5118 \pm 5.7190i$	$E'_{q1}, \delta_2, \omega_2, E_{fd1}, E'_{d2}$	1.0, 0.81, 0.80, 0.76, 0.32
4.7	$2.6677 \pm 5.5020i$	$E'_{q1}, \delta_2, \omega_2, E_{fd1}, E'_{d2}$	1.0, 0.79, 0.78, 0.74, 0.28
4.8	$5.3798 \pm 4.5835i$	$E'_{q1}, \delta_2, \omega_2, E_{fd1}, E'_{d2}$	1.0, 0.77, 0.75, 0.76, 0.26

Table 1.
Selective modal analysis.

(eigenvalue), obtained by selecting the highest magnitudes of participation factors, which are given in the fourth column in the table.

As the load embedded at bus 5 increased, the stability of the new EP decreased with respect to the previous one. The power system oscillatory instability called the HB was detected when the load changed from 4.4 to 4.5 p.u. The SMA around the HB revealed generator 2 as the most participative in the unstable EP. It is important to observe in **Table 1** that generator 2 is the most associated with the critical eigenvalues for all analyzed EPs.

5. Trajectory sensitivity analysis: WSCC system

In order to test the proposed method based on TS to assess the EP stability, operating points before and after the HB point were investigated [30]. As the active power increases at bus 5, as was performed in [7], the system proximity to the bifurcation points is assessed by using the analysis of TS. The rotor angle and speed sensitivities with respect to the load active powers were traced and observed through the time. The TS oscillations provide qualitative information used to investigate the proximity to bifurcation points. Such sensitivity oscillations agree with the critical eigenvalues obtained by the SMA at each EP, as reported in **Table 1**. Thus, the oscillatory behavior in the TS indicates that the EP is around the HB point

and the critical eigenvalue of the EP is complex. The proximity to the HB point is qualitatively assessed by observing the damping of the TS oscillation, i.e., if the TS oscillation is positively damped, the system is operating before the HB (stable EP); however, if the TS oscillation is undamped, the system operates after the HB (unstable EP).

Multiparameter sensitivity is used to assess the load influence around the HB. Such an assessment requires only one simulation to identify the critical loading direction on approaching HB. The TS computation in all cases started from second one onward.

5.1 Stability around the Hopf bifurcation

In order to qualitatively analyze the oscillatory behavior of the EPs around the HB, **Figures 2–4** show the TS of the dynamic variables (generator states) with respect to the load embedded at bus 5. The oscillation waveforms and their peak

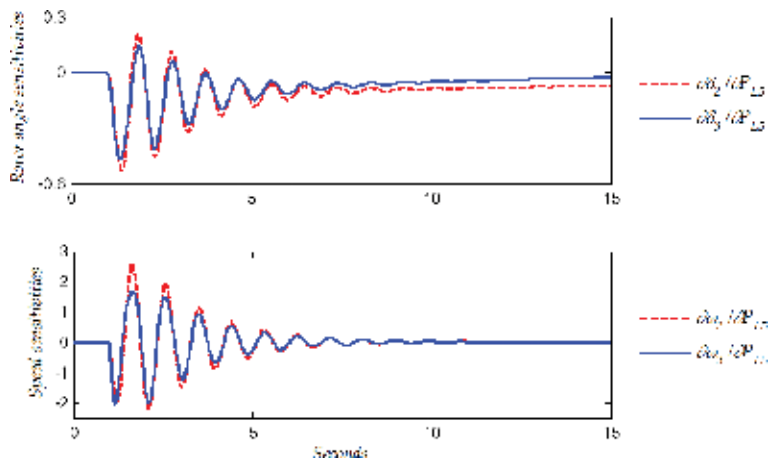


Figure 2. Parameter sensitivities with respect to $P_{L5} = 4.3 \text{ pu}$, $\lambda_{crit} = -0.5395 \pm 6.8512i$, [30].

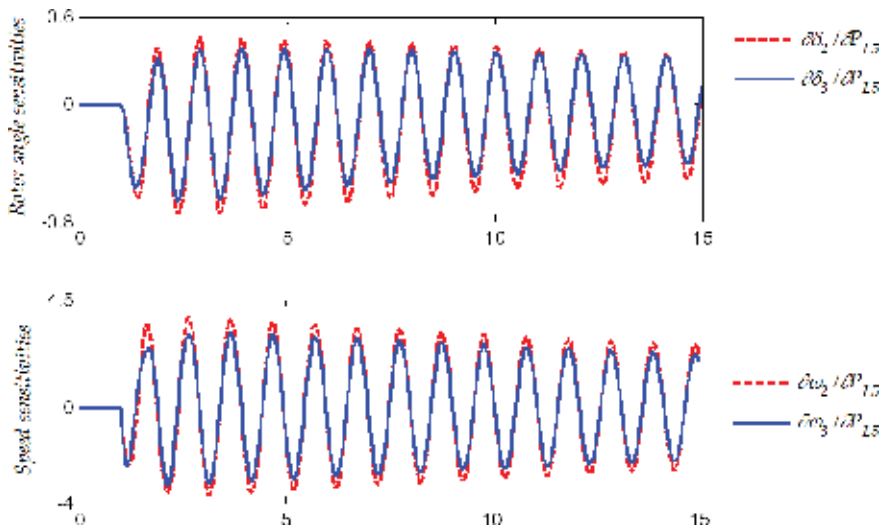


Figure 3. Parameter sensitivities with respect to $P_{L5} = 4.4 \text{ pu}$, $\lambda_{crit} = -0.0305 \pm 6.1462i$, [30].

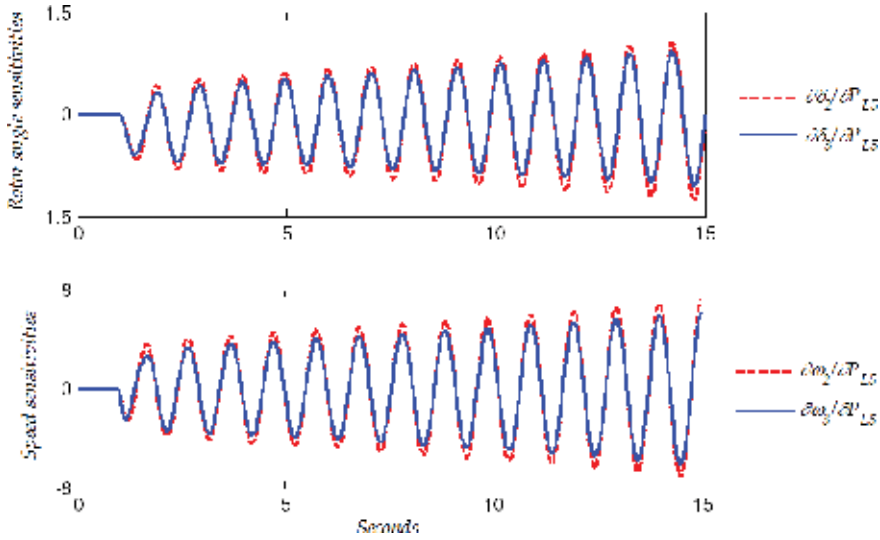


Figure 4. Parameter sensitivities with respect to $P_{L5} = 4.41$ pu, $\lambda_{crit} = 0.0462 \pm 6.1105i$, [30].

values allow to assess and to determine the EP stability as well as its most associated states because of the loading increase. **Figure 2** shows the TS with respect to $P_5 = 4.3$ pu where the sensitivity oscillations are damped. This agrees with the corresponding critical eigenvalue $\lambda_{crit} = -0.5395 \pm 6.8512i$ which indicates that the system is not too close to the HB point. However, **Figure 3** shows sensitivity oscillations with a very small damping when $P_5 = 4.4$ pu, where the critical eigenvalue $\lambda_{crit} = -0.0305 \pm 6.1462i$ is very close to the imaginary axis in the complex plane and hence close to a HB point. This means that a very small variation in the load parameter could steer the system to operate in an unstable EP. **Figure 4** shows the TS behavior when $P_5 = 4.41$ pu, which corresponds to an unstable EP after a HB point. From **Figures 2–4**, it is clear that the highest peaks of the TS oscillations in all cases correspond to generator 2. Therefore, such a generator is the most influential in the EP stability according to the most associated states reported in **Table 1**. However, this correspondence between associated states and TS is not always kept as will be shown in the upcoming sections.

It should be noted from the figures that the load demand at bus 5 increases as the peaks of TS are higher. This qualitative information indicates that such a load variation has a major impact in the load angle and speed of generator 2 (red lines) than the state variables associated with generator 3 (blue lines). Note that this line of reasoning also applies for unstable EPs, i.e., after passing the HB point, as can be observed in **Figure 4**. Thus, a short simulation in time is enough for this approach to determine the EP stability and their most influencing generators.

5.2 Simulation efficiency

In order to observe the effect of the time-step integration Δt in the computational burden, **Figure 5** shows the rotor angle sensitivity of generator 2 with respect to the active power embedded at bus 5. Such a trajectory was computed using three different time-step values. The figure shows sensitivity oscillations considering a period of 14 seconds.

It is important to observe that the big difference between $\Delta t = 0.001$ sec and $\Delta t = 0.01$ sec results in negligible differences in the resulting trajectory sensitivities.

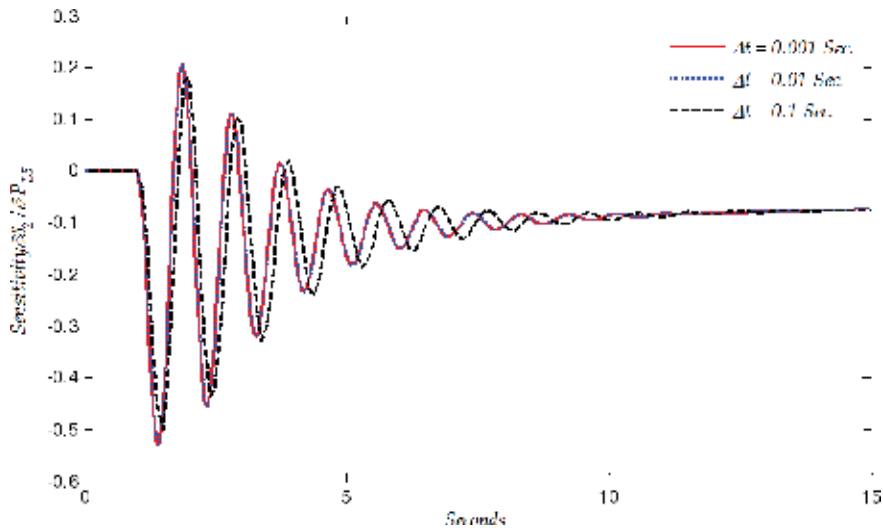


Figure 5.
 Effect of the integration time step on the evolution of parameter sensitivities, [30].

For the two cases, the TS calculation required to compute 14000 and 1400 forward/backward substitutions, respectively. Such a difference is equivalent to reduce in 90% the number of sensitivity solutions. For the case with $\Delta t = 0.1$ sec, 140 forward/backward substitutions were required, which represents a reduction of 99% of such solutions required to assess the transient. Although for this case, a small difference between trajectory sensitivities results, this is still negligible. This TS-based method can assess at the same time the effect of N_p parameters in the EP stability, whereas in the method of eigenvalues and modal analysis, it is not possible.

5.3 Most sensitive loads to Hopf bifurcation

The participation factors provide the change of critical eigenvalues to the change of the states of critical machines ($\partial\lambda/\partial x$), which establishes the SMA. However, this analysis does not provide information about the critical parameter (critical load in this case) influencing the EP stability but only the critical generator and its most participative states. Thus, the modal analysis does not allow the direct identification of the most sensitive loading directions in the stability of the EPs around a HB point. In practice, load increments not have a unique loading direction as in the previous study, which results in a valid consideration only for academic interest. All loads are then constantly varying in N_p directions, so that it is very important to have a general tool to assess the stability of the EPs, especially operating under stressed conditions of loading. In this context, besides identifying the critical generators (states), the SMA-TS approach based on TS identifies the loading directions which are most sensitive to oscillatory instabilities.

Multiparameter analysis of TS allows computing trajectory sensitivities with respect to N_p parameters in a power system [17] at the same time, as explained in Section 3.3, and can be used to find out the influence of the different loading directions on the SSS around a HB point. For this purpose, **Figure 6** shows the sensitivity norm SN through the time with respect to the three embedded loads in the system, where the highest peaks indicate the maximum influence of the corresponding load in the oscillatory behavior. The load demand corresponds to the base case as provided in [7].

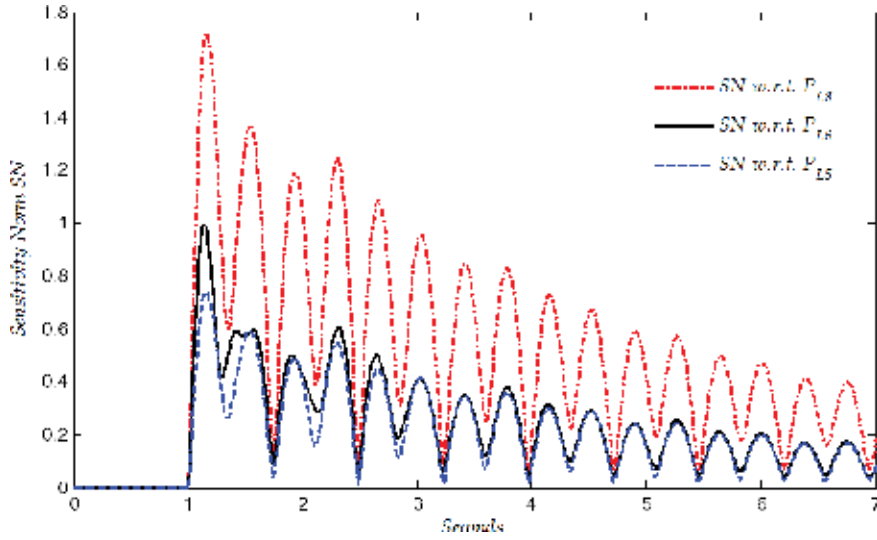


Figure 6. Loads' effect on the EP's stability (WSCC system), [30].

Node	P_{base} (MW)	ΔP_{HB} (MW)	P_{HB} (MW)	SN
8	100.0	299	399	1.723
6	90.0	314	404	0.997
5	125.0	316	441	0.739

Table 2. Sensitivity norm and Hopf bifurcation (WSCC system).

The oscillation of SN_ρ shows that the load embedded at bus 8 (P_{L8}) is the most sensitive for the EP. The load at bus 6 (P_{L6}) is the next most sensitive and finally the load P_{L5} . In order to validate the information provided by the SN_ρ in **Figure 6**, one parametric study at a time was carried out for the active powers P_{L8} and P_{L6} as performed in **Table 1** for the load P_{L5} . The results are reported in **Table 2** as follows: the first column indicates the load nodes, and columns 2 and 3 present the measured powers in the base case and the active power increment from the base case to the HB point to each loading direction, respectively. The fourth column provides the active power magnitude at which a HB point occurs, and lastly, column 5 presents the obtained values of SN_ρ . It is important to observe in **Table 2** that the smallest load increment matches the highest SN value and vice versa, i.e., the highest SN indicates a major change in the EP stability with respect to the corresponding load variation, which determines a shorter way to the HB point. Thus, the smallest increment $\Delta P_{L8} = 299$ MW proves that the highest SN value indicates this load takes the system to the HB faster than $\Delta P_{L6} = 314$ MW and this in turn faster than $\Delta P_{L5} = 316$ MW. This agrees with the SN_ρ reported in **Figure 6**.

6. Trajectory sensitivity analysis: the Mexican system

In this section, the study consisted of computing the TS norm for 91 loads embedded in a reduced equivalent of the Mexican energy system, which consists of 190 nodes and 46 generators. The transmission components are divided into 180 transmission lines and 83 power transformers. Lastly, the system contains 26

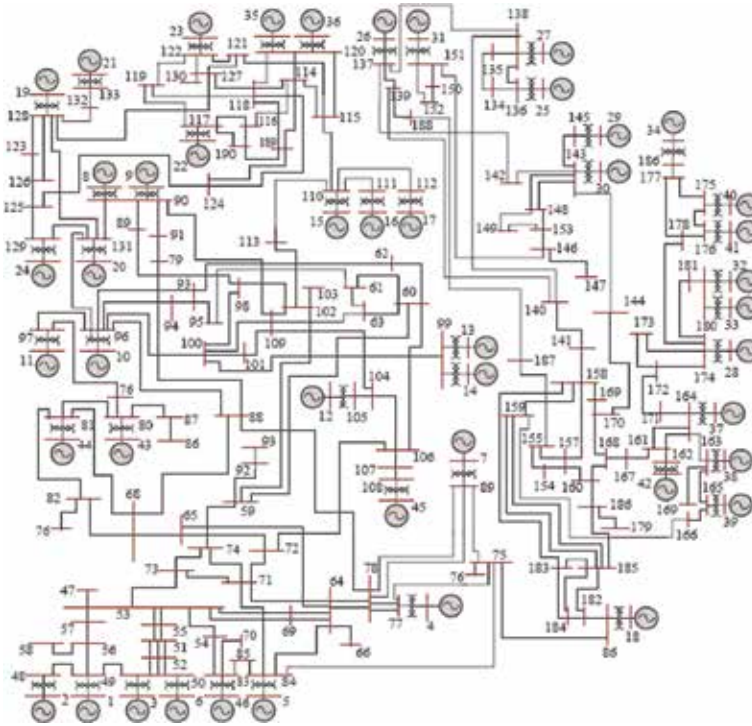


Figure 7.
 The Mexican power system.

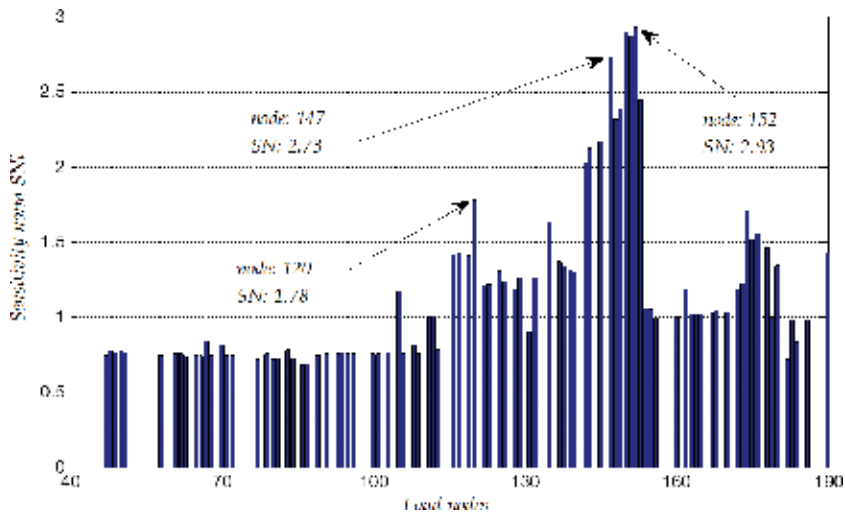


Figure 8.
 Loads' effect on the equilibrium point stability (Mexican system), [30].

capacitive compensators in shunt connection. The unifilar diagram of the power system is shown in **Figure 7**.

In order to assess the effect of the system loads on the system's dynamic performance, the sensitivity norms with respect to 91 loads were computed. **Figure 8** shows the effect of these sensitivities on a critically stable EP. Note that the active power demanded by loads connected at buses from 150 to 152 is the most sensitive in the EP stability. Therefore, according to the reasoning used into the previous

section, the loading increase in such directions will steer in a faster way the system to a HB than the rest of the system loads. It must be pointed out that the computation of the sensitivity norms for the 91 system loads were carried out by using one sole time-domain simulation, which corresponds to solving 91 sensitivity DAE systems, with each one consisting of 702 equations and variables. Thus, the assessment of the 91 loads is equivalent to solving 63882 equations in the same simulation at the same time. However, considering the linearity of the sensitivity systems, the same time-invariant Jacobian matrix is used during the whole time-domain simulation, which considerably reduces the computational burden.

Once the critical loads have been identified from **Figure 8**, it is possible to know the most affected generators by the most sensitive loads. **Figure 9** shows the TS with respect to the active power at bus 152, which resulted as the most sensitive in the sensitivity norm assessment. The damped oscillations in the TS indicate that the EP is stable and the operation point is not at a HB, which agrees with the corresponding critical eigenvalue of the EP $\lambda = -0.0501 \pm 7.8518i$. It must be observed from **Figure 9** that the highest rotor angle sensitivities $\partial\delta_{32}/\partial P_{L152}$ and $\partial\delta_{33}/\partial P_{L152}$ have identified generators 32 and 33 as the most influenced by the active power embedded at bus 152.

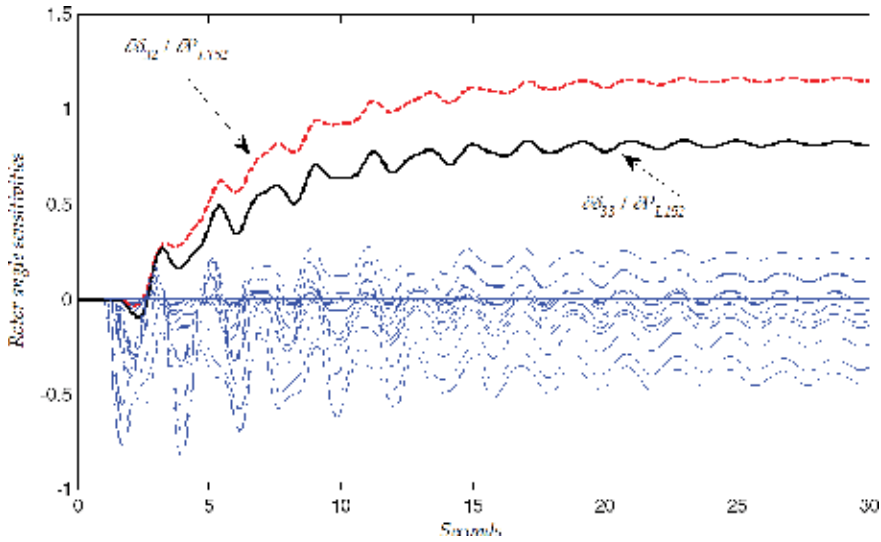


Figure 9. Evolution of parameter sensitivities with respect to P_{L152} , $\lambda_{crit} = -0.05 \pm 7.85i$, [30].

Node	λ_{crit}	P_{base} (MW)	ΔP_{60} (60 MW)	ΔP_{HB} (MW)	P_{HB} (MW)
152	$0.021 \pm 5.02i$	172.64	232.64	53.0	225.64
150	$0.018 \pm 5.03i$	188.24	248.64	54.0	242.24
151	$0.015 \pm 5.03i$	18.72	78.72	54.0	72.72
147	$0.012 \pm 5.05i$	104.00	164.00	56.0	160.00
153	$-0.011 \pm 8.83i$	78.00	138.00	63.0	141.00
145	$-0.015 \pm 5.13i$	83.20	143.20	72.0	155.20
120	$-0.050 \pm 7.85i$	308.88	368.88	189.0	497.88

Table 3. Loads' sensitivity norm to Hopf bifurcation in the Mexican system.

In order to validate the load ranking influence via the sensitivity norm, **Table 3** shows how the increments in the most sensitive loading directions influence the SSS, as well as the proximity to the HB point. Column 1 (Node) indicates the most sensitive loads resulted from the TS analysis shown in **Figure 8**. Column 2 (λ_{crit}) provides the critical eigenvalue for the new EP resulting from such an increment. Columns 3 and 4 show the measured value of active power in the analyzed base case (P_{base}) corresponding to **Figure 9** and the increment in the specified loading direction (ΔP (60 MW)), respectively. Lastly, in columns 5 and 6, (ΔP_{HB}) and (P_{HB}) indicate the increased amount and the value of the active power where the system crosses a HB point by following the corresponding loading directions.

It is important to outline that the load effect in the EP stability is not only dependent on the magnitude but also on the topologic location of loads. For example, the power demand embedded at bus 120 is 17 times larger than the load at bus 151; however, the load at 151 resulted in being more sensitive than the load embedded at bus 120, as shown in **Table 3**, column 3. It must be observed that the most sensitive loads (loads 152–147) provided a major change in the critical eigenvalue and thus in the SSS. The same increment in the most sensitive loading directions (buses 152–147) led the system to oscillatory instability due to a HB point, whereas with the increment in the least sensitive loading directions, the system remained stable. Then, the stability margins in the most sensitive loading directions become more reduced; therefore, according to the sensitivity ranking in **Table 3**, as the most sensitive loads were increased, the appearance of the HB was found faster as can be observed in column 5. Once more the SMA-TS approach has been successfully proved by determining that the most sensitive loads indicate the shorter ways toward the small-signal instability of the electric power systems.

7. Conclusions

In this chapter an alternative approach for monitoring the Hopf bifurcations along variations in multidimensional loading directions by using a time-domain method is presented, which is based on trajectory sensitivities. This approach, SMA-TS, is general and flexible, i.e., the size of the power systems, as well as the complexity of their mathematical modeling, does not represent any restriction. SMA-TS allows to identify the critical loading directions that steer the system to Hopf bifurcation points. Such an approach was tested in the 9-buses, 3-generators system as well as in 190-buses, 46-generators system. Regardless of the number of sensitivity parameters and system dimensions, SMA-TS requires only one simulation. Such a method keeps constant the Jacobian matrix of the system, requiring only one evaluation and factorization during the whole simulation. The computational effort then consists of performing just one forward/backward substitution at each time step. Furthermore, the approach can handle a very large integration step to drastically reduce the computational effort. Lastly, its application is suitable for real-time monitoring and security assessment in energy management systems.

Acknowledgements

The authors thank the University of Guanajuato for providing the financial support with PFCE 2018 resource for this publication.

Conflict of interest

All the authors of this chapter declare to have no any conflict of interest related with any person, company, institution, etc.

Author details

Enrique Arnaldo Zamora Cárdenas^{1*}, Alejandro Pizano Martínez¹ and Claudio Rubén Fuerte Esquivel²

1 Universidad de Guanajuato, Salamanca, Mexico

2 Universidad Michoacana de San Nicolás de Hidalgo, Morelia, Mexico

*Address all correspondence to: ezamora@ugto.mx

IntechOpen

© 2018 The Author(s). Licensee IntechOpen. This chapter is distributed under the terms of the Creative Commons Attribution License (<http://creativecommons.org/licenses/by/3.0>), which permits unrestricted use, distribution, and reproduction in any medium, provided the original work is properly cited. 

References

- [1] IEEE/CIGRE Joint Task Force on Stability Terms and Definitions. Definition and classification of power system stability. *IEEE Transactions on Power Systems*. 2004;**19**:1387-1401. DOI: 10.1109/TPWRS.2004.825981
- [2] Chen C. *Linear System Theory and Design*. 3rd ed. New York, NY: Oxford University Press Inc.; 1998. 352 p
- [3] Lyapunov A. Stability of motion. In: *Mathematics in Science and Engineering*. Vol. 30. New York/London: Academic Press Inc.; 1968
- [4] Pérez-Arriaga I, Verghese G, Schweppe F. Selective modal analysis with applications to electric power systems. Part I: Heuristic introduction. *IEEE Transactions on Power Apparatus and Systems*. 1982;**101**:3117-3125. DOI: 10.1109/TPAS.1982.317524
- [5] Verghese G, Pérez-Arriaga I, Schweppe F. Selective modal analysis with applications to electric power systems, Part II: The dynamic stability problem. *IEEE Transactions on Power Apparatus and Systems*. 1982;**101**:3126-3134. DOI: 10.1109/TPAS.1982.317525
- [6] Kundur P. *Power System Stability and Control*. California: McGraw Hill Inc.; 1994. 1178 p
- [7] Sauer P, Pai M. *Power System Dynamics and Stability*. Upper, Saddle, River, NJ: Prentice Hall; 1998
- [8] Nayfeh A, Balachandran B. *Applied Nonlinear Dynamics*. New York, NY: John Wiley & Sons; 1995. 700 p
- [9] Ajarapu V. *Computational Techniques for Voltage Stability assessment and Control*. New York, NY: Springer; 2006. 250 p
- [10] Ajarapu V, Lee B. Bifurcation theory and its application to nonlinear dynamical phenomena in an electrical power system. *IEEE Transactions on Power Systems*. 1992;**7**:424-431. DOI: 10.1109/59.141738
- [11] Gu W, Milano F, Jiang P, Tang G. Hopf bifurcations induced by SVC controllers: A didactic example. *Electric Power Systems Research*. 2007;**77**:234-240. DOI: 10.1016/j.epsr.2006.03.001
- [12] Kwatny H, Fischl R, Nwankpa C. Local bifurcation in power systems: Theory, computation and applications. *Proceedings of the IEEE*. 1995;**83**:1456-1483
- [13] Xiaoyu W. A novel approach for identification and tracing of oscillatory stability and damping ratio margin boundaries [thesis]. Ames: Iowa State University; 2005
- [14] Joorabian M, Ramandi N, Ebadi M. Optimal location of static VAR compensator (SVC) based on small signal stability of power system. In: *Proceedings of the 2nd IEEE International Conference on Power and Energy (PECon 08)*; 1-3 December 2008; Johor Baharu, Malaysia. 2008. pp. 1333-1338
- [15] Gupta A, Sharma P. Optimal location of SVC for dynamic stability enhancement based on eigenvalue analysis. *Electrical and Electronics Engineering: An International Journal (ELELIJ)*. 2014;**3**:25-37
- [16] Sharma C, Singh P. Contribution of loads to low frequency in power system operation. In: *Proceedings of the iREP Symposium-Bulk Power System Dynamics and Control-VII*; 19-24 August 2007; Charleston, SC, USA. 2007

- [17] Frank P. Introduction to System Sensitivity Theory. 1st ed. New York: Academic Press; 1978. p. 286
- [18] Tomovic R, Vucobratovic M. General Sensitivity Theory. New York: North-Holland; 1972. p. 266
- [19] Laufenberg M, Pai M. A new approach to dynamic security assessment using trajectory sensitivities. *IEEE Transactions on Power Systems*. 1998;**13**:953-958. DOI: 10.1109/59.709082
- [20] Nguyen T, Pai M. Trajectory sensitivity analysis for dynamic security assessment and other applications in power systems. In: Savulescu S, editor. *Real-Time Stability in Power Systems*. 2nd ed. Switzerland: Springer; 2014. DOI: 10.1007/978-3-319-06680-6_11
- [21] Hiskens I, Pai M. Trajectory sensitivity analysis of hybrid systems. *IEEE Transactions on Circuits and Systems I: Fundamental Theory and Applications*. 2000;**47**:204-220. DOI: 10.1109/81.828574
- [22] Hong Z, Shrirang A, Emil C, Mihai A. Discrete adjoint sensitivity analysis of hybrid dynamical systems with switching [Discrete adjoint sensitivity analysis of hybrid dynamical systems]. *IEEE Transactions on Circuits and Systems I: Regular Papers*. 2017. DOI: 10.1109/TCSI.2017.2651683
- [23] Nguyen T, Pai M, Hiskens I. Sensitivity approaches for direct computation of critical parameters in a power system. *International Journal of Electrical Power and Energy Systems*. 2002;**24**:337-343. DOI: 10.1016/S0142-0615(01)00050-3
- [24] Chatterjee D, Ghosh A. Transient stability assessment of power system containing series and shunt compensators. *IEEE Transactions on Power Systems*. 2007;**22**:1210-1220. DOI: 10.1109/TPWRS.2007.901455
- [25] Suguna R, Jalaja S, Pradeep M, Senthil R, SrikrishnaKumar S, Sugavanam K. Transient stability improvement using shunt and series compensators. *Indian Journal of Science and Technology*. 2016;**9**:1-11. DOI: 10.17485/ijst/2016/v9i11/89402
- [26] Zamora-Cárdenas A, Fuerte-Esquivel C. Multi-parameter trajectory sensitivity approach for location of series-connected controllers to enhance power system transient stability. *Electric Power Systems Research*. 2010; **80**:1096-1103. DOI: 10.1016/j.epr.2010.02.002
- [27] Chatterjee D, Ghosh A. TCSC control design for transient stability improvement of a multi-machine power system using trajectory sensitivity. *Electric Power Systems Research*. 2007; **77**:470-483. DOI: 10.1016/j.epr.2010.02.002
- [28] Alexander J. Oscillatory solutions of a model system of nonlinear swing equations. *International Journal of Electrical Power and Energy Systems*. 1986;**8**:130-136. DOI: 10.1016/0142-0615(86)90027-X
- [29] Guo T, Schlueter R. Identification of generic bifurcation and stability problems in power system differential-algebraic model. *IEEE Transactions on Power Systems*. 1994;**9**:1032-1044. DOI: 10.1109/59.317640
- [30] Zamora-Cárdenas E, Fuerte-Esquivel C. Computation of multi-parameter sensitivities of equilibrium points in electric power systems. *Electric Power Systems Research*. 2013; **96**:246-254. DOI: 10.1016/j.epr.2012.11.013

Power System Small-Signal Stability as Affected by Grid-Connected SmartPark

Cai Hui

Abstract

Large-scale smart charging stations can effectively satisfy and control the charging demands of tremendous plug-in electric vehicles (PEVs). But, simultaneously, their penetrations inevitably induce new challenges to the operation of power systems. In this chapter, damping torque analysis (DTA) was employed to examine the effects of the integration of smart charging station on the dynamic stability of the transmission system. A single-machine infinite-bus power system with a smart charging station that denoted the equivalent of several ones was used for analysis. The results obtained from DTA reveal that in view of the damping ratio, the optimal charging capacity is better to be considered in the design of the smart charging station. Under the proposed charging capacity, the power system can achieve the best maintained dynamic stability, and the damping ratio can reach the crest value. Phase compensation method was utilized to design the stabilizer via the active and reactive power regulators of the smart charging station respectively. With the help of the stabilizers, damping of the system oscillation under certain operating conditions can be significantly improved, and the power oscillation in the tie-line can be suppressed more quickly.

Keywords: smart charging station, plug-in electric vehicles (PEVs), power system oscillations, small-signal stability, damping torque analysis (DTA), stabilizer design

1. Introduction

The growing concern of carbon dioxide emission, greenhouse effect, and rapid depletion of fossil energy drives the demand for the revolutionary changes in the automobile industry. Much effort has been put into developing a new high-efficient, environment-friendly, and safe transportation vehicle that can replace the conventional ones. The utilization of plug-in electric vehicles (PEVs) as the most suitable solution has been promoted in many countries. China is expected to have 5 million electric vehicles (EVs) by 2020 according to its Development Plan for Energy-saving and Renewable Energy Vehicles. However, a prediction by State Grid Corporation of China (SGCC) illustrates that the number will be 5–10 million due to the fast development of EVs at present in China. As EV-related technologies have been making progress and many national and local incentives have been created for EV purchases, the total number of EVs is likely to be 30 million by 2030 [1–3].

With the significant increase of PEVs, the corresponding parking lots termed as smart charging stations in [4–8] will be established to charge the tremendous PEVs. A typical city will contain several SmartParks, as the aggregator of numerous EV charging stations, distributed throughout the city one to few miles apart in the distribution system. The newly established smart charging stations are preferred to be connected to an additional bus of the transmission system [3–5]. The vehicle-to-grid (V2G) technology supplies the bidirectional communication between the parked vehicles and connected grid. The vehicles parked in the smart charging station can not only simply absorb active power (AP) from the grid for charging, but also participate in power regulation during discharging mode. Ref. [7] shows that most personal vehicles in the U.S. were parked more than 95% of the day and generally followed a daily schedule. The huge number of parked PEVs has the assignable potential to impact the frequency stability, voltage stability, and rotor-angle stability of the system [9–16]. Nowadays, the capacity of smart charging stations is much lower than that of the conventional power plants. Only frequency stability and voltage stability of the distribution systems attract much attention in recent years. However, if only half of the 230 million gasoline-powered cars, sport utility vehicles, and light trucks in U.S. are converted to or replaced with the electric vehicles, they would have 20 times the power capacity of all electricity in the country [17]. The impacts of SmartParks on the stability of the transmission systems cannot be ignored any more. Power system oscillations, as one section of the dynamic stability, occur inherently due to the rotor inertia of synchronous generators such that it takes time for them to respond to the sudden lack or excess of active power in a power system. The increased amplitude or weakly damped power oscillations via the tie-lines will lead to wrong activation of the automatic protection devices, splitting of the system, or even collapse. While the time-varying nature of the load-flow condition in the power system with high-penetrated smart charging stations is the common reason for the appearance of power oscillations, damping torque of the system is extremely interesting.

Under different operating conditions, smart charging stations can vary from the adjustable load in the charging mode to the regulable generator in the discharging mode and vice versa with the voltage control strategy [4–6]. It is significantly valuable to examine how and why it may interact with the conventional power generation, hence affecting power system small-signal stability. In order to gain a good understanding on and clear insight into this interaction through theoretical analysis, a single-machine infinite-bus power system is adopted in this chapter. A smart charging station is connected to the system and theoretical damping torque analysis is carried out to check how and why the smart charging station interacts with the single generator so as to affect the power oscillation. It is expected that the analytical conclusions obtained in the chapter can be used to guide further work on a more complicated case of the oscillations in multi-machine power systems.

The organization of this chapter is as follows: in Section 2, a comprehensive model of a single-machine infinite-bus power system integrated with a smart charging station is established. After that, damping torque analysis (DTA) [18–21] is employed to examine the effect of joint operation of a smart charging station and a conventional synchronous machine on the system's small-signal stability in Section 3. The result of the damping torque analysis indicates that the smart charging station does not contribute an extra mode of electromechanical oscillation. It affects power system small-signal stability by supplying either positive or negative damping torque to the conventional power plant varying with the system operating conditions. Analysis also reveals that from the view of damping ratio,

the optimal charging capacity is better to be considered during the design of the smart charging station. In Section 4, the phase compensation method is utilized to design the stabilizer via the active power and reactive power (RP) regulators of the smart charging station, respectively. A single-machine infinite-bus power system integrated with a smart charging station is presented as an example in Section 5. Results of numerical computation, non-linear simulations, and eigenvalue calculations at different system operating conditions are given. These simulations and results demonstrate and confirm the presented theoretical analysis, and verify the effectiveness of the designed stabilizer. Another four-machine power system is employed to show that the conclusions obtained in the single-machine power system are also available in the multi-machine power system. Conclusions are summarized in Section 6.

2. A linearized model of single-machine infinite-bus system with a smart charging station

The local electricity generation systems, besides supporting the regional loads, can be used to charge a smart charging station under usual conditions. Comparing with 1000-million-kilowatt capacity of outer power systems, the abundant active power generation with 10,000-kilowatt capacity in a regional system can be simplified as an equivalent synchronous machine. The inertia of the equivalent synchronous machine denotes the dynamic stability of the regional system. Because every individual smart charging station has the same dynamic behavior during the transient procedure, the smart charging stations can be regarded as an equivalent one with higher active power and reactive power capacities. A smart charging station usually is connected to the transmission system through a step-up transformer, which is seen as a reactance in this chapter.

In this chapter, the research focuses on the power oscillation which lasts for mostly 10–20 s. Uncertainties during EV charging such as the alternations of charging strategies or vehicle numbers have little effect on this analysis. EV charging demand or discharging supply during this dynamic procedure is considered as determinate power from the start time and following seconds. For a simple analysis, a constant power charging/discharging strategy is utilized to estimate the optimal EV charging numbers for smart charging station design.

Figure 1 shows the configuration of a single-machine infinite-bus power system, where a smart charging station is connected at a busbar denoted by subscript s . The linearized models of network equations and synchronous machine are presented in [18, 22, 23].

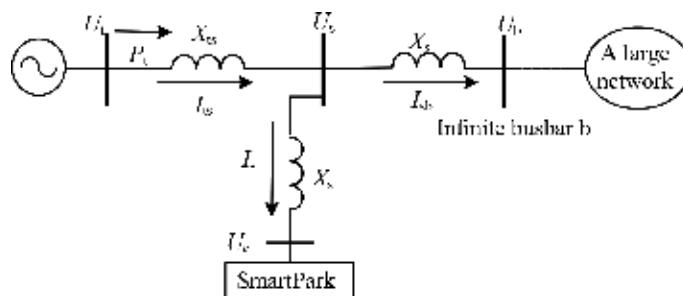


Figure 1.
 Simplified model of the power system in a city.

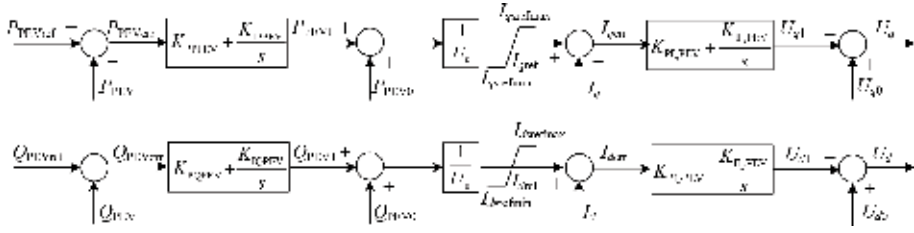


Figure 2.
Control strategy of a smart charging station.

Here, U_s is the voltage at the high-voltage-level busbar where the smart charging station locates; U_b and U_c are the voltages at infinite busbar and the low-voltage-level busbar connected with the smart charging station; I_{ts} , I_s , and I_{sb} are the line currents as indicated in **Figure 1**; and X_{ts} , X_{sb} , and X_s are line reactances as indicated in **Figure 1**.

The control strategy of smart charging stations is shown in **Figure 2**.

The objective control is to command the currents corresponding to the fast change in demanded active and reactive power. The equations of smart charging stations according to **Figure 2** are obtained as:

$$\left\{ \begin{array}{l} P_1 = (K_{PP} + K_{IP}/s)(P_{PEVref} - P_{PEV}) \\ I_{qsref} = \frac{P_1 + P_{10}}{U_s} \\ U_{qc1} = (K_{PIq} + K_{IIq}/s)(I_{qsref} - I_{qs}) \\ U_{qc} = U_{qc0} + U_{qc1} \\ Q_1 = (K_{PQ} + K_{IQ}/s)(Q_{PEVref} - Q_{PEV}) \\ I_{dsref} = \frac{Q_1 + Q_{10}}{U_s} \\ U_{dc1} = (K_{PID} + K_{IID}/s)(I_{dsref} - I_{ds}) \\ U_{dc} = U_{dc0} + U_{dc1} \end{array} \right. \quad (1)$$

where

P_{PEV} and Q_{PEV} are the demanded active and reactive power by the smart charging station and

$K_{PP} + \frac{K_{IP}}{s}$, $K_{PQ} + \frac{K_{IQ}}{s}$, $K_{PI_d} + \frac{K_{II_d}}{s}$, $K_{PI_q} + \frac{K_{II_q}}{s}$ are the proportional-integral controllers in the smart charging station.

Linearized from Eq. (1),

$$\left\{ \begin{array}{l} \Delta U_{dc} = K_{U_{dc}U_{dc}} \Delta U_{dc} + K_{U_{dc}U_{qc}} \Delta U_{qc} + K_{U_{dc}E'_q} \Delta E'_q + K_{U_{dc}\delta} \Delta \delta \\ \Delta U_{qc} = K_{U_{qc}U_{dc}} \Delta U_{dc} + K_{U_{qc}U_{qc}} \Delta U_{qc} + K_{U_{qc}E'_q} \Delta E'_q + K_{U_{qc}\delta} \Delta \delta \end{array} \right. \quad (2)$$

where

$$\left\{ \begin{array}{l} \Delta P_{PEV} = K_{PPU_{dc}} \Delta U_{dc} + K_{PPU_{qc}} \Delta U_{qc} + K_{PPE'_q} \Delta E'_q + K_{PP\delta} \Delta \delta \\ \Delta Q_{PEV} = K_{QPU_{dc}} \Delta U_{dc} + K_{QPU_{qc}} \Delta U_{qc} + K_{QPE'_q} \Delta E'_q + K_{QP\delta} \Delta \delta \\ \Delta U_s = K_{U_sU_{dc}} \Delta U_{dc} + K_{U_sU_{qc}} \Delta U_{qc} + K_{U_sE'_q} \Delta E'_q + K_{U_s\delta} \Delta \delta \end{array} \right. \quad (3)$$

Arranging from Eq. (2),

$$\begin{cases} \Delta U_{dc} = K_{sp-U_{dc}E'_q} \Delta E'_q + K_{sp-U_{dc}\delta} \Delta \delta \\ \Delta U_{qc} = K_{sp-U_{qc}E'_q} \Delta E'_q + K_{sp-U_{qc}\delta} \Delta \delta \end{cases} \quad (4)$$

While this chapter focuses on the analysis of the impact from the grid-connected smart charging station to the system small-signal stability, linearized processes and expressions for coefficients are not specifically listed.

3. Analysis of damping torque contribution from the Phillips-Heffron model

The Phillips-Heffron model of a smart charging station, which is based on the linearization of the system and describes the relationships between all variables, assessed to the single-machine infinite-busbar (SMIB) power system can be obtained as **Figure 3**, where the Phillips-Heffron model of SMIB only is referred to Refs. [22–24]. From Eqs. (2) and (3), the model of the smart charging station and its control strategy can be obtained as **Figure 4**.

From **Figures 3** and **4**, we have:

$$\begin{aligned} \Delta T_{et-sp} &= \Delta T_{st-sp} + j\Delta T_{dt-sp} = K_{PU_{dc}} \Delta U_{dc} + K_{PU_{qc}} \Delta U_{qc} \\ &= \left(K_{PU_{dc}} K_{sp-U_{dc}\delta} + K_{PU_{qc}} K_{sp-U_{qc}\delta} \right) \Delta \delta \end{aligned} \quad (5)$$

$$\begin{aligned} \Delta T_{et-ex} &= \Delta T_{st-ex} + j\Delta T_{dt-ex} = K_{PE'_q} \\ &\quad - \left[K_{E_q U_{qc}} K_{sp-U_{qc}\delta} + K_{E_q \delta} - \frac{K_a}{1+sT_a} \left(K_{U_t U_{dc}} K_{sp-U_{dc}\delta} + K_{U_t U_{qc}} K_{sp-U_{qc}\delta} + K_{U_t \delta} \right) \right] \\ &\quad \frac{\Delta \delta}{\left(T'_{d0}s + K_{E_q E'_q} \right) + K_{E_q U_{qc}} K_{sp-U_{qc}E'_q} - \frac{K_a}{1+sT_a} \left(K_{U_t U_{dc}} K_{sp-U_{dc}E'_q} + K_{U_t U_{qc}} K_{sp-U_{qc}E'_q} + K_{U_t E'_q} \right)} \end{aligned} \quad (6)$$

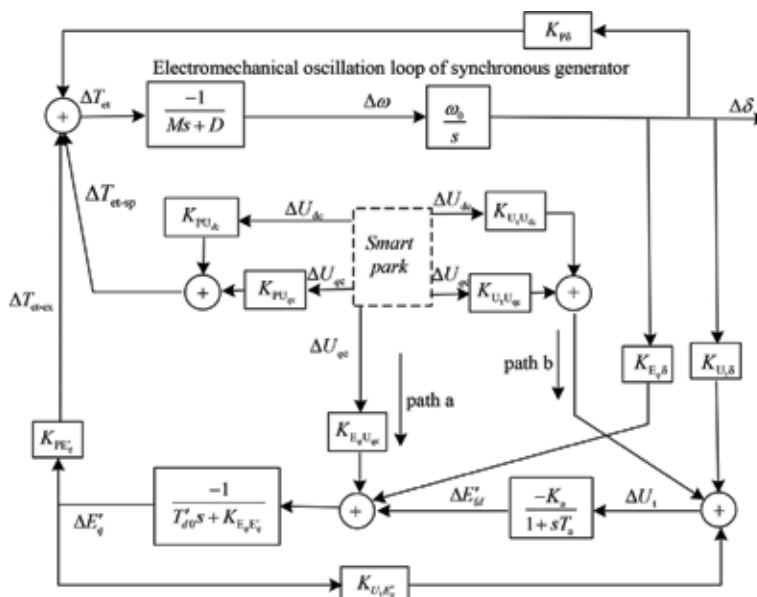


Figure 3. Phillips-Heffron model of the single-machine infinite-busbar system with a smart charging station.

$$\Delta T_{et} = \Delta T_{st} + j\Delta T_{dt} = \Delta T_{et-sp} + \Delta T_{et-ex} = (\Delta T_{st-sp} + \Delta T_{st-ex}) + j(\Delta T_{dt-sp} + \Delta T_{dt-ex}) \quad (7)$$

Figures 3 and 4 clearly show the dynamic interaction between the smart charging station and the conventional synchronous generator. Figure 3 is very similar to the conventional Phillips–Heffron model based on which the DTA was proposed and developed. It shows that the smart charging station interacts closely with the generator by contributing the electric torque to the electromechanical oscillation loop of the generator. The contribution of electric torque is comprised of two parts, viz. ΔT_{et-sp} which relates to $\Delta\delta$ and directly affects the oscillation loop, and ΔT_{et-ex} which relates to $\Delta E'_q$ and functions through the excitation system, as indicated in Figure 3. According to DTA, the electric torque can be decomposed into two components, viz. the synchronizing torque and the damping torque as shown in Eq. (7). The damping torque contributions ΔT_{dt-sp} , ΔT_{dt-ex} , and ΔT_{dt} determine the influences on the damping of power system oscillation.

With certain output power of the synchronous machine and absorbed or injected power of the smart charging station, the bus voltages and currents of the corresponding operation condition can be determined. The damping torques ΔT_{dt-sp} ,

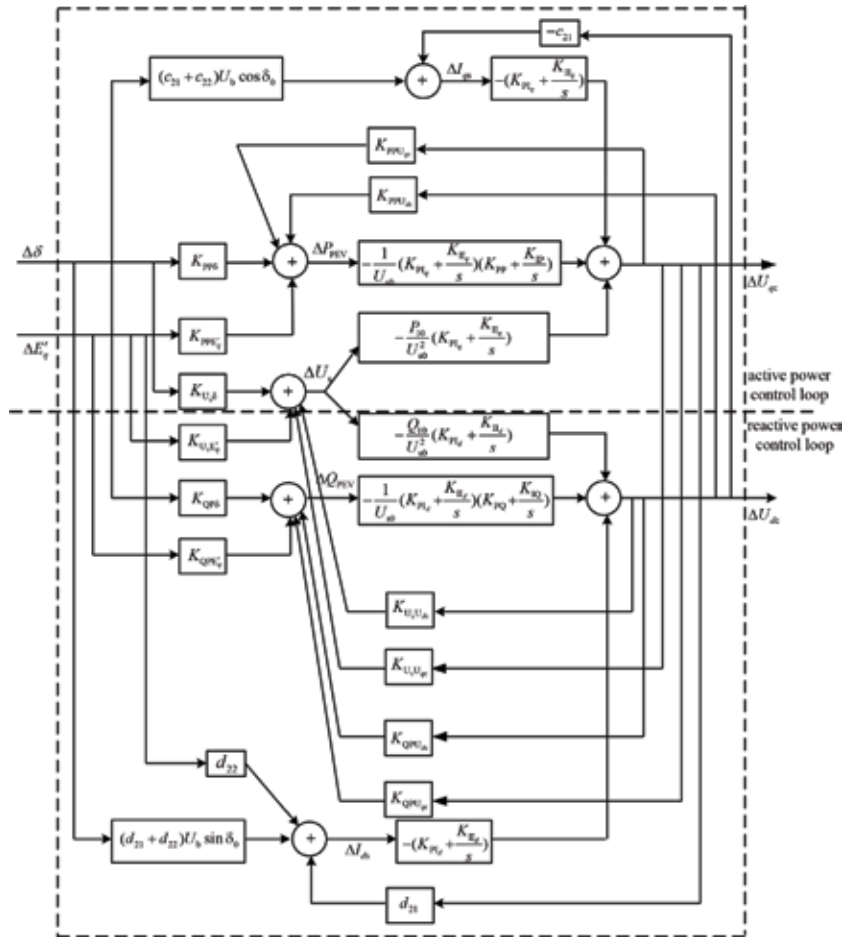


Figure 4. Linearized model of a smart charging station and its control.

ΔT_{dt-ex} , and ΔT_{dt} are dependent on the output power of the synchronous machine and the absorbed or injected power of the smart charging station.

From Eqs. (5)–(7), the conclusions can be summarized as follows:

1. The proportional controls K_p in the smart charging station mainly induce the synchronous torque into the oscillation loop, while for ΔT_{et-sp} in Eq. (5), only its real part is related to $\Delta\delta$; and the majority of damping torque is introduced by integral controls K_i/s , because $1/s$ induces the imaginary part in ΔT_{et-sp} relating to $\Delta\omega$.
2. Because the signals ΔU_{dc} and ΔU_{qc} through path a and path b in **Figure 3** are significantly attenuated by lag loops before they form one part of the damping torque through the excitation system [24], the damping torque contribution from them can be neglected for simplified analysis. ΔT_{dt-sp} represents the main damping torque supplied by the smart charging station in damping torque analysis, and ΔT_{dt-ex} mainly expresses the torque supplied by the excitation system of the synchronous machine.
3. In this chapter, the ‘-’ sign indicates the vehicles are selling power to the grid, that is, they are in discharging mode and the ‘+’ sign indicates that they are buying power from the grid, denoting that the vehicles are in charging mode.

The optimal operation point when the system has the biggest damping torque can be calculated as:

$$\frac{\partial \Delta T_{dt}}{\partial P_{PEV}} = \frac{\partial \Delta T_{dt-sp} + \partial \Delta T_{dt-ex}}{\partial P_{PEV}} = 0 \& \frac{\partial^2 \Delta T_{dt}}{\partial P_{PEV}^2} \leq 0 \text{ when } P_{PEV} > 0 \quad (8)$$

When the output power of the synchronous machine is fixed, the positive or negative damping torque supplied by the excitation system of the synchronous machine is only slightly changed. At the optimal operation point, the total damping torque ΔT_{dt} of the system and ΔT_{dt-sp} contributed from the smart charging station both reach their maximum values.

When the active power in the tie-line is fixed, the output power of the synchronous machine is changed corresponding to the absorbed or injected power of the smart charging station. Both damping torques contributed by the smart charging station and the excitation system need to be considered. The total damping torque ΔT_{dt} of the system and ΔT_{dt-sp} contributed from the smart charging station reach their maximum values at different operation points.

4. Design for the stabilizer attached to the smart charging station

Under the operation conditions that the total damping torques supplied by the smart charging station and the excitation system are not enough to suppress the oscillations, additional damping torques need to be added. Compared with the installation and coordinated parameter setting for power system stabilizers (PSSs) in synchronous machines, smart charging stations can be simply utilized to suppress the grid’s active power oscillation with little infrastructure cost. Only a centralized stabilizer will be required at the smart charging station to maintain system stability.

The stabilizer added via the active power (AP) or reactive power (RP) control loop is shown in **Figure 5**.

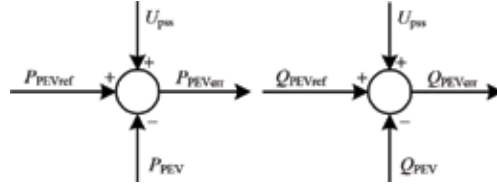


Figure 5. Control strategy of the stabilizer added via AP and RP control loop, respectively.

The forward path function which describes the way from output signal of the stabilizer to the additional damping torque into the electromechanical oscillation loop can be obtained:

$$\left. \begin{aligned}
 F_{\text{pssp}}(s) &= \frac{\partial \Delta T_{\text{pss}}}{\partial \Delta u_{\text{pssp}}} = K_{\text{PU}_{dc}} K_{\text{sp-U}_{dc} u_{\text{pssp}}} + K_{\text{PU}_{qc}} K_{\text{sp-U}_{qc} u_{\text{pssp}}} + \\
 &\quad - \left[K_{\text{E}_q \text{U}_{qc}} K_{\text{sp-U}_{qc} u_{\text{pssp}}} - \frac{K_a}{1 + sT_a} \left(K_{\text{U}_t \text{U}_{dc}} K_{\text{sp-U}_{dc} u_{\text{pssp}}} + K_{\text{U}_t \text{U}_{qc}} K_{\text{sp-U}_{qc} u_{\text{pssp}}} \right) \right] \\
 &\quad \frac{K_{\text{PE}'_q}}{\left(T'_{d0}s + K_{\text{E}_q \text{E}'_q} \right) + K_{\text{E}_q \text{U}_{qc}} K_{\text{sp-U}_{qc} \text{E}'_q} - \frac{K_a}{1 + sT_a} \left(K_{\text{U}_t \text{U}_{dc}} K_{\text{sp-U}_{dc} \text{E}'_q} + K_{\text{U}_t \text{U}_{qc}} K_{\text{sp-U}_{qc} \text{E}'_q} + K_{\text{U}_t \text{E}'_q} \right)} \\
 F_{\text{pssq}}(s) &= \frac{\partial \Delta T_{\text{pss}}}{\partial \Delta u_{\text{pssq}}} = K_{\text{PU}_{dc}} K_{\text{sp-U}_{dc} u_{\text{pssq}}} + K_{\text{PU}_{qc}} K_{\text{sp-U}_{qc} u_{\text{pssq}}} + K_{\text{PE}'_q} \\
 &\quad - \left[K_{\text{E}_q \text{U}_{qc}} K_{\text{sp-U}_{qc} u_{\text{pssq}}} - \frac{K_a}{1 + sT_a} \left(K_{\text{U}_t \text{U}_{dc}} K_{\text{sp-U}_{dc} u_{\text{pssq}}} + K_{\text{U}_t \text{U}_{qc}} K_{\text{sp-U}_{qc} u_{\text{pssq}}} \right) \right] \\
 &\quad \frac{\left(T'_{d0}s + K_{\text{E}_q \text{E}'_q} \right) + K_{\text{E}_q \text{U}_{qc}} K_{\text{sp-U}_{qc} \text{E}'_q} - \frac{K_a}{1 + sT_a} \left(K_{\text{U}_t \text{U}_{dc}} K_{\text{sp-U}_{dc} \text{E}'_q} + K_{\text{U}_t \text{U}_{qc}} K_{\text{sp-U}_{qc} \text{E}'_q} + K_{\text{U}_t \text{E}'_q} \right)}
 \end{aligned} \right\} \quad (9)$$

where,

F_{pssp} or F_{pssq} is corresponding to the utilized output signal of the stabilizer u_{pssp} or u_{pssq} .

$K_{\text{sp-U}_{dc} u_{\text{pssp}}}$, $K_{\text{sp-U}_{qc} u_{\text{pssp}}}$, $K_{\text{sp-U}_{dc} u_{\text{pssq}}}$ and $K_{\text{sp-U}_{qc} u_{\text{pssq}}}$ are obtained from the linearization of the control strategy with the output signals of the stabilizer considered.

The active power P_b in the tie-line is chosen for the feedback signals of the stabilizers via the active power regulator and the reactive power regulator.

From the linear system control theory, the active power P_b can be written as a function of the rotor speed of the generator.

$$\Delta P_b = r_p(s) \Delta \omega \quad (10)$$

where $r_p(s) = \left(K_{\text{P}_b \delta} + K_{\text{P}_b \text{E}'_q} K_{\text{E}'_q \delta} \right) \frac{\omega_0}{s}$ is the reconstruction function for P_b .

While $\Delta P_b = \Delta P_t - \Delta P_{\text{PEV}}$, $K_{\text{P}_b \delta}$, $K_{\text{P}_b \text{E}'_q}$ and $K_{\text{E}'_q \delta}$ are related to the reconstruction of this feedback signal.

Considering Eqs. (9) and (10), the electric torques contributed by the stabilizer via active and reactive power regulators, respectively, are expressed as:

$$\begin{cases}
 \Delta \mathbf{T}(\Delta u_{\text{pssp}}) = F_{\text{pssp}}(s) r_p(s) G_{\text{PEVP}}(s) \Delta \omega \\
 \Delta \mathbf{T}(\Delta u_{\text{pssq}}) = F_{\text{pssq}}(s) r_p(s) G_{\text{PEVQ}}(s) \Delta \omega
 \end{cases} \quad (11)$$

where $G_{\text{PEVP}}(s)$ and $G_{\text{PEVQ}}(s)$ are the transfer function of the stabilizer via active and reactive power regulators respectively.

The transfer function of the stabilizer is

$$G_{PEV} = K_w \frac{1 + sT_2}{1 + sT_1} \frac{1 + sT_4}{1 + sT_3} \quad (12)$$

The stabilizers are designed to compensate the lagging or leading angle of the forward path, in order to supply maximum positive damping into the system. The phase compensation method is used to design the parameters of the stabilizers.

5. Case study

5.1 Case description

Two example cases are employed in this section. From Case A to Case D, a single-machine infinite-busbar power system is used. The parameters of the system are given in Appendix A.1. Under different capacities of the smart charging station, computational results of the damping torque contribution from the smart charging station and the excitation system to the electromechanical oscillation loop of the single synchronous generator are obtained and confirmed by the eigenvalue of the system's oscillation mode. The critical point in which the system has the biggest damping torque is highlighted. In Case E, a four-machine power system is presented. The parameters are given in Appendix A.2. The eigenvalue related to the inter-area oscillation mode is concerned under different capacities of the smart charging station.

5.2 Case A: utilizing only proportional control in the smart charging station and fixing load-flow in the tie-line

With the load-flow in the tie-line fixed at 10 MW, the comparison is done when only proportional control is utilized in the smart charging station under its different charging or discharging power capacities. The computational results of the example system are shown in **Table 1**, when only P control is utilized in the smart charging station. From **Table 1**, it can be concluded that:

$P_t/(10 \text{ MW})$	$P_{PEV}/(10 \text{ MW})$	$\Delta T_{dt}/pu$	$\Delta T_{dt-sp}/pu$	$\Delta T_{dt-ex}/pu$	Frequency/Hz	Damping ratio/%
4.0	3.0	0.6340	0.0006	0.6334	1.83	3.19
3.5	2.5	0.7842	0.0004	0.7838	1.82	3.47
3.0	2.0	0.4368	0.0002	0.4366	1.74	2.99
2.5	1.5	-0.1877	-0.0003	-0.1874	1.68	1.92
2.0	1.0	-0.5730	-0.0005	-0.5725	1.61	1.24
1.5	0.5	-0.1870	-0.0002	-0.1868	1.68	1.92
1.0	0.0	0.4345	0.0003	0.4342	1.74	2.99
0.5	-0.5	0.7851	0.0005	0.7846	1.82	3.47
0.0	-1.0	0.6348	0.0007	0.6341	1.83	3.19

Table 1. Computational results of the example system when only P control is utilized in the smart charging station.

1. The total damping torque contribution ΔT_{dt} is approximately equal to the damping torque from the excitation system ΔT_{dt-ex} . The change of ΔT_{dt} is mainly induced by ΔT_{dt-ex} which is the impact from the excitation system of the synchronous machine under different output power. The smart charging station only with the proportional control functions as an adjustable load in charging mode or as a regulator generator in discharging mode.
2. Integral control in the smart charging station not only helps to reduce the steady-state error and accelerate the smart charging station to the steady operation point, but also supplies either positive or negative damping torque into the system. It demonstrates conclusion (1) obtained in Section 3.

5.3 Case B: utilizing PI control in the smart charging station and fixing output power of the synchronous machine

A comparison of the damping torques is made under different charging or discharging power capacities of the smart charging station with the fixed output power of the synchronous machine. The computational results of the example system are shown in **Table 2**, when active power supplied by the synchronous machine is fixed at 10 MW. From **Table 2**, it can be concluded that:

1. While the output of the synchronous machine is constant, the damping torque from the excitation system of the synchronous machine is nearly unchanged. The signals ΔU_{dc} and ΔU_{qc} through path a and path b only contribute slight changes to ΔT_{dt-ex} . The variety of total damping torque contribution ΔT_{dt} is mainly induced from ΔT_{dt-sp} which comes from the smart charging station and directly affects the oscillation loop. It demonstrates conclusion (2) obtained in Section 3.
2. The damping torque from the smart charging station changes at its different charging or discharging capacity, which is either positive or negative. The smart charging station can help to improve the damping with certain charging capacity which is between the lower and upper threshold. In charging mode, the smart charging station is preferred to operate around 10 MW which is nearly the same as 10.4 MW calculated by Eq. (8). The highest total damping

$P_t/(10 \text{ MW})$	$P_{PEV}/(10 \text{ MW})$	$\Delta T_{dt}/pu$	$\Delta T_{dt-sp}/pu$	$\Delta T_{dt-ex}/pu$	Frequency/Hz	Damping ratio/%
1.0	3.0	0.0633	-0.3182	0.3815	1.69	2.38
1.0	2.5	0.1560	-0.2452	0.4021	1.72	2.51
1.0	2.0	0.3742	-0.0457	0.4199	1.74	2.88
1.0	1.5	0.8400	0.3798	0.4602	1.75	3.71
1.0	1.0	1.0677	0.5806	0.4871	1.76	4.10
1.0	0.5	0.8180	0.3699	0.4481	1.75	3.67
1.0	0.0	0.3523	-0.0582	0.4105	1.74	2.84
1.0	-0.5	0.1398	-0.2593	0.3991	1.72	2.48
1.0	-1.0	0.0227	-0.3370	0.3597	1.70	2.29

Table 2. Computational results of the example system when active power supplied by the synchronous machine is fixed at 10 MW.

torque and damping torque from the smart charging station coincided at the same point. It demonstrates conclusion (3) obtained in Section 3. Under this operation point, the smart charging station just consumes the electricity generated by the equivalent synchronous machine. There is no active power exchange in the tie-line. Beyond or below this point, the damping ratio of the system will decrease because of the increased load burden in the tie-line either from the synchronous machine to the infinite bus or vice versa. Considering each vehicle can draw ± 3.5 kW of active power [25] and always around 60% personal vehicles in the parking lots need to be charged [26], roughly 5000 personal vehicles are optimal to be accepted in this equivalent smart charging station.

3. During the discharging process, the damping of the system tends to deteriorate with the increasing power injected from the smart charging station to grid.

5.4 Case C: utilizing PI control in the smart charging station and fixing load-flow in the tie-line

A comparison of the damping torques is made under different charging or discharging power capacities of the smart charging station with the fixed load-flow in the tie-line. The results are shown in **Table 3**.

From **Table 3**, it can be concluded that:

1. The total damping torque contribution ΔT_{dt} is simultaneously influenced by ΔT_{dt-sp} which relates to $\Delta\delta$ and directly affects the oscillation loop, and ΔT_{dt-ex} which relates to $\Delta E'_q$ and functions through the excitation system.
2. The damping torque supplied from the smart charging station and the excitation system of the synchronous machine respectively is complementary during the charging process. Compared with **Table 1**, the positive damping torque supplied by the smart charging station helps the system to improve the low damping capacity from 5 to 15 MW in charging mode of the smart charging station. This conclusion can be confirmed by the analysis from Eqs. (5) and (6). When the charging power of the smart charging station is between 0 and 30 MW, the product of ΔT_{dt-sp} and ΔT_{dt-ex} is negative.

$P_t/$ (10 MW)	$P_{PEV}/$ (10 MW)	$\Delta T_{dt}/pu$	$\Delta T_{dt-sp}/pu$	$\Delta T_{dt-ex}/pu$	Frequency/ Hz	Damping ratio/%
4.0	3.0	0.3144	-0.2878	0.6022	1.72	2.80
3.5	2.5	0.5527	-0.2122	0.7649	1.72	3.24
3.0	2.0	0.3902	-0.0082	0.3984	1.72	2.94
2.5	1.5	0.1770	0.3152	-0.1382	1.73	2.53
2.0	1.0	0.0093	0.5294	-0.5201	1.73	2.22
1.5	0.5	0.1693	0.3122	-0.1429	1.73	2.52
1.0	0.0	0.3523	-0.0582	0.4105	1.74	2.84
0.5	-0.5	0.5062	-0.2091	0.7153	1.73	3.14
0.0	-1.0	0.2971	-0.2908	0.5879	1.73	2.75

Table 3.
 Computational results of the example system when load-flow in the tie-line is fixed at 10 MW.

3. The impact of the damping torque from the synchronous machine also needs to be considered. With this impact, the highest total damping torque and damping torque from the smart charging station are obtained at different points. In this case, the optimized operation point reaches 25 MW which is nearly the same as 24.6 MW calculated by Eq. (8). It demonstrates conclusion (3) in Section 3. Under the operating conditions that the absorbed power of the smart charging station varies from 20 to 25 MW, although the smart charging station supplies the negative damping torque into the grid, the total damping torque is still positive and keeps increasing with the compensation of the damping torque from the excitation system. The smart charging station at the optimal operation point is also charged by the electricity generated by the equivalent local synchronous machine.
4. The damping of the system tends to deteriorate with the increasing power injected from the smart charging station to the grid during the discharging process.

5.5 Case D: stabilizer design

While the operation condition for the smart charging station varies stochastically, the stabilizer is designed and attached to the smart charging station to supply additional damping torques into the system.

The stabilizer via the active and reactive power loops is designed respectively under the condition that the equivalent synchronous machine supplies 20 MW and the smart charging station consumes 10 MW of active power. A three-phase short-circuit fault happens in Bus s at 0.5 s and lasts for 0.1 s.

The forward path is:

$$\begin{cases} F_{\text{pssp}}(s) = -6.8751 + j6.8293 \\ F_{\text{pssq}}(s) = 1.7520 + j7.2841 \end{cases} \quad (13)$$

The parameters of the designed stabilizer attached to active and reactive power regulators, respectively, are (Table 4).

With the designed stabilizer, the eigenvalue of the system with the smart charging station can be obtained as that, the effectiveness of the designed stabilizers is verified by the time-domain simulation in Figure 6 and eigenvalue calculation in Table 5. From Table 5 and Figure 6, it can be seen that the designed stabilizer attached to the smart charging station can not only help to reduce the power fluctuations for PEV charging, but also suppress the power oscillation in the tie-line.

5.6 Case E: analysis in the four-machine power system

The power system integrated with the smart charging station is shown in Figure 7. The Prony method is employed to analyze the time-domain simulation of the power flow in the tie-line L6-7 [27]. The critical inter-area electromechanical

Stabilizer	Parameters
Stabilizer via active power regulator	$T_1 = T_3 = 0.0195; T_2 = T_4 = 0.5; K_W = 16.5704$
Stabilizer via reactive power regulator	$T_1 = T_3 = 0.0810; T_2 = T_4 = 0.5; K_W = 12.6289$

Table 4.
Parameters of smart charging station-based stabilizers.

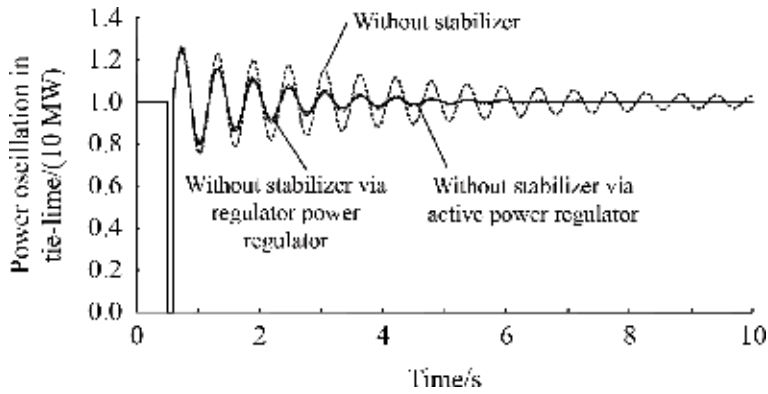


Figure 6. Comparisons of tie-line power oscillation without and with the stabilizer via active and reactive power regulators under $P_{PEV} = 10$ MW, $P_t = 20$ MW.

Without the stabilizer	$-0.2419 + j10.8644$
With the stabilizer via active power regulator	$-0.7590 + j10.8169$
With the stabilizer via reactive power regulator	$-0.6511 + j10.8471$

Table 5. Eigenvalue of the oscillation mode without and with stabilizers under PPEV 10 MW, Pt 20 MW.

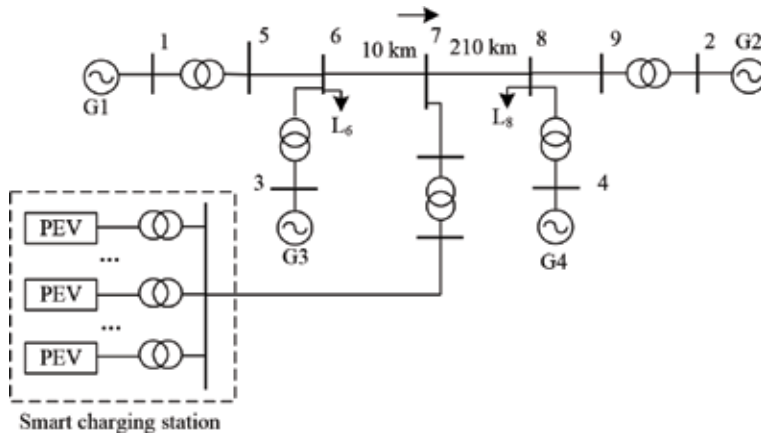


Figure 7. Four-machine power system integrated with the smart charging station.

oscillation frequency $f_{critical}$ and its corresponding attenuation factor $\alpha_{critical}$ are extracted. The eigenvalue of the critical oscillation mode is $\lambda_{critical} = \alpha_{critical} + j2\pi f_{critical}$.

With the load-flow in the tie-line L_{6-7} fixed at 70 MW, a comparison is done between the proportional controlled smart charging station and the adjustable load/generator connected at Bus 7, respectively. The eigenvalue related to the inter-area oscillation mode is a concern. From **Table 6**, only the proportional controlled smart charging station functions as the adjustable load during charging period and as the regulable generator in discharging mode in view of the damping ratio.

Proportional control of the smart charging station only supplies the synchronous torque and integral control that introduces the damping torque into the grid.

$P_{G2}/$ (10 MW)	$P_{PEV}/$ (10 MW)	Frequency/ Hz	Damping ratio/%	Adjustable load/ generator ⁺ /(10 MW)	Frequency/ Hz	Damping ratio/%
9.0	3.0	0.4724	3.12	3.0	0.4724	3.12
8.5	2.5	0.4710	3.14	2.5	0.4710	3.14
8.0	2.0	0.4693	3.15	2.0	0.4693	3.15
7.5	1.5	0.4672	3.16	1.5	0.4672	3.16
7.0	1.0	0.4650	3.15	1.0	0.4650	3.15
6.5	0.5	0.4624	3.13	0.5	0.4624	3.13
6.0	0.0	0.4595	3.11	0.0	0.4595	3.11
5.5	-0.5	0.4564	3.07	-0.5	0.4564	3.07
5.0	-1.0	0.4530	3.01	-1.0	0.4530	3.01

⁺ denotes the adjustable load absorbing active power from the grid; ⁻ denotes the regulable generator injecting active power into the grid.

Table 6. Comparison of eigenvalue related to inter-area oscillation mode only utilizing the proportional control of the smart charging station.

$P_{G2}/$ (10 MW)	$P_{PEV}/$ (10 MW)	Frequency/Hz	Damping ratio/%
9.0	3.0	0.4734	2.52
8.5	2.5	0.4778	2.64
8.0	2.0	0.4802	2.98
7.5	1.5	0.4753	2.56
7.0	1.0	0.4725	2.48
6.5	0.5	0.4683	2.34
6.0	0.0	0.4611	2.25
5.5	-0.5	0.4627	2.30
5.0	-1.0	0.4721	2.39

Table 7. Comparison of eigenvalue related to the inter-area oscillation mode utilizing PI control of the smart charging station.

Conclusion (1) obtained in the single-machine infinite-busbar power system is also available in the multi-machine power system.

Both proportional and integral controls are utilized in the smart charging station. A comparison is done under different charging or discharging power capacities of the smart charging station when the load-flow in the tie-line is fixed at 70 MW. The eigenvalue related to the inter-area oscillation mode is concerned. The results are shown in **Table 7**.

From **Table 7**, the optimal charging point with the highest damping ratio in the single-machine power system can be obtained by Eq. (8) and verified by the damping torque calculation; and it also exists in the multi-machine power system. But, because of the complex interconnection of the synchronous machines and the

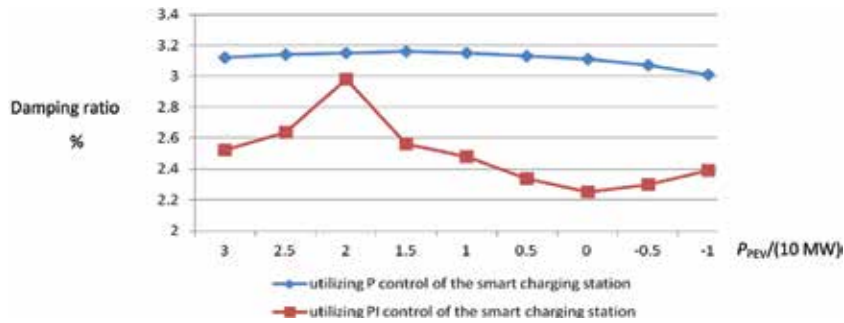


Figure 8. Comparison of damping ratio related to inter-area oscillation mode utilizing the P and PI control of the smart charging station, respectively.

smart charging station, it is difficult to calculate the optimal charging point in theory (Figure 8).

6. Conclusion

The chapter investigates the impacts of a grid-connected smart charging station on power system's small-signal stability based on a simple single-machine infinite-bus power system integrated with a smart charging station. Damping torque analysis (DTA) is employed to examine the contribution from the smart charging station to the electromechanical oscillation loop of the generator in theoretical analysis. The analysis has concluded that, the smart charging station affects power system's small-signal stability in light of its interaction with the synchronous machine. The proportional controls in the smart charging station mainly induce the synchronous torque into the oscillation loop and the majority of damping torque is introduced by integral controls. The damping torque supplied by the smart charging station is mainly directly induced into the oscillation loop, and the damping torque from the excitation system is almost from the synchronous machine itself. The optimal operation condition of the smart charging station is the moment when the system has the highest damping ratio. In this chapter, such an optimal operation condition is defined, indicating that the optimal charging capacity is considered for smart charging station design.

Results of the damping torque computation of a single-machine power system integrated with a smart charging station, confirmed by eigenvalue calculations of system oscillation mode, are presented in the chapter. The conclusions obtained from the theoretical analysis are demonstrated and verified by these results. Under the optimal operation condition, the total damping torque supplied from the smart charging station and synchronous machine reaches its maximum value. During the discharging process, the damping of the system tends to deteriorate with the increasing power injected from the smart charging station to the grid. Another four-machine power system is employed to manifest that the conclusions obtained in the single-machine power system are also available in the multi-machine power system.

The stabilizer is designed and attached to the active or reactive power regulator of the smart charging station to supply additional positive damping into the system. The phase compensation method is used here. The effectiveness is confirmed by the

nonlinear simulations and eigenvalue calculations in the single-machine power system.

Although the configuration of the power system with the grid-connected smart charging station and the function to describe the charging/discharging behaviors of EVs adopted in this chapter are very simple, all the essential elements have been included to serve the purpose of study, which can thoroughly reveal the dynamic interaction between the equivalent smart charging station and conventional generation in the transmission system. The optimal charging capacity is better to be considered during the capacity design of the smart charging station. With the help of the designed smart charging station-based stabilizer, the small-signal stability can be effectively maintained. Studies on the interactions among several smart charging stations with the dynamic stability in distribution systems and the uncertainties and diversities of EV charging/discharging behaviors will be carried out for future researches.

A. Appendix: the parameters of example systems

1. Single-machine infinite-busbar power system.

The parameters of the synchronous machine (The unit is in pu):

$$M = 5.0; T'_{d0} = 5.0 \text{ s}; D = 1.2; X_d = 0.8; X_q = 0.4; X'_d = 0.05; \omega_0 = 2 \times 50\pi; \\ U_t = 1.05; U_{\text{tref}} = 1.05; K_a = 20.0; T_a = 0.01 \text{ s}.$$

The parameters of the network (The unit is in pu): $X_{\text{ts}} = 0.2; X_{\text{sb}} = 0.1; \\ X_s = 0.1; U_b = 1.0.$

The parameters for the smart charging station(The unit is in pu):

$$K_{\text{PP}} = 20, K_{\text{IP}} = 20, K_{\text{PI}_q} = 0.3, K_{\text{II}_q} = 0.3, K_{\text{PQ}} = 15, K_{\text{IQ}} = 15, K_{\text{PI}_d} = 0.7, \\ K_{\text{II}_d} = 0.7.$$

2. Four-machine power system.

The parameters of the synchronous machine are:

$$T_{J1} = T_{J2} = 117; T_{J3} = T_{J4} = 111.15; T'_{d01} = T'_{d02} = T'_{d03} = T'_{d04} = 8.0 \text{ s}; \\ D_{\text{mac1}} = D_{\text{mac2}} = D_{\text{mac3}} = D_{\text{mac4}} = 5.0 \text{ pu}; X_{d1} = X_{d2} = X_{d3} = X_{d4} = 0.2; \\ X_{q1} = X_{q2} = X_{q3} = X_{q4} = 0.1889; X'_{d1} = X'_{d2} = X'_{d3} = X'_{d4} = 0.0333; \\ \omega_{01} = \omega_{02} = \omega_{03} = \omega_{04} = 100\pi; U_{t1} = U_{t3} = 1.03; U_{t2} = U_{t4} = 1.01; \\ U_{\text{tref1}} = U_{\text{tref3}} = 1.03; U_{\text{tref2}} = U_{\text{tref4}} = 1.01.$$

All the generators are equipped with the same AVR: $K_a = 50; T_a = 0.55 \text{ s};$

The parameters of the smart charging station are (in pu):

$$K_{\text{PP}} = 20, K_{\text{IP}} = 20, K_{\text{PI}_q} = 0.3, K_{\text{II}_q} = 0.3; \\ K_{\text{PQ}} = 15, K_{\text{IQ}} = 15, K_{\text{PI}_d} = 0.7, K_{\text{II}_d} = 0.7.$$

The parameters of the lines are (in pu): $X_{15} = X_{36} = X_{29} = X_{48} = 0.01667; \\ X_{56} = X_{89} = 0.025; X_{67} = 0.105; X_{78} = 0.005.$

G1 is connected with the slack bus of the system. G3 and G4 generate 70 MW of active power, respectively. The loads at Bus 6 and Bus 8 are 100 and 200 MW accordingly.

Acknowledgements

The authors would like to acknowledge the support of Dr. Tim Littler from Queen's University, Belfast, UK.

Author details

Cai Hui

State Grid Jiangsu Economic Research Institute, Nanjing, P.R. China

*Address all correspondence to: caihui300@hotmail.com

IntechOpen

© 2019 The Author(s). Licensee IntechOpen. This chapter is distributed under the terms of the Creative Commons Attribution License (<http://creativecommons.org/licenses/by/3.0>), which permits unrestricted use, distribution, and reproduction in any medium, provided the original work is properly cited. 

References

- [1] Zhenya L. *Electric Power and Energy in China*. Beijing: China Electric Power Press; 2012. pp. 124-135 (in Chinese). ISBN: 978-7-5123-2667-5
- [2] Zheng J, Mehndiratta S, Guo JY, et al. Strategic policies and demonstration program of electric vehicle in China. *Transport Policy*. 2012;**19**(1):17-25. DOI: 10.1016/j.tranpol.2011.07.006
- [3] Bowen Z, Littler T. Local storage meets local demand: A technical solution to future power distribution system. *IET Generation, Transmission and Distribution*. 2016;**10**(3):704-711. DOI: 10.1049/iet-gtd.2015.0442
- [4] Venayagamoorthy GK. SmartParks for short term power flow control in smart grids. In: *IEEE International Electric Vehicle Conference (IEVC) 2012*. Greenville, USA: IEEE; 2012. pp. 1-6. DOI: 10.1109/IEVC.2012.6183288
- [5] Mitra P, Venayagamoorthy GK. SmartPark as a virtual STATCOM. *IEEE Transactions on Smart Grid*. 2011;**2**(3): 445-455. DOI: 10.1109/TSG.2011.2158330
- [6] Mitra P, Venayagamoorthy GK. Intelligent coordinated control of a wind farm and distributed SmartParks. In: *IEEE Industry Application Society Annual Meeting (IAS) 2010*. Houston, USA: IEEE; 2010. pp. 1-8. DOI: 10.1109/IAS.2010.5615930
- [7] Tomic J, Kempton W. Using fleets of electric drive vehicles for grid support. *Journal of Power Sources*. 2007;**168**(2): 459-468. DOI: 10.1016/j.jpowsour.2007.03.010
- [8] Venayagamoorthy GK, Sharma RK, Gautam PK. Dynamic energy management system for a smart microgrid. *IEEE Transactions on Neural Networks and Learning Systems*. 2016; **27**(8):1643-1656. DOI: 10.1109/TNNLS.2016.2514358
- [9] Kempton W, Tomic J. Vehicle-to-grid power fundamentals: Calculating capacity and net revenue. *Journal of Power Sources*. 2005;**144**(1):268-279. DOI: 10.1016/j.jpowsour.2004.12.025
- [10] Xifan W, Chengcheng S, Xiuli W, et al. Survey of electric vehicle charging load and dispatch control strategy. *Proceedings of the CSEE*. 2013;**33**(1): 1-10 (in Chinese). Available from: <http://d.wanfangdata.com.cn/Periodical/zgdjgxcb201301001>
- [11] Kempton W, Tomic J. Vehicle-to-grid power implementation: From stabilizing the grid to support large-scale renewable energy. *Journal of Power Sources*. 2005;**144**(1):280-294. DOI: 10.1016/j.jpowsour.2004.12.022
- [12] Liting T, Mingxia Z, Wang H. Evaluation and solutions for electric vehicles' impact on the grid. *Proceedings of the CSEE*. 2012;**32**(31): 43-49 (in Chinese). Available from: <http://d.wanfangdata.com.cn/Periodical/zgdjgxcb201231006>
- [13] Huston C, Venayagamoorthy GK, Corzine K. Intelligent scheduling of hybrid and electric vehicle storage capacity in a parking lot for profit maximization in grid power transaction. In: *Proceedings of IEEE Energy 2030*. Atlanta, USA: IEEE; 2008. pp. 1-8. DOI: 10.1109/ENERGY.2008.4781051
- [14] Zhengshuo L, Hongbin S, Guo Q, et al. Study on wind-EV complementation on the transmission grid side considering carbon emission. *Proceedings of the CSEE*. 2012;**32**(10): 41-48 (in Chinese). Available from:

http://explore.bl.uk/primo_library/libweb/action/display.do?tabs=detailsTab&gathStatTab=true&ct=display&fn=search&doc=ETOCRN613373549&indx=1&recIds=ETOCRN313900056

[15] Xiaoyan Y, Chunlin G, Xuan X, Dequan H, Zhou M. Research on large scale electric vehicles participating in the economic dispatch of wind and thermal power system. In: 2017 China International Electrical and Energy Conference. 2017. pp. 223-228. DOI: 10.1109/CIEEC.2017.8388450

[16] Hua P, Zuofang L, Qianzhong X. Economic dispatch of power system including electric vehicle and wind farm. In: 2017 IEEE Conference on Energy Internet and Energy System Integration. 2017. pp. 1-5. DOI: 10.1109/EI2.2017.8245238

[17] Beck LJ. V2G—101, a text about vehicle-to-grid (V2G), the technology which enables a future of clean and efficient electric-powered transportation. USA:V2G-101 Copyright; 2009. pp. 10-25

[18] Yaonan Y. Electric Power System Dynamics. New York: Academic Press; 1983. pp. 79-94. ISBN: 0127748202

[19] Wenjuan D, Haifeng W, Jun C. Model and theory of PSS localized phase compensation method. Proceeding of the CSEE. 2012;**32**(19):36-41 (in Chinese)

[20] Wenjuan D, Haifeng W, Jun C. Application of localized phase compensation method to design a stabilizer in a multi-machine power system. Proceeding of the CSEE. 2012; **32**(22):73-78 (in Chinese). Available from: http://explore.bl.uk/primo_library/libweb/action/display.do?tabs=detailsTab&gathStatTab=true&ct=display&fn=search&doc=ETOCRN613373549&indx=1&recIds=ETOCRN011774271

ETOCRN613373549&indx=1&recIds=ETOCRN320143870

[21] Lingling Y, Wenjuan D, Yizhang Y, Yanfeng G. Methods of DTA to estimate the impact of integration of DFIG on single-machine infinite-bus power system. In: 2016 China International Conference on Electricity Distribution. 2016. pp. 1-5. DOI: 10.1109/CICED.2016.7576247

[22] Wenjuan D, Haifeng W, Liye X. Power system small-signal stability as affected by grid-connected photovoltaic generation. European Transactions on Electrical Power. 2012; **22**(5):688-703

[23] Wenjuan D, Haifeng W, Hui C. Modeling a Grid-connected SOFC power plant into power systems for small-signal analysis and control. European Transactions on Electrical Power. 2012;**23**(3):330-341. DOI: 10.1049/cp.2011.0208

[24] Haifeng W, Swift FJ. The capability of the static var compensator in damping power system oscillations. IEE Proceedings of Generation, Transmission and Distribution. 1996; **143**(4):353-358 Available from: https://explore-bl-uk.vpn.seu.edu.cn/primo_library/libweb/action/display.do?tabs=detailsTab&gathStatTab=true&ct=display&fn=search&doc=ETOCRN613373549&indx=1&recIds=ETOCRN011774271

[25] Majeau-Bettez G, Hawkins TR, Stroemman AH. Life-cycle environmental assessment of lithium-ion and nickel metal hydride batteries for plug-in hybrid and battery electric vehicles. Environmental Science and Technology. 2011;**45**(10):4548-4554

[26] Stikes K, Gross T, Lin Z, et al. Plug-in Hybrid Electric Vehicle Market Introduction Study: Final Report.

Washington, DC: Tech. Rep.
DE2010-972306; 2010

[27] Guoqiang H, Renmu H, Huachun Y, et al. Iterative prony method based power system low frequency oscillation mode analysis and PSS design. In: 2005 IEEE/PES Asia and Pacific Transmission and Distribution Conference and Exhibition. Dalian, China: IEEE; 2005. pp. 1-6. DOI: 10.1109/TDC.2005.1546867

Section 2

**Power Oscillations and
Electrical Infrastructures**

Power Oscillation Due to Ferroresonance and Subsynchronous Resonance

Salman Rezaei

Abstract

Power oscillation occurs in electrical network due to variety of phenomena. Subsynchronous resonance (SSR) and ferroresonance are the phenomena that cause power oscillation of rotary systems. Ferroresonance is likely to occur due to traversing capacitance line of the system across nonlinear area of transformer saturation curve due to several configurations like breaker failure, voltage transformer connected to grading capacitor circuit breaker, line and plant outage, etc. It causes misshaping the waveforms and frequency difference between two points in the network. Frequency difference (Δf) results in oscillation of power with a swing frequency which is equal to Δf . During SSR, electrical energy is exchanged between generators and transmission systems below power frequency. It happens due to interaction of a series compensated transmission line with a generator. It results in oscillation in the shaft and power oscillation. In addition, SSR causes the magnitudes of voltage and current to increase. Increasing the voltage causes saturation of iron core of transformer or reactor and consequently occurrence of ferroresonance in the presence of series capacitance.

Keywords: power oscillation, ferroresonance, subsynchronous resonance, series compensation, saturation, frequency difference, Manitoba hydro, Mohave plant

1. Introduction

The word ferroresonance was originally expressed in 1920 to explain the phenomenon of two stable fundamental frequency operating points in a series resistor, nonlinear inductor, and capacitor circuit [1]. It has been extensively studied over the past 90 years. Severity of ferroresonance is classified as four categories like fundamental, harmonic, quasi-periodic, and chaotic [2]. Ref [3] explains Conventional configurations which lead in ferroresonance like; voltage transformer (VT) energized through the grading capacitance of open circuit breakers or VT connected to an ungrounded neutral system, circuit breaker failure during opening or closing operation, and power transformer supplied through a long transmission line cable with low short-circuit power [3]. Several methods have been presented to analyze ferroresonance in time and frequency domain. Ref. [4] is concerned with comparing analytical nonlinear dynamics methods with a two-dimensional (2-D) brute-force bifurcation diagram for displaying safety margins in a 2-D parameter space.

Analysis and mitigation of ferroresonant oscillations based on harmonic balance method and bifurcation theory are presented in [5].

Ferroresonance generally occurs in distribution network and is significantly probable in HV systems [6–8]. For instance, plant outage in HV power system is able to change electrical characteristics and parameters in a nonlinear circuit, which may lead in ferroresonance [9].

Impact of ferroresonance has been taken into consideration in wind farm. Ref. [10] presents the scenarios that can lead to ferroresonant circuits in Doubly Fed Induction Generator (DFIG)-based wind parks. Transient and sustained ferroresonance phenomenon in wind farms connected to a power distribution system is analyzed in [11]. Occurrence of ferroresonance causes misshaped waveform of magnitudes with different frequencies. It leads in power oscillation between two points with a certain frequency difference in the network [12]. Ferroresonance is typically damped by using several methods. For instance, installation of permanent resistance in the secondary circuit of distribution transformer; furthermore, replacing VT with CVT causes mitigation of ferroresonance in voltage transformer [6].

The term of SSR has been taken into consideration in the power industry since first experienced in 1970. It results in shaft failure of units at Mohave power plant. The second failure was the real cause of failure recognized as SSR in 1971 [13].

Many investigations have been implemented in analysis and mitigation of SSR. By bifurcation analysis, the stable limit cycle bifurcates to a stable torus and an unstable limit cycle, which connects to a stable limit cycle by a supercritical torus bifurcation [14]. Frequency scanning computes the equivalent resistance and inductance, seen looking into the network from a point behind the stator winding of a generator as a function of frequency [15]. Design and implementation details of an artificial neural network-based SSR are presented in [16]. Time frequency distribution algorithm extracts time variable information about frequency contents from the time domain signal [17].

For the mitigation of SSR, several methods have been presented. STATCOM is used in the transformer bus to damp SSR [18]. Application of gate-controlled series capacitors (GCSC) for reducing stresses due to SSR in turbine-generator shaft is presented in [19]. Fuzzy logic and ANFIS controller-based Static Var Compensation (SVC) for mitigating SSR is explained in [20].

SSR has received considerable attention in the wind farm. SSR analysis on DFIG-based wind farm and optimal adaptive controls to mitigate SSR in wind farm are presented in [21, 22].

SSR causes subharmonic components of electrical quantities to interact with natural frequencies of rotary systems due to series capacitance. It leads in torsional oscillation of the turbo-generator shaft. Torsional oscillation in the shaft results in out of step condition of the generator. It increases the magnitudes of voltage and current. Increasing the voltage causes saturation of transformer and probable occurrence of ferroresonance in a series compensated network [23, 24]. Oscillation due to ferroresonance is superimposed on torsional oscillation in SSR.

In this chapter, theoretical approach of ferroresonance and SSR is presented. Manitoba hydro electrical network has experienced ferroresonant states in 1995 [8]. In addition, it includes long transmission line of about 500 km, which is suitable for series compensation studies [6]. Hence, it is a good example of a case study in this field. The state that results in ferroresonance is simulated in Manitoba hydro system by PSCAD/EMTDC. Power oscillation due to SSR and ferroresonance is presented in HV power system, and results of oscillation are analyzed on electrical and mechanical parameters of rotary systems including hydro generator in Grand Rapids station.

2. Theoretical approach of ferroresonance and subsynchronous resonance

2.1 Ferroresonance

Ferroresonance is a nonlinear resonance, which occurs in presence of a saturable nonlinear inductance and capacitance in a circuit with low resistance. In ferroresonance, the capacitance line crosses inductance characteristic in nonlinear area. It results in presence of abnormally large currents and frequency distortion.

A graphical approach is obtained by calculating the parameters of nonlinear circuits in time domain. For instance, in a typical series, RLC circuit inductor voltage is calculated as follows [6]:

$$V_L = \sqrt{V_h^2 - (I.R)^2} + \frac{I}{\omega C} \quad (1)$$

It is also a nonlinear function of current as follows:

$$V_L = \omega f(I) \quad (2)$$

The inductance in this circuit is a nonlinear element due to the core saturation and hysteresis. The voltage across the capacitance in the circuit is represented as:

$$V_C = I/\omega C \quad (3)$$

where V_h is the total voltage across the circuit. Similarly, the voltage across the inductance can also be expressed as:

$$V_L = V + (I/\omega C) \quad (4)$$

As shown in **Figure 1**, point of intersection of $V_L = \omega f(I)$ and V_C represents the operating point of the circuit. Changing the capacitance of the system causes change in the slope given by $\tan \alpha = 1/\omega C$. On the other hand, changes in inductance result in an interaction with a wide range of circuit capacitances resulting in existence of several stable steady state responses to any given change of parameter. It causes changes in configuration of the circuit, and so capacitance traverses across nonlinear area of $V_L = \omega f(I)$ curve and results in occurrence of ferroresonance in the circuit.

As was mentioned above, frequency of waveform can be deviated from nominal frequency in ferroresonance so that frequency deviation can be defined as follows

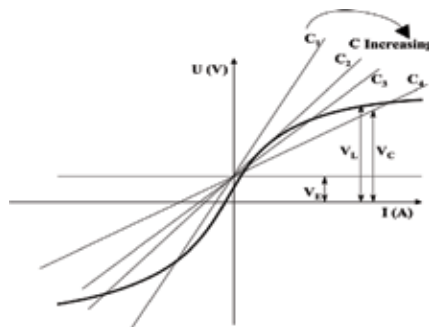


Figure 1.
 Diagram of parameters in series RLC ferroresonant circuit.

$$\Delta f = |f_{fr} - f_{nom}| \quad (5)$$

where f_{fr} is the frequency of waveform in ferroresonance.

Resulted waveform is decomposed to its number of harmonics using fast Fourier transform (FFT). Measurement is done by evaluation of samples, which are taken in specific sampling interval; hence, discrete Fourier transform (DFT) is used with a certain sampling rate to illustrate harmonic components on harmonic spectrum.

$$V_{Lk} = \sum_{n=0}^{N-1} V_{Ln} e^{-j2\pi k \frac{n}{N}} \quad K = 0 \dots N - 1 \quad (6)$$

N = number of samples.

Then, total harmonic distortion is calculated, and so integer harmonics, which obtained from FFT, are considered in the following formula:

$$THD = \sqrt{\sum_{h=2}^x \left(\frac{\text{individual } (h)}{\text{individual } (1)} \right)^2} \quad (7)$$

where x is integer harmonics.

In order to determine ferroresonance based on measurement in a logical manner, ferroresonant characteristics must be quantified. THD and Δf are the quantities that are used as criteria to determine ferroresonance of different types (**Table 1**).

As shown in the table, fundamental ferroresonance is detected when frequency of waveform remains at nominal value (Δf is zero) and the value of THD is more than 50%. Harmonic ferroresonance is detected when frequency of waveform is deviated from nominal value and remains constant (Δf is not zero); furthermore, the value of THD is also more than 50%. In most cases, fundamental and harmonic ferroresonance contain odd harmonics; hence, harmonic spectrum is discrete. Quasi-periodic and chaotic modes are determined when $\frac{d\Delta f}{dt}$ is detected and calculated as follow.

$$\frac{d\Delta f}{dt} = T \cdot \frac{\Delta f(t) - \Delta f(t - \Delta t)}{\Delta t} \quad (8)$$

where T is the time constant, $t - \Delta t$ is the previous time step, and Δt is the time step interval.

Furthermore, the value of THD increases more than 100% where chaotic mode contains a continuous harmonic spectrum. As harmonic spectrum is mostly a qualified characteristic, THD and Δf are used to determine ferroresonance modes.

2.2 Subsynchronous resonance

In this section, theoretical aspects of SSR in AC transmission system are explained.

Ferroresonance type	Δf	$\frac{d\Delta f}{dt}$	THD (%)	Harmonic spectrum
Fundamental	Zero	Zero	>50	Discrete
Harmonic	Constant	Zero	>50	Discrete
Quasi-periodic	Variable	Not zero	>100	Discrete
Chaotic	Variable	Not zero	>100	Continuous

Table 1.
Criteria to determine ferroresonance modes.

Loadability of AC transmission line is defined as follows:

$$P = \frac{V_S \cdot V_R}{X_T} \sin \delta \quad (9)$$

Series compensation increases transmittable power by adding series capacitors, which decrease total line impedance as follows:

$$X_T = X_L - X_C \quad (10)$$

$$X_T = (1 - S) \cdot X_L \quad (11)$$

Here, S is the compensation degree, which is changed between 0 and 100% defined as follows:

$$S = \frac{X_C}{X_L} \times 100\% \quad (12)$$

The degree of compensation could be 100% theoretically. It may produce large currents in the presence of small disturbances or faults. In other hand, a high level of compensation highlights the problem in protective relays and in voltage profile during fault condition. In a radial series-compensated power system, the electrical resonance frequency is given by the following formula.

$$f_{er} = \pm f_s \sqrt{\frac{X_C}{X_L}} \quad (13)$$

where f_s is power system nominal frequency and X_L is total inductance of the grid.

Current flowing in the grid circulates to the armature winding of the generator and interacts with turbine-generator rotor as subharmonic and super harmonic frequencies. As shown below, the current includes fundamental component (grid frequency), and another sinusoidal components are determined by existing elements in the grid [25].

$$i(t) = K[A \sin(\omega_1 t + \psi_1) + B e^{-\zeta \omega_2 t} \sin(\omega_2 t + \psi_2)] \quad (14)$$

where ζ is damping ratio given by (7).

$$\zeta = \frac{R}{2} \sqrt{\frac{C}{L}} \quad (15)$$

ω_2 is damping frequency as follows:

$$\omega_2 = \omega_n \sqrt{1 - \zeta^2} \quad (16)$$

ω_n is undamped natural frequency as follows:

$$\omega_n = \sqrt{\frac{1}{LC}} \quad (17)$$

Subsynchronous current induced in generator produces torque on the turbine-generator shaft. Subsynchronous torque may coincide with one of the natural frequencies of the rotary system. It causes oscillation of the shaft at some natural frequencies. Subsynchronous resonance can cause catastrophic damage to the

turbine-generator shaft. SSR is generally divided into transient and steady state which are described as follows [26].

Transient SSR occurs due to occurrence of a short circuit in a system with series compensation. Transient magnitudes include subsynchronous frequencies, which depend on elements in the network. Slip frequency f_r in generator is given by (18).

$$f_r = f_0 - f_{er} \quad (18)$$

In case this frequency coincides with one of natural frequencies of the turbine-generator rotor (f_n), torque amplitude is increased much larger with respect to the system without compensation.

Steady state (self-excitation) SSR is divided into the induction generator effect (IGE) and torsional interaction (TI). IGE considers generator as a rigid mass at constant speed connected to the network. TI considers the turbine generator with multimass shaft, which interacts with the system disturbances at its natural frequencies.

3. Power oscillation due to ferroresonance

Catastrophic circumstances and equipment failures in electrical networks are mostly caused by emerging unwanted and unpredicted phenomena in electrical network. Resonance and ferroresonance are those phenomena which have been investigated many years ago. Manitoba hydro 230 kV electrical network has experienced ferroresonant states several times. Such conditions may occur in effect of short circuit, breaker phase failure, transformer energizing, load rejection, accidental or scheduled line disconnection, and plant outage. Power oscillation has been experienced during ferroresonance studies in Manitoba hydro system. In this section, ferroresonant states, which occurred in Manitoba hydro network, are explained, and results are analyzed. The latest studies on ferroresonance in Manitoba hydro system are explained, and power oscillation due to ferroresonance is discussed in this network. In addition to that, impact of ferroresonance on electrical and mechanical parameters of hydro generator is analyzed.

3.1 Ferroresonance accidents in Manitoba hydro system

3.1.1 Failure of wound PT in effect of opening grading capacitance circuit breakers

Manitoba hydro 230 kV electrical network consists of several 230 kV power sources like Vermillion, Dorsey, Ridgway, Rosser, and Grand Rapids station. Furthermore, Ashern station comprises an overvoltage-damping reactor, and Silver station with $2 \times 230/66$ kV, YNd, 50 MVA transformers, is considered for particular ferroresonant investigations [27]. In order to meet a -50°C low temperature specification, circuit breakers used in Dorsey converter station have been provided by SF₆ mixed with CF₄ since 1988. In high voltage systems, multiple interrupting chambers are connected in series to break the current and withstand the high recovery voltage. Grading capacitors with the values of 1500–1600 for an SF₆ breaker are installed in parallel with each chamber to obtain an equal voltage distribution [28].

As shown in **Figure 2**, the 230 kV ac bus in Dorsey HVDC converter station consists of four bus sections. At 22:04, May 20, 1995, bus A2 was disconnected for maintenance. At approximately 22:30, a potential transformer (V13F) failed catastrophically. It caused damage to equipment up to 33 m away. The main reason for

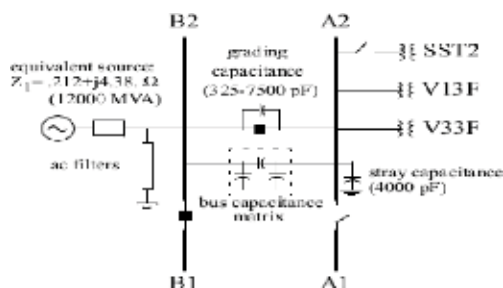


Figure 2.
 Dorsey converter station 230 kV bus arrangement in Failure of wound PT.

PT explosion was occurrence of ferroresonance, which is caused by switching procedure. De-energized bus and the associated PTs were being connected to the energized bus B2 through the grading capacitors (5061 pF) of nine open 230 kV circuit breakers. Station service transformer SST2, which is normally connected to bus A2, had been previously disconnected. This arrangement leads in occurrence of ferroresonance in phase A and B [6].

3.1.2 Energizing induction motor by closing 4.16 kV circuit breaker

Another ferroresonant state occurred on August 5, 1995, at 14:18. A 4.16 kV breaker failed to latch while attempting to energize a 1500 kW induction motor at the Dorsey Converter Station [28]. It resulted in opening eleven 230 kV breakers to clear bus B2 to which the 230/4.16 kV transformer (SST1) was connected. Noise levels of SST1 were significantly higher than normal state. **Figure 3** shows bus arrangement, equivalent source impedance, and capacitances. Misshaped waveforms and voltage increasing near 1.5 pu occurred in bus B2. This is the evidence of existing a steady-state asymmetric fundamental mode of ferroresonance.

3.2 Power oscillation due to ferroresonance examined in Manitoba hydro system

One of the popular configurations, which cause ferroresonance in the network, is transformer-terminated double circuit line. Ferroresonance occurs due to capacitive coupling between double circuit lines. In such configuration, power transformers are connected to de-energized transmission lines of remarkable length, which is parallel to another energized line.

As shown in **Figure 4**, in Manitoba hydro network, 230/66 kV transformers in Silver station are supplied from a single transmission line, which is tapped from A3R line. A double circuit transmission line with a length of about 200 km comprises A3R-A4D lines, which are routed between Ashern and Rosser station. Grand Rapids is connected to Ashern station by G1A-G2A double circuit transmission line with a

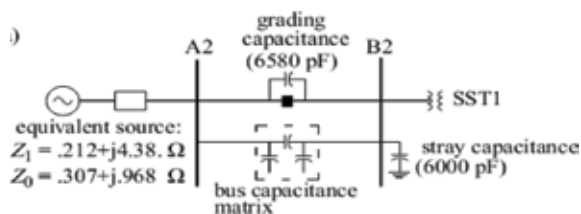


Figure 3.
 Dorsey converter station 230 kV bus arrangement in closing 4.16 kV circuit breaker.

length of about 234 km. Several ferroresonant states, which resulted in power oscillation, were experienced by EMTP are fully explained in [6].

New ferroresonance studies have been implemented in Manitoba hydro system to obtain other configurations vulnerable to ferroresonance in the network [9, 12]. These arrangements comprise breaker phase failure, transformer-terminated double-circuit transmission line, and plant outage. Unlike previous investigations, in obtained ferroresonant arrangements due to transformer-terminated double circuit transmission line, both lines are remained energized. Hence, it is concluded that capacitive coupling of double circuit lines is not the only reason of occurrence of ferroresonance. In the following, one of these configurations is explained.

3.2.1 Disconnection of A3R line from Rosser and G2A line from Grand Rapids station

Figure 4 shows a ferroresonant configuration in Manitoba system. In this arrangement, A3R-A4D and G2A transmission lines are energized by G1A line, which is still connected to Grand Rapids station. In addition, Vermillion is disconnected from Ashern station by a 230 kV circuit breaker in Ashern station. By such switching operation, G2A, A4D, and A3R transmission lines are changed to open-end lines. As was mentioned in advance, in order to supply transformers in Silver station, a 230 kV single line is taped from A3R line of A3R-A4D double circuit line. In such arrangement, transformers in Silver station are located at the end of an open end line whose voltage is increased.

This experiment is represented by two different conditions for a time of about 10 s. In one condition, transformers in Silver station are considered nonsaturated. As shown in **Figure 5**, the magnitude of voltage is increased up to $304 \text{ kV}_{\text{pick prim}}$ (pick value in primary side) in Silver station due to voltage increment in open-end line, whereas this value is $209 \text{ kV}_{\text{pick prim}}$ in normal status. It must be noted that all mentioned voltage and current magnitudes in this paper are phase to neutral values. Oscillograph shows that voltage and current waveforms are not misshaped and remained in sinusoidal form; hence, no ferroresonance occurs in the system. In this experiment, damping reactor in Ashern station is disconnected from the network. In addition, grading capacitor circuit breakers are open in Dorsey converter station.

In another experiment, transformer core is saturated with specified values of magnetizing parameters. Oscillograph shows occurrence of ferroresonance due to

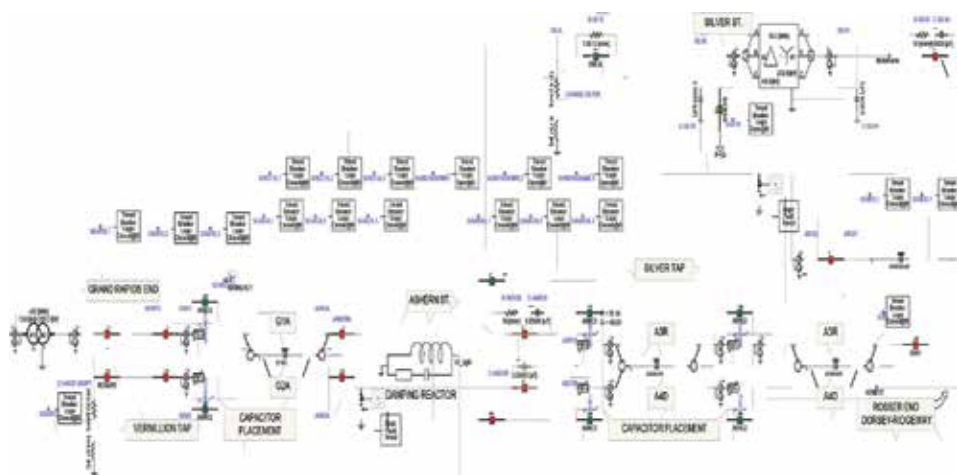


Figure 4. Manitoba hydro network under study in PSCAD/EMTDC.

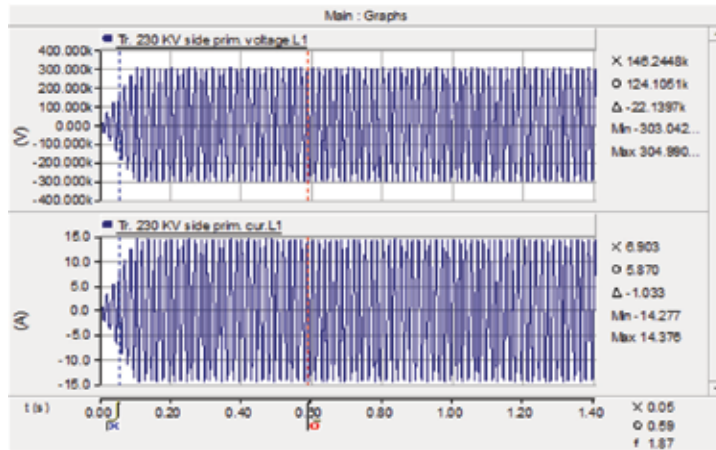


Figure 5.
 Voltage and current waveform of nonsaturated core.

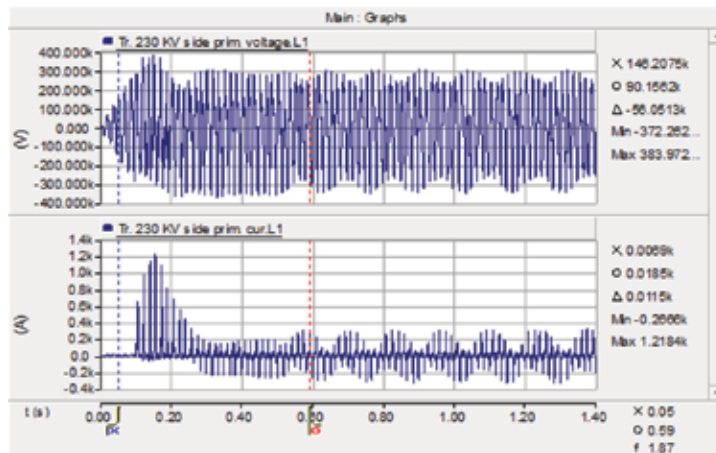


Figure 6.
 Voltage and current waveform of saturated core (ferroresonance).

transformer saturation core. As shown in **Figure 6**, in addition to misshaping the waveforms, the magnitude of voltage and current is increased up to maximum values of about $383 \text{ kV}_{\text{pick prim}}$ and $1.21 \text{ kA}_{\text{pick prim}}$, respectively, at the beginning of ferroresonance.

3.3 Analysis of power oscillation in effect of ferroresonance

In fact, the main reason of occurrence of ferroresonance is existing nonlinear elements in the circuit. Consequently, the voltage and current values are nonlinear with respect to each other due to nonlinear characteristic of elements. It results in misshaping waveforms, and so that they are deviated from sinusoidal form. In such conditions, waveforms comprise orders of harmonics. It definitely depends on nonlinear characteristic of elements in the network. Frequency of total waveform is deviated from nominal frequency due to existing number of harmonics. The resulted frequency of waveform in ferroresonance depends on phase and values of orders with respect to fundamental. Reciprocally, in such conditions, frequency of

the waveform may remain in nominal value in another side of the network or can get different nonlinear characteristic. Consequently, a frequency difference between two points in the network is resulted. The main factor, which results in power oscillation, is frequency difference in the network. Frequency of power oscillation is a function of frequency difference between two points.

As was shown in **Figure 6**, voltage and current oscillate with specific period in effect of ferroresonance. Envelope of misshaped waveforms due to existing number of harmonics in ferroresonance oscillates with a frequency of about 10 Hz. It is resulted from frequency difference of about 10 Hz between Grand Rapids and Silver station.

There is significant difference between power oscillation experienced in ferroresonance and a typical oscillation in case of pole slipping in the generator. As shown in **Figure 7**, in a typical pole slipping in the generator, envelope of voltage swing advances by 180° with respect to the envelope of current swing or vice versa, whereas envelope of voltage swing is the same phase with respect to the envelope of current swing in power oscillation due to ferroresonance. Furthermore, the envelope of power oscillation due to ferroresonance covers negative or positive side

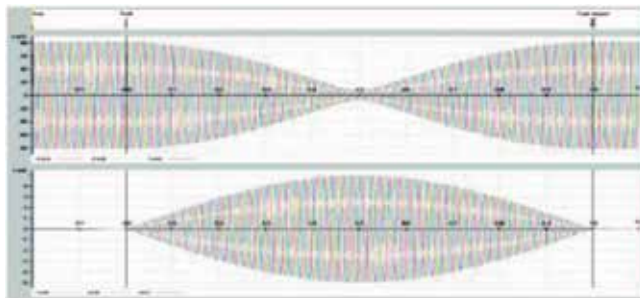


Figure 7.
Typical status of voltage and current in case of pole slipping in generator.

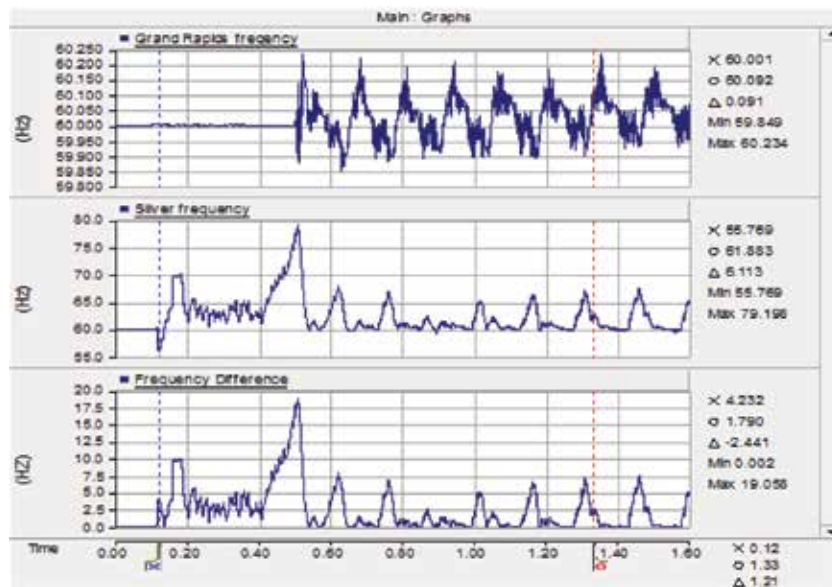


Figure 8.
 Δf between Grand Rapids and Silver station.

sequentially, whereas the same envelope of power covers both negative and positive sides in each period of swing. In addition, in case of power swing in effect of out of step condition in no ferroresonant state, waveform of voltage and current mostly includes fundamental waveform. Consequently, power oscillation in case of pole slipping in the network can be distinguished from oscillation in effect of ferroresonance. It must be noted that, in some cases, electrical parameters in case of pole slipping in generator get different magnitudes and harmonic distortion according to dynamics of generator and power system.

Figure 8 shows frequency difference between Grand Rapids and Silver station during ferroresonance. As it is inferred from diagram, the frequency difference is not constant in the time of ferroresonance. Consequently, period of power oscillation is variable in such conditions.

3.4 Impact of power oscillation in effect of ferroresonance on operation of hydro generator

In order to analyze impact of power oscillation in effect of ferroresonance on operation of hydro generator, Grand Rapids station in Manitoba hydro system is simulated as both equivalent circuit and hydro-generator mode in the software. In

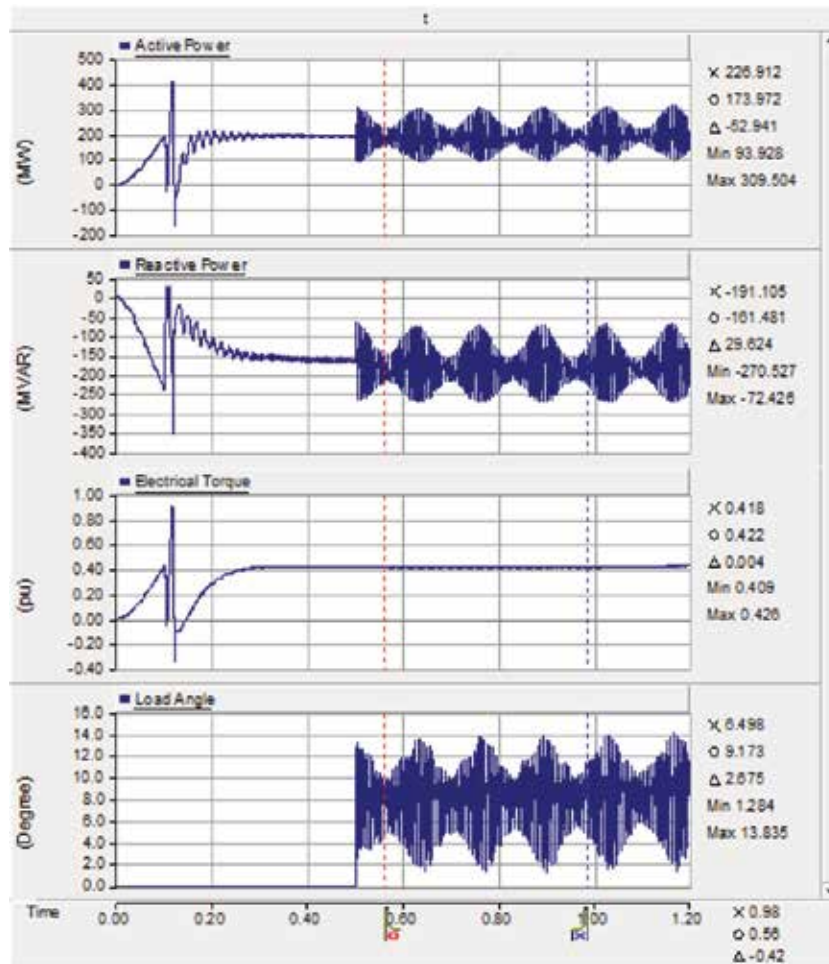


Figure 9. Electrical parameters of hydro generator during ferroresonance.

order to compare behavior of the station in both operation mode and prevent instability due to sudden energizing at the beginning of simulation, the station is changed from equivalent circuit to hydro generator with constant speed along with exciter and PSS in the time of 0.5 s from the beginning of simulation. When the condition is stable, generator is changed to full-blown machine where governor and multi-mass torsional shaft model are also released in the time after 0.1 s. Voltage and current waveforms follow the same oscillations, as well as previous state with a lower magnitude of about $320 \text{ kV}_{\text{pick prim}}$ and $0.380 \text{ kA}_{\text{pick prim}}$, respectively, in generator mode.

Frequency difference between Grand Rapids and Silver station is about 10 Hz when station is in service as equivalent circuit. In such condition, power oscillates from 179 to 212 MW with a frequency of about 10 Hz in the time before 0.5 s.

In the time after 0.5 s (Grand Rapids in generator mode), power oscillation due to ferroresonance affects the stability of hydro generator. As shown in **Figure 9**, ferroresonance causes envelope of power with a frequency of about 16 Hz. Power oscillates increasingly from 93 to 309 MW in the time of about 3 ms in each period of envelope. Hence, frequency of power oscillation in each envelope is 166 Hz.

Electrical and mechanical parameters of hydro generator are shown in **Figures 9** and **10**, respectively. The parameters increase significantly during ferroresonance.

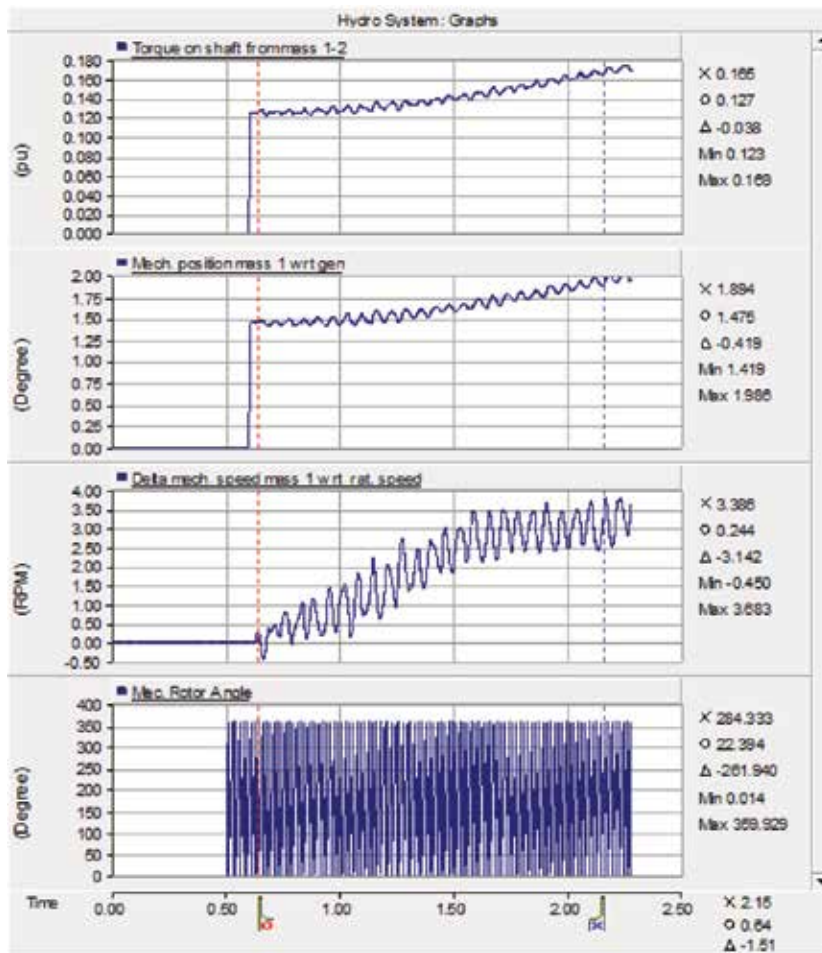


Figure 10. Mechanical parameters of hydro generator during ferroresonance.

Hydro generator will be in unstable condition due to oscillation of parameters, which follows power oscillation in the network. Load angle oscillates as well as real power and increases up to maximum 14° ; however, the value is far from power stability limit, which is defined as 90° . Mechanical parameters of the generator have increasing manner in the time of ferroresonance. Torque on shaft from generator to stage one of hydro turbine increases from 0.12 to 0.16 pu in a duration of 1.5 s. Mechanical displacement of stage 1 of hydro turbine with respect to generator increases from 1.4 to 2° . In addition, mechanical speed difference of the generator with respect to rated speed increases up to 3.6 rpm at the same time. Consequently, frequency oscillates from 59.8 to 60.2 Hz in Grand Rapids station.

4. Power oscillation due to subsynchronous resonance

The phenomenon of subsynchronous resonance on alternating self-excited power oscillation in series compensation line was first treated in the technical literature in the early of 1943. As was discussed in advance, two shaft failures occurred at the Mohave Generating Station in Southern Nevada. In this section, occurrence of SSR in Mohave power plant is explained, and test results are analyzed. Manitoba hydro system with long transmission line of about 500 km is under series compensation studies in 230 kV level. In addition to that, impact of SSR on electrical and mechanical parameters of hydro generator is analyzed.

4.1 Occurrence of subsynchronous resonance in Mohave power plant

Power generation in Mohave plant includes two 909 MVA cross-compound units. **Figure 11** shows arrangement of one unit. The high-pressure (HP) generators comprise two-pole, 483 MVA, 22 kV machines. The low-pressure (LP) generators are four-pole, 426-MVA machines each driven by LP turbine. The cross-compound units are connected to the Mohave 500 kV bus through 825 MVA, 525/22 kV transformer bank. The generation plant and its associated transmission are included into the 500 kV system, which is designed with 70% series compensation. Unit No. 2 Mohave power plant was exposed to failure in the shaft section between the generator and exciter at the main generator collector due to torsional fatigue. The mechanical strain cycling which involved plastic deformations caused the shaft to heat up to temperatures, which resulted in the breakdown of the insulation between the collector rings and the shaft. The heavy current flow that resulted from the positive and negative generator field short circuit eroded large pockets of metal from the shaft and the collector ring. Analysis of line current oscillogram taken during the disturbance on the line indicated the presence of appreciable currents of subsynchronous frequency (lower than 60 Hz).

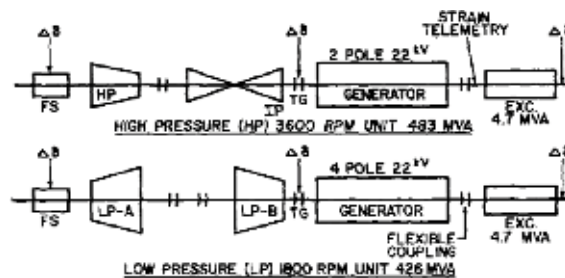


Figure 11.
Mohave generating station 909 MVA cross compound units.

Subsynchronous currents flow in the generator armature and react with the main flux of the generator to increase torque on the shaft at the slip frequency between the rotating main generator flux and the subsynchronous current flowing in the electrical network. The slip frequency following the disturbance, which causes the Mohave failures, coincided with the second flexible torsional natural frequency of the turbine-generator rotor system. It results in amplifying the magnitude of the shaft response torque. For this mode of oscillation, maximum twist occurs in the shaft span between the generator and exciter [29, 30].

4.2 Power oscillation due to SSR examined in Manitoba hydro system

As was shown in advance, Manitoba hydro system comprises G1A-G2A double circuit transmission line, which connects Ashern station to Grand Rapids station with a length of about 234 km. In another side, Ashern station is connected to Rosser station by A3R-A4D double circuit transmission line with a length of about 200 km. Transformers in Silver station are supplied from a single line, which is tapped from A3R line in a distance of about 50 km from Ashern station. As the line comprises three sections, compensation is applied at the beginning of the line in each section individually (Figure 4).

Electrical resonance frequency (f_{er}) generated by the elements of the network including series capacitance produces a frequency in hydro generator in Grand Rapids station. It may coincide with one of natural frequencies of the hydro generator. Rotor shaft comprises a 4-section turbine, generator, and exciter. Natural frequencies of the rotor are categorized in six torsional modes. Table 2 shows electrical specifications of series compensation in each section. F_{er} generated by the elements of the network produce f_r , which may coincide with one of natural frequencies (f_n) of 480-MW hydro generator in Grand Rapids station. Inertia constant, shaft stiffness, and natural frequencies of rotor shaft are shown in Table 3.

G1A-G2A 234 km			A3R-A4D 50 km			A3R-A4D 150 km		
Comp. %	XL (Ω)	C (μ f)	Comp. %	XL (Ω)	C (μ f)	Comp. %	XL (Ω)	C (μ f)
100	50.3	53	100	10.6	250	100	32	83
75	37.5	71	75	7.95	330	75	24	110
50	25.1	105	50	5.3	500	50	18	155
25	12.5	210	25	2.65	990	25	8	330

Table 2.
Specifications of series compensation in the network.

Inertia	Value (s)	Stiffness	Value (pu. T/rad)	F_n (Hz)	Mode
JT1	0.0830	KT1-2	18.0858	51.94	5
JT2	0.1451	KT2-3	33.1075	43.15	4
JT3	0.7864	KT3-4	51.3650	33.31	3
JT4	0.7945	KT4-Gen	68.0483	0.00	0
JGen	0.7859	KGen-Exc	2.117	20.86	1
JExc	0.0284			24.97	2

Table 3.
Values of inertia, stiffness, and natural frequencies of 480 MW hydro generator.

Natural frequencies of the rotor are calculated by eigenvalue analysis and categorized in six torsional modes as shown in **Figure 12** [31–32].

Analysis of SSR is implemented by applying a three-phase fault at 230 kV side in Silver station. Compensation level is set to 75% for all three sections. The fault occurs in the time of 1.2 s from energizing, and then it is removed after 0.2 s, where

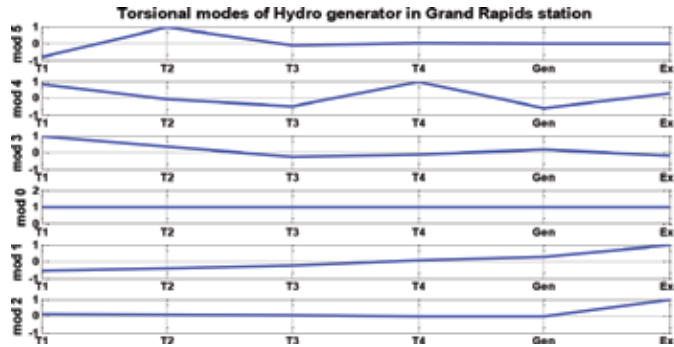


Figure 12.
 Torsional modes of hydro generator in Grand Rapids station.

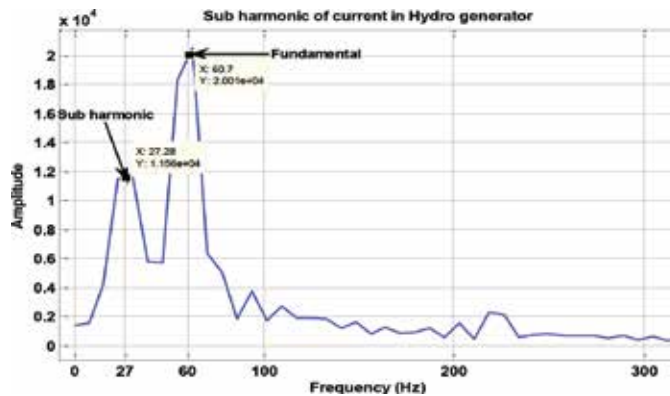


Figure 13.
 Frequency spectrum of current of generator in Grand Rapids station.

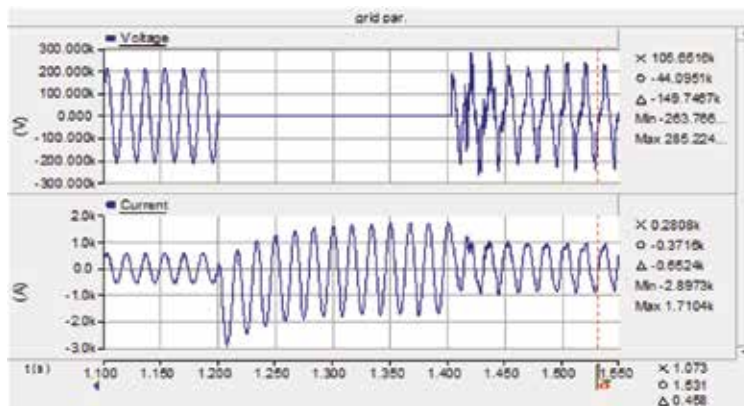


Figure 14.
 Grid parameters during short circuit in noncompensated system.

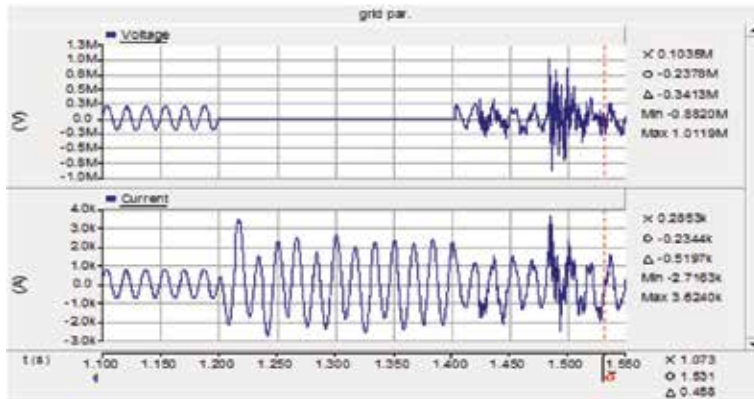


Figure 15.
Grid parameters during short circuit in series-compensated system.

Grand Rapids station is in generator mode. Current in hydro generator stator in Grand Rapids station consists of subharmonic 27 with a value of about 50% (Figure 13). This is f_{er} , which is generated by the network elements at the instance of short circuit. f_{er} is induced in the generator rotor and generates $f_r = 60 - 27 = 33$ Hz. The slip frequency of f_r coincides with natural frequency (Figure 12, mode 3) of rotor shaft in Grand Rapids station.

Figures 14 and 15 compare impact of series compensation on grid parameters with respect to noncompensated line during short circuit. As shown in Figure 14

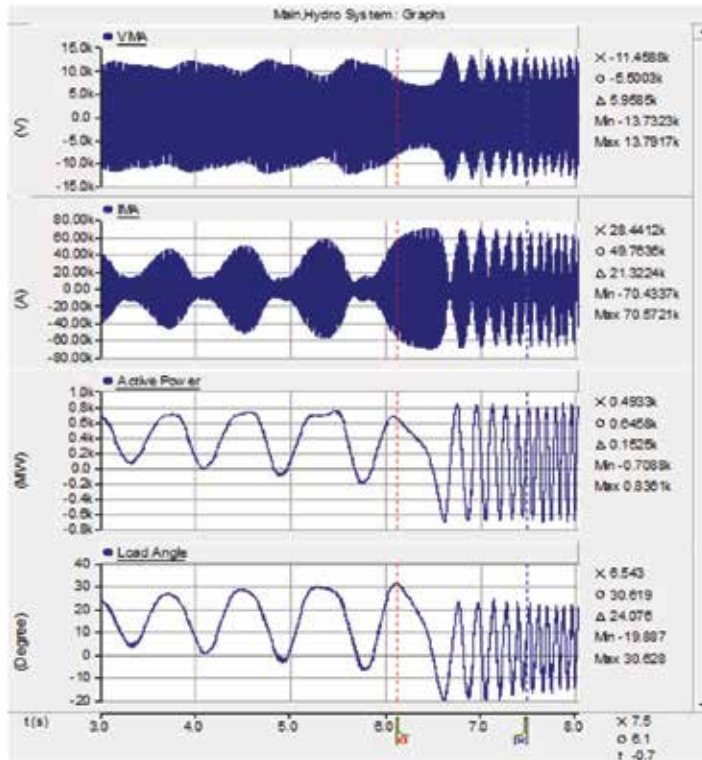


Figure 16.
Electrical parameters of hydro generator during SSR.

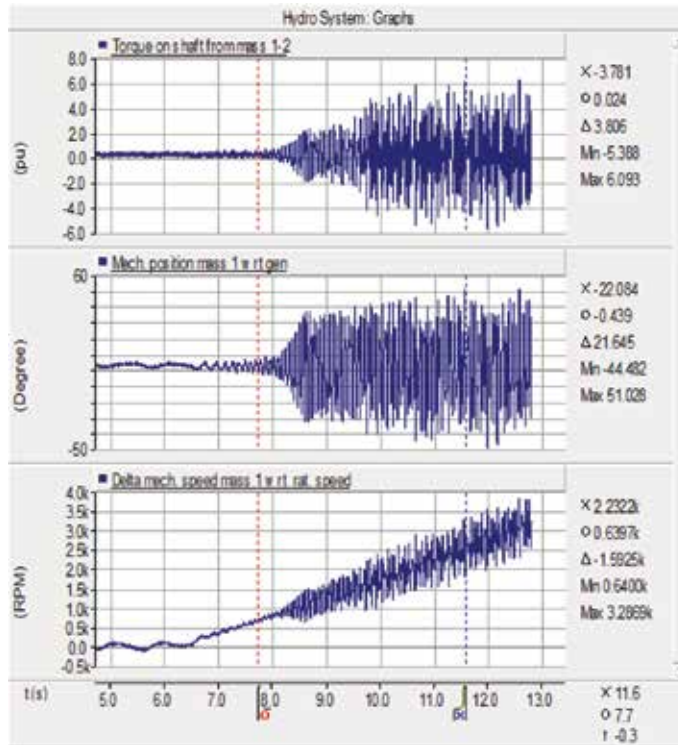


Figure 17.
 Mechanical parameters of hydro generator during SSR.

(noncompensation), voltage increases up to $285 \text{ kV}_{\text{pick}}$ in two periods and suppresses immediately. Current includes DC component, which is decayed gradually. In **Figure 15**, (series compensation) voltage increases up to $1 \text{ MV}_{\text{pick}}$. It causes saturation of transformer core and occurrence of ferroresonance. Current waveform is misshaped and includes subharmonics, which flow in the network. Electrical parameters of hydro generator are shown in **Figure 16**. Active power and load angle increase and oscillate along with increasing and oscillation of voltage and current after removing the fault and power oscillation begins with a frequency of about 1.5 Hz. Envelope of current grows up to 2.66 times greater than nominal current. As shown in **Figure 17**, oscillation of active power in Grand Rapids station causes increasing and oscillation of mechanical parameters of the hydro generator. Torsional strength from turbine to generator increases significantly in the time after 9 s. Direction of torque on the shaft and mechanical displacement between turbine to generator changes alternatively and increases at the same time. In addition, speed of the masses increases significantly with respect to rated speed.

Author details

Salman Rezaei
Kerman Power Generation Management Company, Kerman, Iran

*Address all correspondence to: rezaiesalman@gmail.com

IntechOpen

© 2019 The Author(s). Licensee IntechOpen. This chapter is distributed under the terms of the Creative Commons Attribution License (<http://creativecommons.org/licenses/by/3.0>), which permits unrestricted use, distribution, and reproduction in any medium, provided the original work is properly cited. 

References

- [1] Boucherot P. Éxistence de deux régimes en ferorésonance. *Rev. Gen. de L'Éclairage Électrique*. 1920;**8**(24): 827-828
- [2] Ferracci P. Ferroresonance-Cahier Technique Schneider no. 190; Groupe Schneider; 1998
- [3] Valverde V, Buigues G, Mazón AJ, Zamora I, Albizu I. Ferroresonant configurations in power systems. In: *International Conference on Renewable Energies and Power Quality (ICREPQ'12)*; 28-30 March 2012, Santiago de Compostela, Spain. 2012
- [4] Jacobson DAN, Lehn Peter W, Menzies W. Robert: Stability domain calculations of period-1 ferroresonance in a nonlinear resonant circuit. *IEEE Transactions on Power Delivery*. 2002; **17**(3):865-871
- [5] Kováč M, Eleschová Ž, Heretík P, Koniček M. Analysis and mitigation of ferroresonant oscillations in power system. *Proceedings of the 15th International Scientific Conference on Electric Power Engineering (EPE)*. 2014. pp. 211-216
- [6] Jacobson DAN. Field testing, modeling, and analysis of ferroresonance in a high voltage power system [Ph.D. dissertation]. Dept. elect. and comp. Eng., Univ. Manitoba; 2000
- [7] Scott LH. A case study of ferroresonance in a CCVT secondary circuit and its impact on protective relaying. In: *WPRC*; 17-19 October 2006; Spokane, Washington. 2006
- [8] Jacobson DAN, Menzies RW. Investigation of station service transformer ferroresonance in Manitoba Hydro's 230 kV Dorsey Converter Station. In: *Proc. IPST conf. Rio de Janeiro*; 2001
- [9] Rezaei S. Impact of plant outage on ferroresonance and mal operation of differential protection in presence of SVC in electrical network. *IET Generation, Transmission and Distribution*. 2017;**11**(7):1671-1682
- [10] Karaagac U, Mahseredjian J, Cai L. Ferroresonance conditions in wind parks. *Electric Power Systems Research*. 2016;**38**:41-49
- [11] Siahpoosh MK, Dorrel D, Li L, Ferroresonance assessment in a case study wind farm with 8 units of 2 MVA DFIG wind turbines. *20th International Conference on Electrical Machines and Systems (ICEMS)*. 2017. pp. 1-5
- [12] Rezaei S. Impact of ferroresonance on protective relays in Manitoba hydro 230 kV electrical network. In: *Proc. IEEE 15th Int. Conf. on Environment and Electrical Engineering*. Rome, Italy; 2015. pp. 1694-1699
- [13] Ballance JW, Goldberg S. Sub synchronous resonance in series compensated transmission lines. *IEEE Transactions on Power Apparatus and Systems*. 1973;**PAS-92**:1649-1658
- [14] Varghese M, Wu FF, Varaiya P. Bifurcations associated with sub-synchronous resonance. *IEEE Transactions on Power Systems*. 1998; **13**(1):139-144
- [15] Gupta S, Moharana A, Varma RK. Frequency scanning study of sub-synchronous resonance in power systems. In: *26th IEEE Canadian Conference on Electrical and Computer Engineering (CCECE)*. 2013. pp. 1-6
- [16] Nagabhushana; Chandrasekharaiah BS, Lai LL, Vujatovic D. Neural network approach to identification and control of sub-synchronous resonance in series compensated systems. In: *Proceedings of the IEEE Int. Conf. on Power Electronics and Drive Systems. PEDS '99*. Vol. 2. 1999. pp. 683-687

- [17] Yousif N, Al-Dabbagh M. Time-frequency distribution application for sub-synchronous resonance analysis in power systems. In: International Power Engineering Conference. Vol. 2. 2005. pp. 771-775
- [18] Khalilinia H, Ghaisari J. Improve sub-synchronous resonance (SSR) damping using a STATCOM in the transformer bus. In: IEEE EUROCON. 2009. pp. 445-450
- [19] Umre BS, Helonde JB, Modak JP, Renkey S. Application of gate-controlled series capacitors (GCSC) for reducing stresses due to sub-synchronous resonance in turbine-generator shaft. In: IEEE Energy Conversion Congress and Exposition. 2010. pp. 2300-2305
- [20] Lak A, Nazarpour D, Ghahramani H. Novel methods with fuzzy logic and ANFIS controller based SVC for damping sub-synchronous resonance and low-frequency power oscillation. In: 20th Iranian Conference on Electrical Engineering (ICEE2012). 2012. pp. 450-455
- [21] Mohammad pour HA, Santi E. Sub-synchronous resonance analysis in DFIG-based wind farms: Definitions and problem identification—Part I. In: IEEE Energy Conversion Congress and Exposition (ECCE). 2014. pp. 812-819
- [22] Mohammad pour HA, Santi E. Optimal adaptive sub-synchronous resonance damping controller for a series-compensated doubly-fed induction generator-based wind farm. IET Renewable Power Generation. 2015; **9**(6):669-681
- [23] Gagnon R, Viarouge P, Sybille G, Tourkhani E. Identification of ferroresonance as the cause of SVC instability in a degraded series compensated network. In: IEEE Power Engineering Society Winter Meeting. Vol. 2. 2000. pp. 1377-1382
- [24] Woodford DA. Solving the ferroresonance problem when compensating a Dc converter station with a series capacitor. IEEE Transactions on Power Systems. 1996; **11**(3):1325-1331
- [25] Anderson PM, Agrawal BL, Van Ness JE. Sub synchronous resonance in power systems. In: IEEE PES Book. 1926. p. 9
- [26] Leon AE, Solsona JA. Sub synchronous interaction damping control for DFIG wind turbines. IEEE Transactions on Power Systems. 2015; **30**(1):419-428
- [27] EMTP works version 2.0.2, examples, Ferro-Demo, Data case given by Jacobson DAN
- [28] Jacobson DAN. Examples of ferroresonance in a high voltage power system. In: Proc. IEEE PES General Meeting. 2003. pp. 1206-1212
- [29] Walker DN, Bowler CEJ, Jackson RL, Hodges DA. Results of subsynchronous resonance test at Mohave. IEEE Transactions on Power Apparatus and Systems. 1975;**94**(5):1878-1889
- [30] Tweedie R, Abrams HW. Electrical features of the 1590 MW coal-slurry-supplied Mohave generating station. IEEE Transactions on Power Apparatus and Systems. 1971;**PAS 90**(2):725-735
- [31] Rezaei S. Impact of sub synchronous resonance on operation of protective relays and prevention method. In: IEEE/IAS 53rd Industrial and Commercial Power Systems Technical Conference (I&CPS); 2017; Niagara Falls, ON, Canada. 2017. pp. 1-9
- [32] Rezaei S. An adaptive algorithm based on sub harmonic and time domain analysis to prevent mal operation of overcurrent relay during sub synchronous resonance. IEEE Transactions on Industry Applications. 2018;**54**(3):2085-2096

Effects of Climate Change in Electric Power Infrastructures

Daniel Burillo

Abstract

Climate change mitigation and adaptation has been a major driving force to modernize electric power infrastructure and include more renewable energy systems. This chapter explains several ways in which electric power infrastructure has contributed to climate change, how climate change affects electric power infrastructure, mitigation options, and adaptation options. Electricity infrastructure categories include power generation technologies, transmission lines, substations, and building loads. Climate change categories include atmospheric greenhouse gas concentration levels, rising sea levels, changes in precipitation patterns and river flows, as well as more extreme air temperatures. Specific quantitative case studies are provided to estimate vulnerabilities from heat waves in the US desert southwest, including long-term forecasting of infrastructure performance, as well as, various supply-side and demand-side strategic options to maintain reliable operations.

Keywords: climate change, risk management, demand forecast, load volatility, vulnerability, failure prediction, outage prediction, long-term planning

1. Introduction

Climate change occurs because of both natural and human causes. A geographic area that has a particular prevailing weather condition is said to have a particular climate [1, 2]. Over the course of time, earth has gone through several global climate changes, including the asteroid that killed the dinosaurs [3], the ice ages, and the warm period that we are in now [4]. Specific regions of the earth have also gone through local climate changes due to large storms, earthquakes, and volcanic eruptions that mostly only affect the target locations [5, 6]. Since human civilizations started intelligently designing ecosystems by channeling water, doing agriculture, building cities, and so on—we have been intentionally, and sometimes unintentionally, changing climates as well.

Civilization arguably did not start contributing to climate change at a global scale until after the industrial revolution with the proliferation of coal-powered steam engines and the burning of fossil fuels into the air [7]. The portable energy transformation device was revolutionary; the abundance with which humans lived and moved increased dramatically. Then, in 1896, Swedish chemist Svante Arrhenius estimated that the long-term effects of coal burning would enhance the natural greenhouse effect, and that a doubling of carbon dioxide in the atmosphere would warm the earth a few degrees Celsius. Modern-day climate models have maintained Arrhenius's conclusion, and only added more specifics to the predictions, with

details such as less average freezing at the earth's poles, higher sea level, more forceful storms, and various different weather patterns in particular geographies [8, 9]. Oil spills, trash barges, mass pavement, deforestation, various air-borne pollutants, and so on have also affected earth's ecosystems and climates [10].

Climate change is now affecting infrastructure systems by changing the weather conditions in which they must operate. The United States Department of Homeland Security has defined 16 critical infrastructure sectors that are considered vital to the "security, national economic security, and national public health or safety" of the country [11]. These critical infrastructure sectors are: chemicals, commercial facilities, communications, critical manufacturing, dams, defense, emergency services, energy, financial services, food and agriculture, government facilities, healthcare and public health, information technology, nuclear, transportation, and water and wastewater systems [11]. Across these infrastructure sectors, climate change will impact physical assets, operations, and use [12, 13]. As public awareness of the risks of climate change has risen, vulnerability assessments and adaption planning studies have been rapidly emerging in recent years too [13–16].

Climate is typically considered in infrastructure system designs by using several years' recent weather conditions to specify tolerances. This can be problematic for two reasons. First, because weather is not exactly the same every year, and more robust hardware is typically costlier, investors are often faced with tough risk management problems for low-probability high-impact events. Second, climates are changing. Thanks to advancements in global climate modeling, researchers are now able to forecast changes in future climate conditions and plan for extreme weather conditions with higher confidence. Climate change assessments generally rely on scenarios standardized by the Intergovernmental Panel on Climate Change (IPCC) [17]; however other considerations are made as well for factors such as the anthropogenic change in urban environments [18, 19]. The IPCC standard scenarios are referred to as Representative Concentration Pathways (RCPs), and are numbered corresponding to the amount of radiation forcing increase from the sun associated with the greenhouse gas effect relative to pre-industrial times, for example, RCP 4.5 and RCP 8.5 (4.5 and 8.5 W/m²) [20, 21].

The newest technological advancements in climate change modeling and long-term weather forecasting include high-resolution spatial projections based on "downscaling" techniques. These downscaling techniques aim to improve the geographic and temporal resolution of specific weather projections, including air temperature, wind speed, solar radiation, precipitation, snowpack, and hydrology for specific geographic regions [22–27]. However, challenges still exist in incorporating climate change data into practice [28–30]. These challenges range from a lack of understanding of what parameters to use in complex models, to the methods used in the models, to what to do about the results. Significant literature is emerging to disentangle the contribution of different mechanisms to the response patterns, yielding more transparent models and results [31]. Further solutions to these challenges are expected to be met through ongoing collaboration between climate scientists and engineers, which we have included examples for in this chapter for electricity infrastructure and heat waves.

2. Electricity infrastructure vulnerabilities to climate change

Electric power infrastructure broadly consists of three systems: generation, delivery, and demand. In terms of the physical processes, electrical power is created by generators to meet demand via delivery hardware. In terms of functionality however, it is the demand for electric power that drives the development of the

other two systems. Reliable electric power is central to urban development, and is a critical service in modern cities as almost all other major infrastructure and services rely on it: commerce, communication, manufacturing, defense, emergency, finance, agriculture, healthcare, information technology, transportation, and water [32]. Climate change can affect energy trade over time in ways that are significant to economics and natural resource consumption. For example, more extreme summer and winter temperatures necessarily result in more demand for cooling and heating, respectively. Climate change can also affect electric service reliability. A shortage of electric power generation, or sequence of faults in the delivery network, can result in an interruption in service at any second. This is why generation and delivery systems are built with multiple redundancies, such that individual component outages can occur safely. Unless there are multiple simultaneous outages, the infrastructure system can still deliver power to buildings and other loads without an interruption in service. **Table 1** provides a summary of major climate variables and their associated impacts on the power sector, adapted from [33].

Generation is vulnerable to flooding, reduced streamflow, warmer water, and warmer air temperatures, which can all cause a shortage of power supply in the system [34]. There are many ways to physically generate electric power, but to evaluate the effects of climate change we have chosen to broadly categorize them as those that use water, and those that do not as follows. Conventional hydroelectric and water-cooled turbine generators (e.g., nuclear, coal-fired, and some natural gas) use water, and so are vulnerable to changes in three ways. First, flooding can damage physical hardware of above and below ground equipment if that hardware is not sufficiently shielded [35]. For example, sea level is projected to rise by 1–1.4 m by the end of the century, and if that is the case, then 25 coastal plants in California will be at risk of flooding during 1-in-100 year high-tide events [36]. Second, if the water levels in natural sources are too low (e.g., low river flow during droughts), then production capacity can be dependent upon priority level in access rights or reduced to zero if the water level physically goes below the intake pipe [37]. Third, some once-through generators are vulnerable to increases in water temperature in coastal plants, as a certain amount of temperature rise is necessary to cool the generators. Environmental regulations prevent expelling of water that is too hot to be safe for the ecosystem [38]. In August of 2015, the Pilgrim Nuclear Power Station in Massachusetts cut its power because the temperature of sea water used as influent was too high [39]. Power generators that do not use water include dry combustion natural gas and solar photovoltaics. These types of “dry” power generators are generally inland and could be at risk of flooding if they are located in a basin-like landscape that would collect water from a storm. Dry power generators also operate less efficiently under higher ambient air temperatures, which mean they also have lower production capacity to meet peak demand [40]. Dry generators are also vulnerable to changes in humidity that can affect their air circulation systems, as well as flooding and storm-gusty winds in general [33].

Delivery systems can be affected by climate change due to higher temperatures causing higher demand, reduced capacity, and congestion; wildfires that can render power lines inoperable due to ionized air; and large storms that can cause physical damage via flooding and high winds that make trees fall on lines [41]. Delivery systems physically consist of various types of power lines that transport energy, transformers which convert the power to different voltage levels, quality devices for efficiency and reliability, and protection devices that interrupt power flows during hazardous conditions. Climate change can cause failures via physical hardware damage or create operational conditions that exceed hardware tolerances. Higher temperatures can cause individual components to become inoperable because protection devices will cut them off if power flow is too high for the weather

Climate hazard	Key impacts	Impacted segment	Adaptation strategies
Increased air temperatures	<ul style="list-style-type: none"> • Lower generation efficiency • Decreased coal-to-gas conversion efficiency • Decreased combined cycle gas turbine efficiency • Decreased solar PV efficiency 	Generation	<ul style="list-style-type: none"> • Implement air chillers or more efficient chillers • Site new generation in cooler locations
	<ul style="list-style-type: none"> • Reduced carrying capacity of lines and transformers • Increased losses in lines and transformers 	Delivery-Transmission & Distribution	<ul style="list-style-type: none"> • Underground hardware • Use more heat-resistant materials • Implement more effective cooling for transformers
	<ul style="list-style-type: none"> • Increased peak demand and total energy demand for cooling 	Demand-End Use	<ul style="list-style-type: none"> • AC energy efficiency • Building thermal efficiency • Peak load shifting
Increase in precipitation	<ul style="list-style-type: none"> • Reduced combustion efficiency due to increased moisture content of coal 	Generation	<ul style="list-style-type: none"> • Protect coal stockpiles • Switch to fuel that is more moisture resistant (e.g., natural gas)
	<ul style="list-style-type: none"> • Damaged power lines from snow and ice • Flooding of underground infrastructure • Damaged towers due to erosion 	Delivery-Transmission & Distribution	<ul style="list-style-type: none"> • Improved flood protection for equipment at ground level • Use covered and/or insulated conductors • Include lightning protection (e.g., earth wires, spark gaps) in the distribution network
Decrease in precipitation	<ul style="list-style-type: none"> • Decreased availability of freshwater for thermal cooling 	Generation	<ul style="list-style-type: none"> • Switch to recirculating or dry cooling • Switch to more “water-efficient” fuels (e.g., natural gas, wind, solar) • Increase volume of water treatment system • Restore/reforest land
Sea level rise/increased storm surge during hurricanes and tropical storms/increased nuisance flooding during high tides	<ul style="list-style-type: none"> • Flooding/damage to coastal/low-lying infrastructure 	Generation/delivery-Transmission and Distribution Demand-End use	<ul style="list-style-type: none"> • Implement flood control (dams, dikes, reservoirs, polders, etc.) • Improve coastal defenses (seawalls, bulkheads, etc.) • Build in and/or relocate to less exposed locations • Raise structure levels • Improved drainage systems • Protect fuel storage

Climate hazard	Key impacts	Impacted segment	Adaptation strategies
More frequent/severe extreme events (floods, typhoons, drought, high winds, etc.)	<ul style="list-style-type: none"> • Damaged infrastructure • Disrupted supply chains and offshore activity • Damage to facilities related to soil erosion 	Generation Delivery-Transmission and Distribution	<ul style="list-style-type: none"> • Same as above • Concrete-sided buildings instead of metal • Implement more rigorous structural standards • Implement porous materials for better wind flow • Increased decentralized energy generation • Cite infrastructure away from heavily wooded areas/rigorously prune trees

Table 1.
Summary of key climate drivers and possible impacts to power systems.

conditions [42]. Additionally, higher temperatures can result in reduced capacity for above ground power lines to safely carry electricity. If too many components are offline or the capacity of the system is significantly reduced, then power may not be available when it is needed causing cascading failures and blackouts as happened in the US in 2003 and 2011 [43, 44]. Alternatively, if protection devices are not properly calibrated, then components can overheat. This has happened to hundreds of distribution-level transformers during recent record breaking heat waves in the US southwest [45]. Moreover, lines can sag to the point that they permanently deform. Not coincidentally, during these record-breaking heat waves, the air is very dry, and the risk of wildfires is high. If wildfires burn under power lines, then those components can fail as well due to air ionization. Like generators, substations are vulnerable to rising sea levels and storm floods near the coast and in basin-like land areas [36]. Flooding can erode or short the hardware in substations and underground power lines [33]. Lastly, severe storms can blow trees, and other things, into power lines and cause outages.

Electric power demand is primarily susceptible to higher air temperatures, which can increase both total energy consumption and the peak demand in regions with significant electric air conditioning [40, 46, 47]. Demand is typically planned for at city- and state-level geographies based on seasonal weather usage patterns, daily weather usage patterns, and local use patterns. In warm to hot climates, the peak electricity demand is usually in the late afternoon during the summer when businesses are still operating and people are coming home and turning on air conditioners [48]. Historically, preparing for higher peak demand means building additional generation and delivery capacity, but policies aimed at natural resource conservation have targeted building and appliance energy efficiency standards which also offset increases in peak demand [40]. In terms of climate change, higher average temperatures and higher maximum temperatures mean more demand for AC usage, which could mean more energy usage over time, higher power demand for ACs to operate at hotter temperatures, and more installations of ACs total in moderately warm climates. The combined effects could be a significant increase in per capita demand [40]. This may be more than local delivery infrastructure are capable of supporting without systemic or network-wide investments [49].

3. How heat waves can result in service interruptions

The fault tree in **Figure 1** shows the terminal event of a service interruption on the right, and the power- and material/hardware-based-failures that can lead to a service interruption logically proceeding from the left [50]. Hardware failures feed-back into the event triggers as their loss of functionality results in a loss of power-flow that could cause an interruption. System operators generally maintain an $n - 1$ redundancy standard in design at the high-voltage transmission level meaning that the single largest generator, transmission line branch, or substation can fail

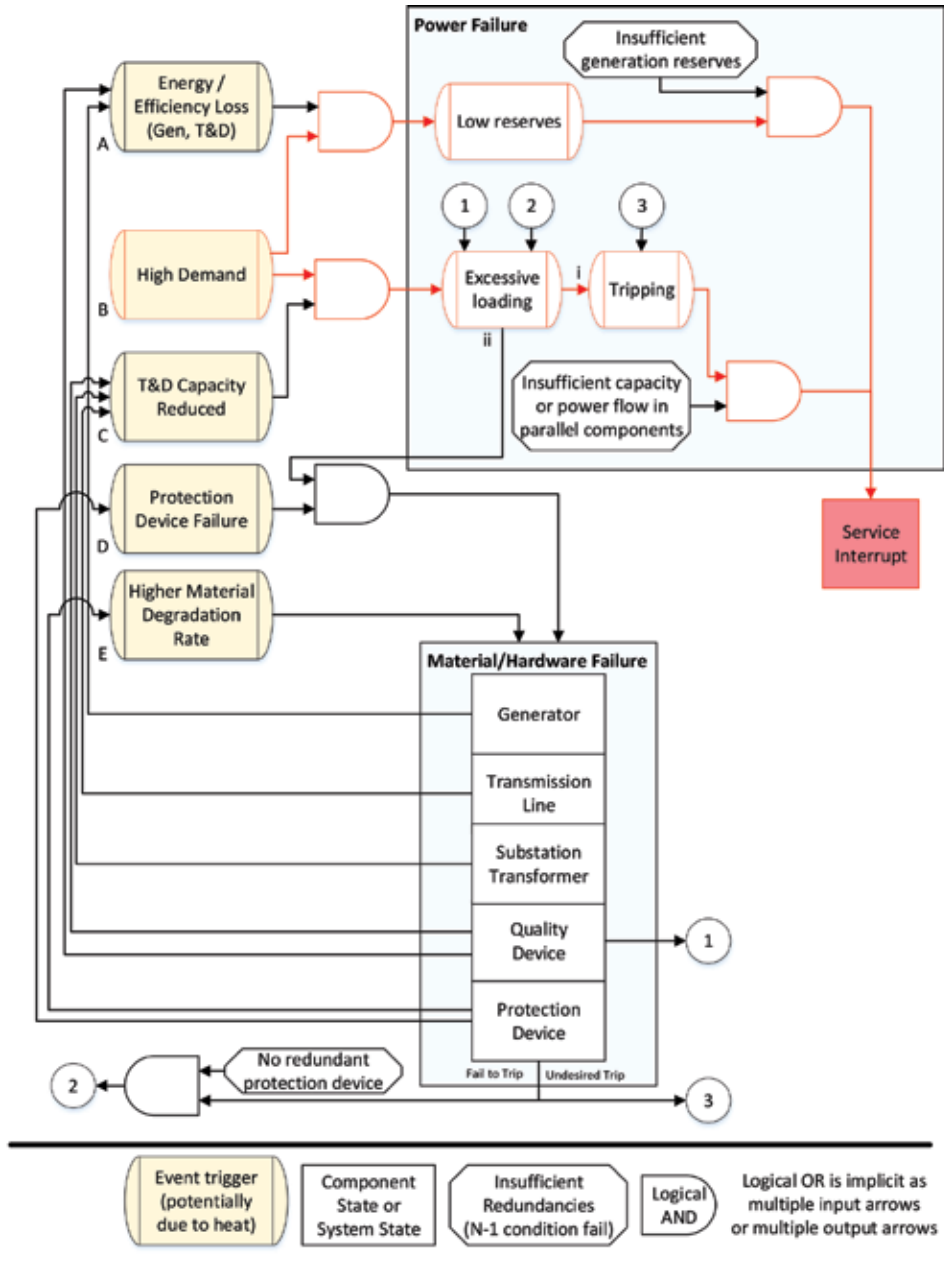


Figure 1. Fault tree from heat wave to service interruption.

at any time without any interruption in service [51]. These $n - 1$ redundancies are represented by octagon boxes and logical AND gates in the figure. Service interruptions due to major component failures only occur when more than one individual component fails at the same time. Such events can lead to cascading failures including blackouts as in the 2011 Arizona-California blackout [52]. The pathway for high demand is colored red because it is a critical condition for a service interruption in a system protected with multiple redundancies.

The two ways that a service interruption can occur as a function of purely rising air temperatures are that there is either not enough total generation to meet total demand, or particular power lines and substations do not have sufficient capacity to deliver power to loads. The following list explains how increases in ambient air temperatures can trigger failures leading to service interruptions consistent with the lettering in **Figure 1**.

- a. High air temperatures can result in loss of generation capacity and loss of efficiency in the transmission and distribution (T&D) network [36, 53]. If the system is also in high demand, (B), then load can exceed generation. If there are insufficient generation reserves, then there will be a service interruption.
- b. High air temperatures can result in higher demand, especially during the already hot summer months due to increased burden on building air conditioning systems [53].
- c. High air temperatures result in less capacity in T&D lines and transformers [36, 53]. If a circuit is in high demand, then power flow can result in components' temperatures exceeding safe operating temperatures [52].
 - i. If protection devices function correctly, then they will trip (open) the circuit under excessive loading and power flow will be instantaneously redistributed to parallel T&D components [52]. If there is insufficient capacity in parallel branches to deliver power to the load, then there will be a service interruption [52].
 - ii. If a protection device fails to trip and a circuit is over loaded, then excess heat accelerates the chemical degradation rate of sensitive materials and can result in mechanical failure (E) [54, 55]. Protection devices can fail because they are not accurately designed or calibrated for local climate conditions or other reasons [56]. Depending on the type and location of overload failure, a generator, transmission line, substation, quality device, or other protection device can fail. If a generator fails, then the system state goes to (A) as the system now has less generation. If a line or transformer fails, then the system goes to (C) as the T&D network operates at lower efficiency and or has less power flow capacity. If a power quality device fails, then it goes to (A) or (C) again or directly to excessive loading depending on the circumstances. If another redundant protection device fails, then the cycle of potential failures repeats for additional components on connected circuits.
- d. High air temperatures can result in a protection device failing to trip [56]. The device could be calibrated to a certain power rating that should be lower for the actual air temperature. If that occurs during high loading, then a component can become overloaded and fail as in (ii).
- e. High air temperatures can result in an accelerated physical material degradation rate, which can result in accelerated failures for any electrical devices [57]. The

same failure scenarios can occur as described above, with the addition of an undesired trip of a protection device. If a protection device fails with an undesired trip, and there is no redundant power flow, then a service interruption occurs.

4. Case study 1: quick estimate of peak demand for record-breaking heat waves

How can we know how much electricity demand there will be if weather conditions are more severe than they have ever been in the past? With no past records, how can we know what the future will be? How do we know if there will be sufficient generation resources to meet the demand? These are not straightforward questions to answer as demand and generation are, at the city scale, rather complicated with millions of moving parts. In this case study, adapted from Burillo et al. [40], we show how analysts can produce a reasonable city-scale predictive model using basic computational tools, and simple publicly available data for buildings, electricity demand, and air temperature.

We will consider Phoenix, Arizona and Los Angeles, California as regions because they have summertime peak demands with significant air conditioner (AC) penetration, and are expected to have higher air temperatures in the future with climate change [58–60]. A simple approach to predicting peak demand for future temperatures would be to plot daily peak electricity demand against daily maximum air temperatures, T_{max} , and draw a straight line, but doing so would be an oversimplification as it results in an overestimate of demand. Overestimating peak demand would be very costly from a planning perspective because it would inflate delivery capacity and resource adequacy requirements. Instead, we are going to use regression techniques to fit the structural equation model (SEM) developed in [40] using the number of residential and commercial utility customers, daily peak demand data for those customers, the air conditioning penetration percent from the county assessor's office, and daily T_{max} .

A full explanation of the theory and equations are in [40], but the concept in brief has two main parts as follows. First, at a micro-scale, as outdoor thermal forces (sunlight and air temperature) increase, the work that individual ACs do increases and so does their electrical load. In our prior study, we found that the most common AC units (split indoor-outdoor dry air-cooled) have an increase in active load of 1.33% kW per $1^{\circ}\text{C} \pm 0.35\%$. Second, at a macro scale, AC duty cycles increase proportional to the ratio of incoming and outgoing building thermal energy at the thermostat set point. At higher T_{max} , the number of ACs simultaneously active in a region during the peak period increases as well up to a theoretical limit of 100%. This behavior can be effectively modeled in the form of an s-curve.

The results for the peak demand SEM are shown in **Figure 2** compared to a straight-line approach. Peak demand in Phoenix is more sensitive to average historical seasonal changes in air temperatures than Los Angeles, but results show that *marginal* changes in peak demand are more significant in Los Angeles than in Phoenix at summertime highs. Peak demand for Phoenix increased more in its historical range because its 90th percentile, T_{90} , was relatively higher, and Phoenix has higher AC penetration. From historical T_{90} to the highest projected T_{max} however, peak demand increased more in Los Angeles than Phoenix, another 3.9 GW vs. 1.2 GW or 34 vs. 16%. In this case, the larger increase in peak demand in Los Angeles was due to the larger relative difference between historical T_{90} and future T_{max} . As shown in **Figure 2b**, Phoenix's ACs expect to already be running at nearly 100% duty cycle at its T_{90} , whereas Los Angeles's ACs expect to only run at about 60% duty cycle at its T_{90} . Thus, the potential for a record-breaking heat wave to affect peak demand is higher in Los Angeles than Phoenix.

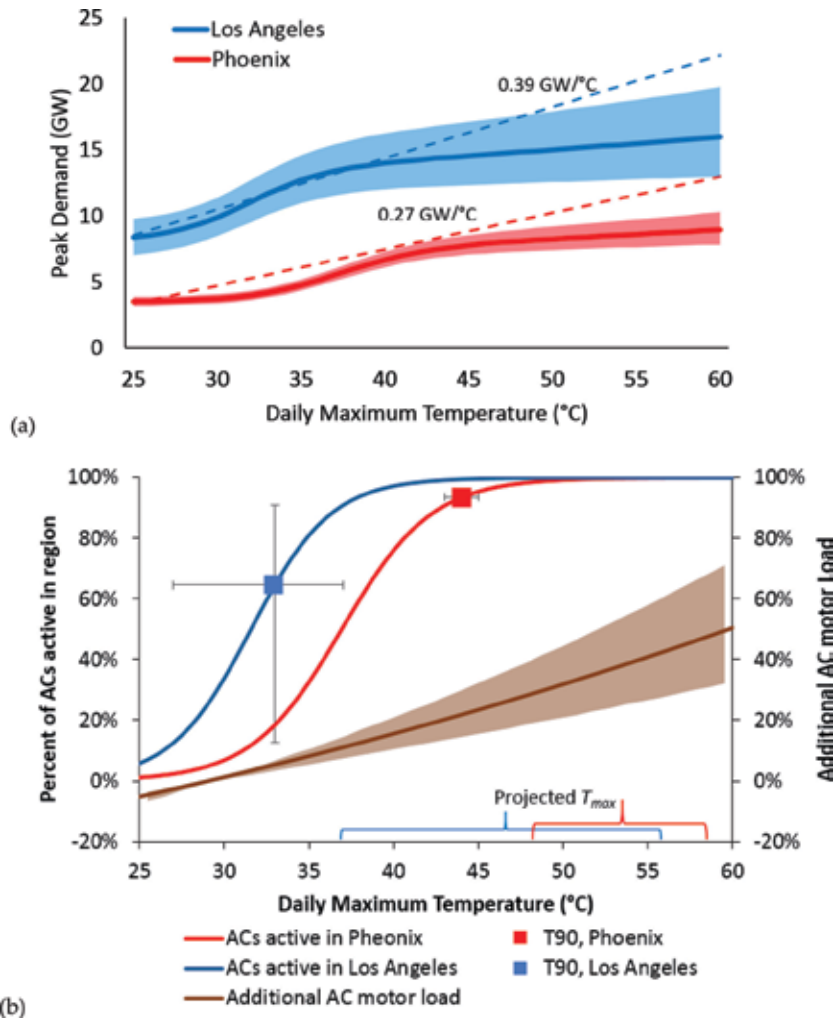


Figure 2. (a) Peak demand. (b) Peak demand SEM factors. (a) Shows SEM approach results in solids. Straight-line approach shown in dotted lines. (b) Shows the two s-curved lines are expected values. T₉₀ ranges represent the range of 90th percentile values for the locations sampled.

5. Case study 2: using downscaled climate data to inform long-term demand forecasts and capital infrastructure planning

While city-scale blackouts often make for bigger headlines in the news, neighborhood-scale outages are much more common. In the last case study, we saw how forecasting peak electricity demand was critical for planning generation resource capacity, and how those efforts could be enhanced with better quantitative understanding of climate change. In this case study, based on [61], we incorporate climate change projections at the next level in electricity infrastructure planning and consider the highly complex problem of siting and sizing delivery component capacities.

It is not enough to simply have generation resources in the same city as loads. There must also be lines, substations, and transformers to get the power from the generators to the users, and each of those have their own capacities which are a function of how hot the devices can safely operate at. Where and how should we build immovable field assets with 30–70-year useable life spans? How do we know what the urban landscape,

the buildings, the appliance technology, the population, and so on will look like that far into the future? Doing this well is a highly coordinated effort with many steps and iterations across multiple planning departments, as we shall get a taste for below.

If we are going to attempt to model a map of the future infrastructure requirements with any accuracy, then first we need a model that produces an accurate map of current conditions. The full details of our approach are described in Ref. [61], and the concept at brief is as follows. We used high-resolution (2 km²) data for daily maximum ambient air temperatures (T_{max}), residential and commercial building models calibrated for the region, a geographic map of the buildings' locations, and a geographic map of lines and substations. With these tools and data we are able to validate a map of the base period (2010) electric power demand and infrastructure loading in Los Angeles County, California as shown in **Figure 3**.

With a reasonably accurate and verified model of base period electricity demand, and initial loading on delivery hardware, we can use historical climate data to estimate overloading risks in the base period. We do this by re-running our models with the composite image of the highest temperature values that historically occurred in any location at any historical period in time. We also use that temperature image to estimate the reduced capacity on infrastructure hardware. Combining the two together, we can compute the thermally de-rated load factors on hardware as shown in **Figure 4** for substations with corresponding definitions in **Table 2**.

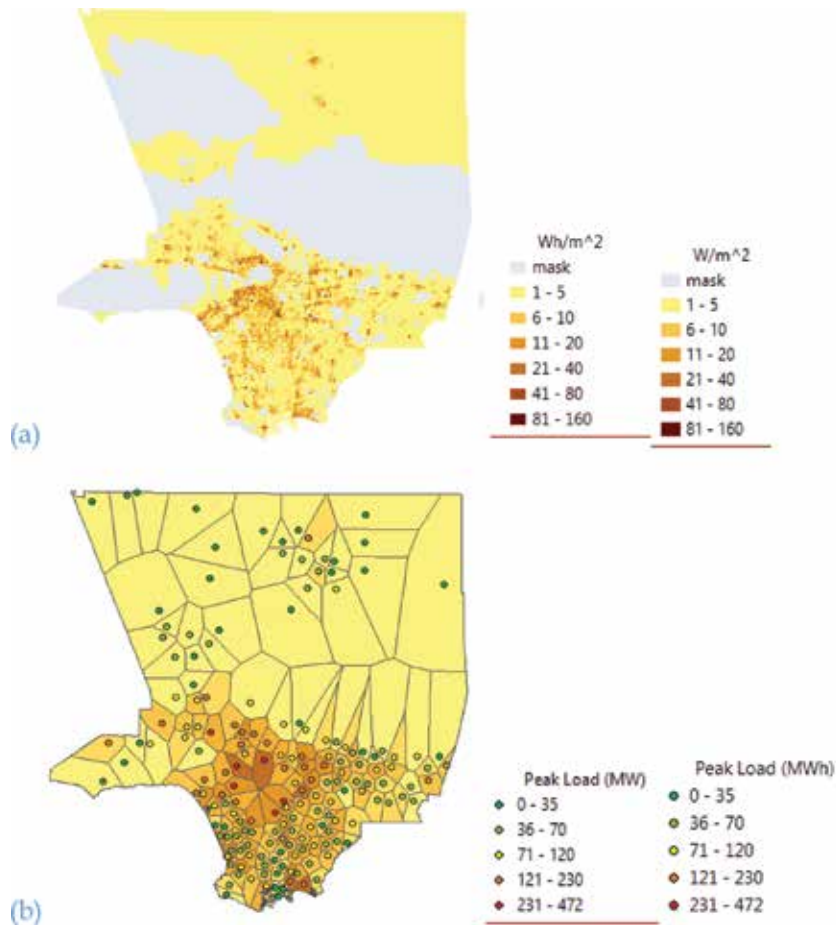


Figure 3. Map of Los Angeles County, California. (a) Peak demand and (b) substation loading in base period.

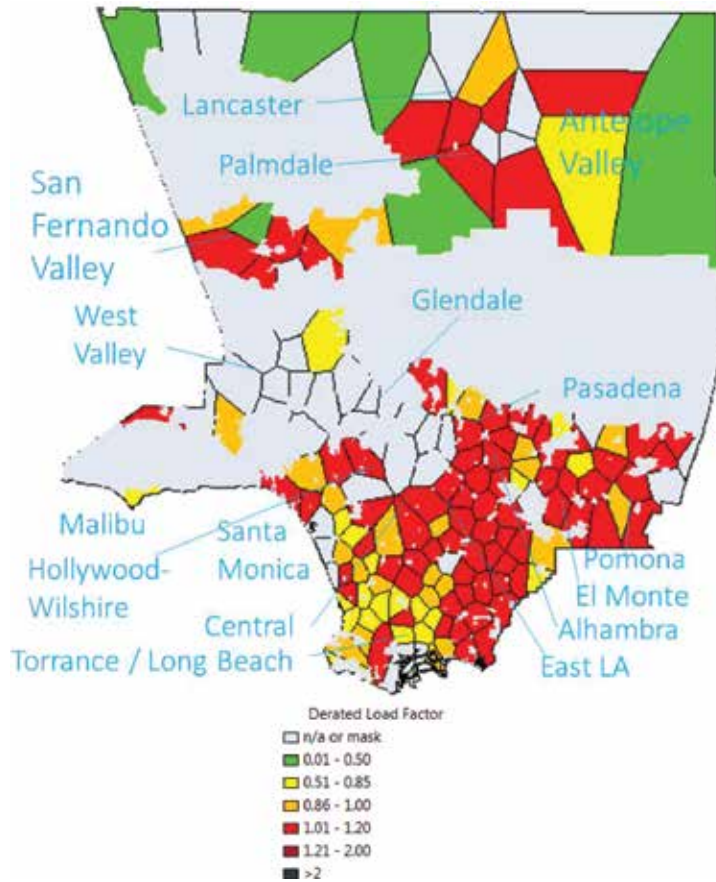


Figure 4.
 Map of Los Angeles County, California substations risks in base period.

Load factor	Risk level	Reference	Description
n/a	Unknown	n/a	Substation(s) exists in this space according to national database [1], but not shown in SCE DERiM [2], so load factor data were unavailable
0.01–0.5	Very safe	Assumption	Negligible thermal wear, probably n – 2 reliable if in parallel/redundant configuration
0.51–0.85	Safe	15% rule	Very low thermal wear, probably n – 1 reliable if in parallel/redundant configuration
0.86–1.00	Caution	15% rule	Some thermal wear, probably not n – 1 reliable
1.01–1.20	Warning	[3, 4]	Moderate thermal wear, component overloaded, automatic switching may occur within 24 h to 30 days if loading continues at this level depending upon switch gear settings
1.21–2.00	Emergency	[3, 4]	Significant thermal wear, component very overloaded, automatic switching may occur within 30 min depending upon switch gear settings
>2	Outage	[4]	Extreme thermal wear, switchgear will automatically trip to prevent combustion and permanent hardware damage

Table 2.
 Substation derated load factor risk metrics.

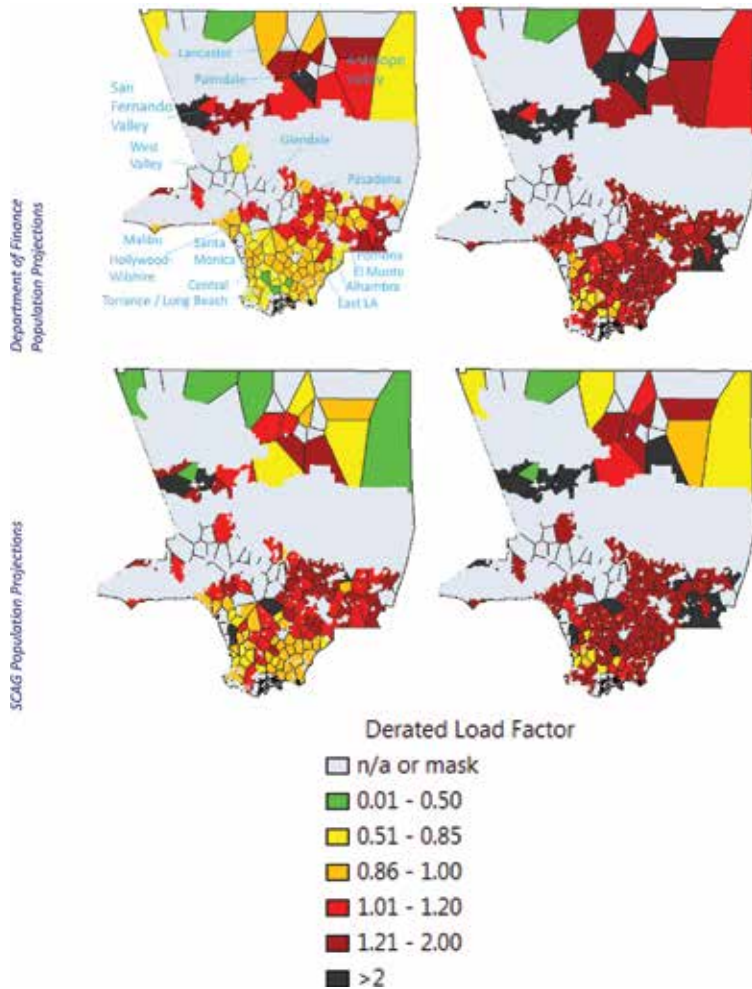


Figure 5.
Map of Substation Risks by 2060.

We can now forecast into the future for a variety of factors. In this case, we considered rising air temperatures, population growth, building stock turnover, housing densification, air conditioning penetration, and air conditioning efficiency. All of these factors were technically specified in either the building energy models or at the census block group in making spatial allocations to the maps. The results are shown for two population growth scenarios, and two energy efficiency scenarios for substation loading in **Figure 5**. This is what the peak hour could look like during a heat wave in 2060 with the same infrastructure as in the base period. Specific cities and neighborhoods are identified as being at risk of overloading and outages as shown in **Figure 5**.

6. Climate change risk mitigation and adaptation options in the electric power sector

There are many ways to maintain stability in electric power systems in light of climate change. Several mitigation and adaptation options are listed in **Figure 6** for our case studies of insufficient supply-side resources during rising air temperatures, with effects on stability and other factors important for consideration as well. We categorically consider several options in the form of technology implementations, market

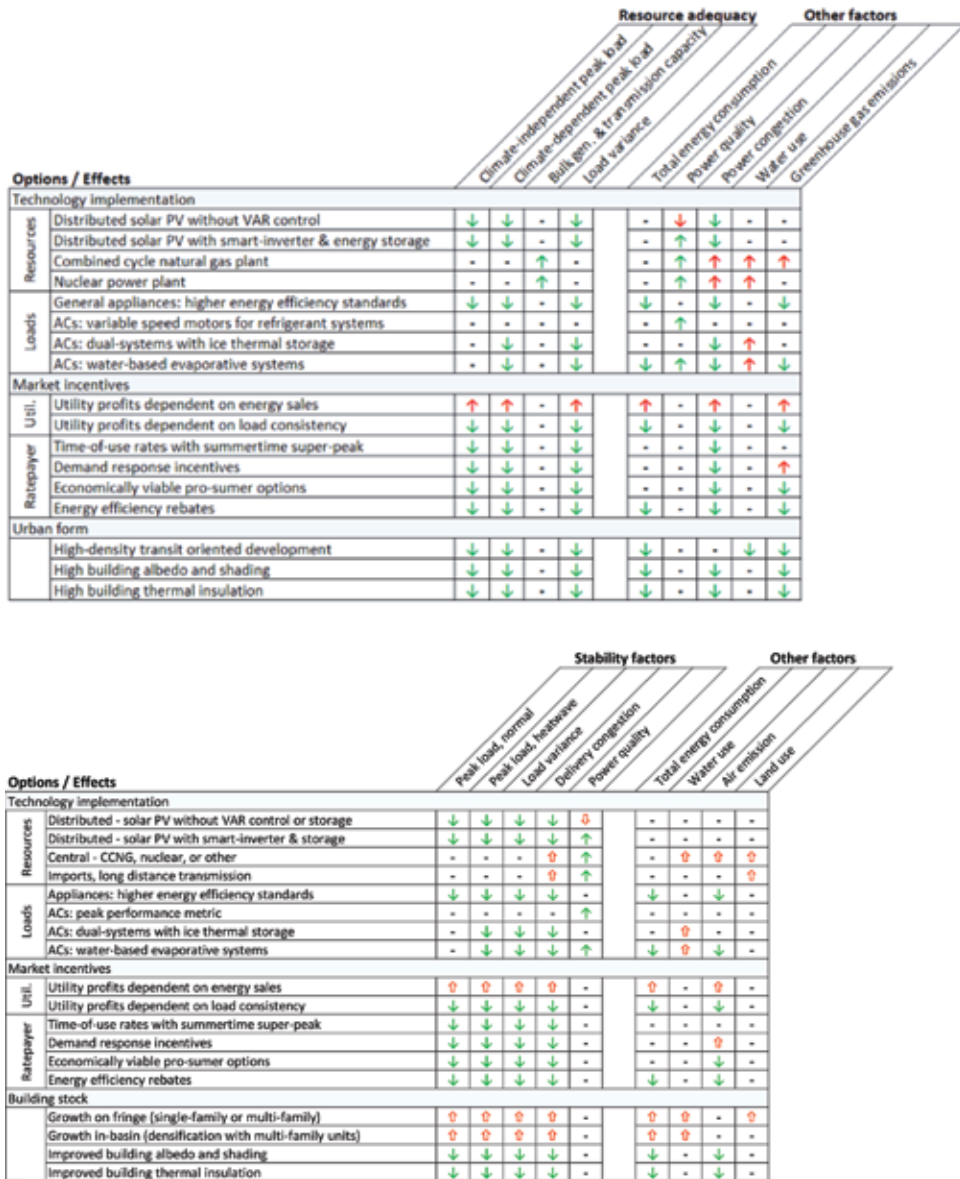


Figure 6. Climate change risk mitigation and adaptation options and effects.

incentives, and building stock. We consider load variance as an effect explicitly because less variance means more consistent load, more capacity for contingencies, and lower operations and maintenance costs [49]. We also identified effects of those options on several other complex interdependent factors that are priorities for stakeholders too. This discussion should not be considered exhaustive nor advocate any particular option, but simply present several options as we have identified so far in a structured manner.

6.1 Electrical systems: resources

The major tradeoffs between generation technologies—distributed solar PV (with storage and power quality controls) and centralized systems—in meeting demand are: land space requirements, delivery congestion relief, water usage, air

emissions, and marginal capital costs. Solar PV can be installed on building roofs, whereas centralized systems require their own dedicated land footprint and delivery infrastructure [62–65]. When implemented at the distribution level, solar PV can power load directly without going through delivery components that are necessary for central systems. The net effect is a relative decrease in load from the perspective of the grid relative to demand. Yet these distributed systems beg the question of storage given peak demand occurs once the PV systems decline in production of power. At the same time, this will be an important metric to monitor for reliability purposes going forward—if storage is included—as those two values have historically been one and the same. The most prominent fast-ramping central generation technology is combined cycle natural gas plants, which both consume water and emit various gasses into the atmosphere. Combustion-only natural gas plants could be implemented, which would not use water, but would be more sensitive to rising air temperatures, as well as less fuel-efficient, and therefore more costly and emissions intensive per kWh. While leveled costs of solar PV are now at or below parity with bulk generation plants on a per kWh basis, the combined costs of solar PV with storage to provide 24/7 dispatchable energy and regulation services are still higher than traditional central generation plants [66]. Thus, the best options for new resource procurement across competing objectives, will be those that consider the current and future state of the delivery infrastructure.

Implementing DER with new buildings may be the most cost-effective way to meet demand associated with growth in areas where delivery infrastructure are already over capacity during extreme heat waves. In such areas, some substations may be able to be adapted with improved heat sinks, forced air, or water cooling systems to increase capacity. But some may not, and overhead power line capacity will still be limited to convective cooling. The cost of increasing delivery infrastructure capacity necessary to meet demand through central generation, or long-distance imported power could be quite significant at \$10–130 million USD per substation and \$1–3 million USD per mile of line length leading all the way out of the urban center [67, 68].

Future work for vulnerable neighborhoods should consider implementation of adaptation options by considering 24-h load profiles on distribution-level circuits, the total Watt-hours of necessary storage capacity to complement solar PV capacity, and opportunity for network aggregation in supplying ancillary grid services. Circuits with higher portion of commercial and industrial loads may be preferable for the installation of DERs, as their load profiles may more closely match the PV generation profile (peaking at mid-day) allowing for more storage efficiency. Effective implementation of energy storage would reduce load variance by charging during off-peak hours and discharging during peak hours, resulting in a more consistent load, which is more readily manageable by system operators, and therefore has lower operations and maintenance costs [49]. This could occur through some kind of automated and networked market incentives that are available for wholesale markets as of February 2018 [69].

Implementation of new bulk generation systems and delivery infrastructure may be more valuable in the northern areas of San Fernando and Antelope Valley. The areas are relatively less developed there and so land should be more readily available for construction. Future studies should consider the reliability and security benefits of redundant central and distributed energy systems, and determine what amount of each, including storage, is optimal for different outage risk tolerances.

6.2 Electrical systems: loads

More energy efficient appliances can reduce use-phase load, load variance, and thus provide benefits to power systems' stability. To mitigate risks from heat waves

however, focus should be directed towards air conditioner units. Differences in lighting and other appliance efficiencies only affected peak demand in the models by 2% in California, but that state already has aggressive energy efficiency policies, so other areas around the world could benefit more. AC units generally accounted for 60–70% of summertime peak demand within residential buildings, and higher air temperatures resulted in a 3–7% increase in demand per 1°C (1.8°F). Los Angeles County currently has only 45% AC penetration in its residential buildings, meaning that peak demand in just over half of the current building stock does not increase with air temperature. By 2060 almost all buildings could have AC.

Policies that would guide new or replacement ACs based on different performance constraints or different technologies would aid in reducing the risk of excessive peak demand during extreme heat events. It is possible to design AC units that are more efficient under the hottest conditions or that utilize thermal storage to achieve ‘flat’ efficiency curves that do not degrade at the hottest temperatures [70, 71]. For example, developing a new ‘peak performance rating’ for ACs at 50°C (122°F) could be useful to mitigate peak load during extreme heat waves. Doing so could provide incentive for ACs to be optimally engineered for more efficient performance at or near such extreme temperatures. Current standards, SEER and EER [72], are primarily for temperatures at or below 35°C (95°F). The current SEER standard, SEER 13, is already optimized to the point that improvements in SEER ratings in the model up to SEER 21 only affected peak demand by a few percent and were slightly counter-effective in some instances where temperatures exceeded 45°C (113°F) due to tradeoffs in engineering design optimization. Water-based evaporative cooling systems are another option that uses much less electric power, but requires water to operate, and are often not accepted by users as the sole-source of air conditioning due to insufficient comfort levels when the weather is both hot and humid [73, 74]. Further study may be useful to identify the practicality of hybrid designs.

6.3 Market incentives: supply side and utilities

Some studies suggest that the traditional utility business model, that couples energy sales to profits, is not compatible with certain energy efficiency goals or large amounts of DER [85]. The former issue is because utility revenues are primarily dependent on total energy sales, but the costs of providing reliable infrastructure are primarily dependent on capital expenditures, operations, and maintenance [75]. Profits increase with volumetric energy sales, and costs are relatively flat. Therefore, financial incentives must exist to be relatively inefficient in some processes. Hence, public regulatory commissions exist to oversee the prices set for rate-payers. The alternative business model is referred to as a “decoupled” market, where “excess” profits are carried forward and accounted for in adjusting the following years’ prices [76, 77]. When utility profits are decoupled from energy sales, load serving entities can implement effective conservation programs without violating fiduciary responsibility to shareholders [78]. This structure has been implemented in several states with positive effects on energy efficiency. For example, California’s per-capita annual energy consumption has remained relatively flat since decoupling was implemented in the 1980s, whereas many other states’ has steadily risen [79]. Market design determines rules by which participants must play [80]. If utilities’ profits were a function of key reliability precursors, such as smaller load variance, then utilities would have a direct incentive to reduce peak load (including shifting it to off-peak hours), resulting in less congestion, higher utilization of lower-cost base-load bulk generation resources, and more contingency capacity for non-stationary extreme heat events.

6.4 Market incentives: demand side and ratepayers

One philosophy for evaluating public policy is to consider whether the rules are equitable, efficient, transparent, administratively simple, and support achieving greater policy goals [81]. Current retail electricity rate schedules in Los Angeles and Phoenix generally meet these criteria via monthly energy billing with tiered and time of use rates [82–85]. Charging residential ratepayers monthly based on total energy use is simple, transparent, equitable, and promotes energy efficiency. Higher electricity prices during peak hours helps to reduce peak load by incentivizing ratepayers to take action to shift flexible or non-critical usage to off-peak hours when electricity can be generated at lower cost [86]. Incentivizing ratepayers to turn off loads in the form of demand response relieves congestion on the grid; however, the majority of that relief comes from industrial customers who often switch to onsite diesel power or natural gas combined heat and power units [87]. Rebates are available in some localities for ratepayers to obtain solar PV, storage, or demand management technologies [88]. One-time rebates for building energy efficiency enhancements have also been found to reduce demand and peak load [89]. Overall, these incentives generally reflect the philosophy that electricity is both a critical infrastructure necessity and a non-critical commodity. Electricity is critical for powering infrastructure systems such as water, transportation, food, fuel, communications, and finance [32]. It is also critical in residential buildings for lighting, cooking, cleaning, and climate control.

6.5 Building stock

Population growth will increase peak demand, but where and by how much will be significantly influenced by decisions relating to the management of urban systems. Housing demand in less developed areas can be met through either single family or multi-family dwelling units. To meet population growth through densification however, most housing demand would need to be met through new multi-family dwelling. In addition to conserving land space, the benefits of building new multi-family unit residential housing can be as much as a 50% lower peak demand per capita than single-family detached units. Those benefits are due to reduced volume and shared walls, which significantly reduce exposure to extreme heat. In addition, street albedo and widths should be considered for urban heat island impacts.

7. Conclusions

Climate change is a broad term used to describe ecosystem disruptions that result in long-term changes in weather patterns. Industrial processes have had various impacts on ecosystems over time, and for the most part business peace treaties have been effective in the form of government regulations to limit climate-altering emissions that are harmful to human health. While electric power generation is not the only contributor to climate change, it has historically been a major one with various emissions regulations developed for the solid, liquid, and air-borne wastes of different processes. Carbon-dioxide emissions, once thought relatively harmless, are now understood to be the primary contributor to higher solar energy retention by the earth's atmosphere, and thus lower average annual ice formation, higher sea-levels, warmer air temperatures, and various related effects around the globe. As public understanding of the risks of climate change have increased in recent years, several advancements in technology, analytics, and regulations have been piloted

to reduce carbon emissions as well. Through advancements in weather forecasting tools, analysts are better able to characterize extreme weather conditions, and support electric power systems planning to forecast peak demand, resource adequacy requirements, delivery infrastructure capacity, and avoid outages during heat waves. While public understanding of the risks of climate change has increased, little knowledge exists of the value of low-cost energy available to the public nor the public risk of unstable power systems. As power systems around the world undergo transformation to lower-emissions technology standards, analysts can use the techniques demonstrated in this chapter to clearly define other risky climate conditions and support development of tools, regulations, and implementations that manage risks of other power stability issues in conjunction with climate change.

Acknowledgements

The content in this chapter was adapted from the published PhD dissertation of its author [90], which was supported by the California Energy Commission under grant number CEC EPC-15-007, Climate Change in Los Angeles County: Grid Vulnerability to Extreme Events, and the National Science Foundation under grant number 1360509, 2014-2017, Advancing Infrastructure and Institutional Resilience to Climate Change for Coupled Water-Energy Systems. Any opinions, findings, conclusions, or recommendations expressed in this material are those of the authors and do not necessarily reflect the views of the National Science Foundation or the California Energy Commission.

Conflict of interest


None.

Author details

Daniel Burillo
Independent Scholar, Glendale, Arizona, USA

*Address all correspondence to: danielbtb@gmail.com

IntechOpen

© 2018 The Author(s). Licensee IntechOpen. This chapter is distributed under the terms of the Creative Commons Attribution License (<http://creativecommons.org/licenses/by/3.0>), which permits unrestricted use, distribution, and reproduction in any medium, provided the original work is properly cited. 

References

- [1] California Energy Commission. The Pacific Energy Center's Guide to: California Climate Zones. 2006
- [2] Stewart ID, Oke TR. Local climate zones for urban temperature studies. *Bulletin of the American Meteorological Society*. 2012;**93**:1879-1900. DOI: 10.1175/BAMS-D-11-00019.1
- [3] Switek B. What Happened in the Seconds, Hours, Weeks After the Dino-Killing Asteroid Hit Earth? *Smithsonian*. 2016. <https://www.smithsonianmag.com/science-nature/what-happened-seconds-hours-weeks-after-dino-killing-asteroid-hit-earth-180960032/> [Accessed May 9, 2018]
- [4] Eldredge S, Biek B. Glad You Asked: Ice Ages—What are They and What Causes Them? *Utah Geological Survey*. 2010. <https://geology.utah.gov/map-pub/survey-notes/glad-you-asked/ice-ages-what-are-they-and-what-causes-them/> [Accessed May 9, 2018]
- [5] Crowley TJ. Causes of climate change over the past 1000 years. *Science*. 2000;**289**:270-278
- [6] Jaramillo E, Dugan JE, Hubbard DM, Melnick D, Manzano M, Duarte C, et al. Ecological implications of extreme events: Footprints of the 2010 earthquake along the Chilean Coast. *PLoS One*. 2012;**7**:e35348. DOI: 10.1371/journal.pone.0035348
- [7] Palermo E. Who invented the steam engine? *Live Science*. 2014. <https://www.livescience.com/44186-who-invented-the-steam-engine.html> [Accessed May 21, 2018]
- [8] Shukman D. A brief history of climate change. *BBC News*. 2018. <http://www.bbc.com/news/science-environment-15874560> [Accessed May 8, 2018]
- [9] Olah GA, Prakash GKS, Goepfert A. Anthropogenic chemical carbon cycle for a sustainable future. *American Chemical Society*. 2011;**133**:12881-12898. DOI: 10.1021/ja202642y
- [10] IPCC. Fifth Assessment Report—Climate Change. 2013:2013. <https://www.ipcc.ch/report/ar5/wg1/> [Accessed January 22, 2018]
- [11] Smith A. Presidential Policy Directive 21 Implementation. Department of Homeland Security. 2015. <https://www.dhs.gov/sites/default/files/publications/ISC-PPD-21-Implementation-White-Paper-2015-508.pdf> [Accessed January 1, 2017]
- [12] Melillo JM, Richmond TC, Yohe GW, editors. *Climate Change Impacts in the United States: The Third National Climate Assessment*. U.S; 2014. DOI: 10.7930/j0z31WJ2
- [13] Warren RF, Wilby RL, Brown K, Watkiss P, Betts RA, Murphy JM, et al. Advancing national climate change risk assessment to deliver national adaptation plans. *Philosophical Transactions of the Royal Society A: Mathematical, Physical and Engineering Sciences*. 2018;**376**(20170295). DOI: 10.1098/rsta.2017.0295
- [14] Carter JG, Handley J, Butlin T, Gill S. Adapting cities to climate change—Exploring the flood risk management role of green infrastructure landscapes. *Journal of Environmental Planning and Management*. 2017;**0568**:1-18. DOI: 10.1080/09640568.2017.1355777
- [15] Oh S, Kim K, Kim H. Investment decision for coastal urban development projects considering the impact of climate change: Case study of the Great Garuda Project in Indonesia. *Journal of Cleaner Production*. 2018;**178**:507-514. DOI: 10.1016/j.jclepro.2017.12.283

- [16] Lee JY, Ellingwood BR. A decision model for intergenerational life-cycle risk assessment of civil infrastructure exposed to hurricanes under climate change. *Reliability Engineering and System Safety*. 2017;**159**:100-107. DOI: 10.1016/j.res.2016.10.022
- [17] Kim K, Ha S, Kim H. Using real options for urban infrastructure adaptation under climate change. *Journal of Cleaner Production*. 2017;**143**:40-50. DOI: 10.1016/j.jclepro.2016.12.152
- [18] Hunt JCR, Aktas YD, Mahalov A, Moustauoui M, Salamanca F, Georgescu M. Climate change and growing megacities: hazards and vulnerability. *Proceedings of the Institution of Civil Engineers—Engineering Sustainability*. 2018;**171**:314-326. DOI: 10.1680/jensu.16.00068
- [19] Prestele R, Arneth A, Bondeau A, De Noblet-Ducoudré N, Pugh TAM, Sitch S, et al. Current challenges of implementing anthropogenic land-use and land-cover change in models contributing to climate change assessments. *Earth System Dynamics*. 2017;**8**:369-386. DOI: 10.5194/esd-8-369-2017
- [20] van Vuuren DP, Edmonds J, Kainuma M, Riahi K, Thomson A, Hibbard K, et al. The representative concentration pathways: An overview. *Climatic Change*. 2011;**109**:5-31. DOI: 10.1007/s10584-011-0148-z
- [21] Arora VK, Scinocca JF, Boer GJ, Christian JR, Denman KL, Flato GM, et al. Carbon emission limits required to satisfy future representative concentration pathways of greenhouse gases. *Geophysical Research Letters*. 2011;**38**:3-8. DOI: 10.1029/2010GL046270
- [22] Walton DB, Sun F, Hall A, Capps S. A hybrid dynamical-statistical downscaling technique. Part I: Development and validation of the technique. *Journal of Climate*. 2015;**28**:4597-4617. DOI: 10.1175/JCLI-D-14-00196.1
- [23] Sun F, Walton DB, Hall A. A hybrid dynamical-statistical downscaling technique. Part II: End-of-Century warming projections predict a new climate state in the Los Angeles region. *Journal of Climate*. 2015;**28**:4618-4636. DOI: 10.1175/JCLI-D-14-00197.1
- [24] Loikith PC, Waliser DE, Kim J, Ferraro R. Evaluation of cool season precipitation event characteristics over the Northeast US in a suite of downscaled climate model hindcasts. *Climate Dynamics*. 2018;**50**:3711-3727. DOI: 10.1007/s00382-017-3837-0
- [25] Ahmadalipour A, Moradkhani H, Svoboda M. Centennial drought outlook over the CONUS using NASA-NEX downscaled climate ensemble. *International Journal of Climatology*. 2017;**37**:2477-2491. DOI: 10.1002/joc.4859
- [26] Sanjay J, Krishnan R, Shrestha AB, Rajbhandari R, Ren GY. Downscaled climate change projections for the Hindu Kush Himalayan region using CORDEX South Asia regional climate models. *Advances in Climate Change Research*. 2017;**8**:185-198. DOI: 10.1016/j.accr.2017.08.003
- [27] Tian B, Lee H, Waliser DE, Ferraro R, Kim J, Case J, et al. Development of a model performance metric and its application to assess summer precipitation over the U.S. great plains in downscaled climate simulations. *Journal of Hydrometeorology*. 2017;**18**:2781-2799. DOI: 10.1175/JHM-D-17-0045.1
- [28] Douglas E, Jacobs J, Hayhoe K, Silka L, Daniel J, Collins M, et al. Progress and challenges in incorporating climate change information into transportation research and design. *Journal of Infrastructure Systems*. 2017;**23**. DOI:

04017018. DOI: 10.1061/(ASCE)
IS.1943-555X.0000377

[29] Weyant J. Some contributions of integrated assessment models of global climate change. *Review of Environmental Economics and Policy*. 2017;**11**:115-137. DOI: 10.1093/reep/rew018

[30] Pindyck RS. The use and misuse of models for climate policy. *Review of Environmental Economics and Policy*. 2017;**11**:100-114. DOI: 10.1093/reep/rew012

[31] Kröner N, Kotlarski S, Fischer E, Lüthi D, Zubler E, Schär C. Separating climate change signals into thermodynamic, lapse-rate and circulation effects: theory and application to the European summer climate. *Climate Dynamics*. 2017;**48**:3425-3440. DOI: 10.1007/s00382-016-3276-3

[32] Rinaldi SM, Peerenboom JP, Kelly TK. Identifying, understanding, and analyzing critical infrastructure interdependencies. *IEEE Control Systems Magazine*. 2001;**21**:11-25. DOI: 10.1109/37.969131

[33] Asian Development Bank. *Climate Risk and Adaptation in the Electric Power Sector*. Asian Development Bank; 2012

[34] Bartos M, Chester M. Impacts of climate change on electric power supply in the Western United States. *Nature Climate Change*. 2015;**5**:748-752. DOI: 10.1038/nclimate2648

[35] Hollnagel E, Fujita Y. The Fukushima disaster-systemic failures as the lack of resilience. *Nuclear Engineering and Technology*. 2013;**45**:13-20. DOI: 10.5516/NET.03.2011.078

[36] Sathaye JA, Dale LL, Larsen PH, Fitts GA, Koy K, Lewis SM, et al.

Estimating impacts of warming temperatures on California's electricity system. *Global Environmental Change*. 2013;**23**:499-511. DOI: 10.1016/j.gloenvcha.2012.12.005

[37] Wagman D. *Water Issues Challenge Power Generators*. 2013. <http://www.powermag.com/water-issues-challenge-power-generators/> [Accessed October 3, 2017]

[38] European Environment Agency. *Energy and Environment Report*. 2008:2008. DOI: 10.2800/10548

[39] Abel D. Pilgrim Nuclear Power Station in Plymouth to shut down by 2019—The Boston Globe. *Boston Globe*. 2015. <https://www.bostonglobe.com/metro/2015/10/13/entergy-close-pilgrim-nuclear-power-station-nuclear-power-plant-that-opened/fNeR4RT1BowMrFApb7DqQO/story.html> [Accessed December 3, 2017]

[40] Burillo D, Chester MV, Ruddell B, Johnson N. Electricity demand planning forecasts should consider climate non-stationarity to maintain reserve margins during heat waves. *Applied Energy*. 2017;**206**:267-277. DOI: 10.1016/j.apenergy.2017.08.141

[41] Campbell RJ. *Weather-Related Power Outages and Electric System Resiliency*. 2012

[42] IEEE Std C37.30.1-2011—IEEE Standard Requirements for AC High-Voltage Air Switches Rated Above 1000 V. 2012. DOI: 10.1109/IEEESTD.2012.6175995

[43] North American Electric Reliability Council. *Technical Analysis of the August 14, 2003, Blackout: What Happened, Why, and What Did We Learn?* Report. 2004

[44] FERC, NERC. *Arizona-Southern California Outages on September 8 2011*. 2012

- [45] Jerod MacDonald-Evoy. Power outages impact thousands around Arizona. Arizona Repub. 2016. <http://www.azcentral.com/story/news/local/ mesa-breaking/2016/06/05/1900-mesa-homes-lose-power-record-breaking-heat/85464650/>
- [46] Reyna JL, Chester MV, Wagner G, Wagner G, Kainuma M. Energy efficiency to reduce residential electricity and natural gas use under climate change. *Nature Communications*. 2017;**8**:14916. DOI: 10.1038/ncomms14916
- [47] Bartos M, Chester M, Johnson N, Gorman B, Eisenberg D, Linkov I, et al. Impacts of rising air temperatures on electric transmission ampacity and peak electricity load in the United States. *Environmental Research Letters*. 2016;**11**:114008. DOI: 10.1088/1748-9326/11/11/114008
- [48] EIA. U.S. Electric System Operating Data—Hourly. 2016. http://www.eia.gov/beta/realtime_grid/#/data/grap hs?end=20160916T00&start=20160909T00
- [49] Burillo D, Chester M, Ruddell B, Johnson N. Electricity demand planning forecasts should consider climate non-stationarity to maintain reserve margins during heat waves. *Applied Energy*. 2017;**206**. DOI: 10.1016/j.apenergy.2017.08.141
- [50] Willis HL, Welch GV, Schrieber RR. *Aging Power Delivery Infrastructures*. 1st ed. New York, NY: Marcel Dekker, Inc; 2001
- [51] Burillo D, Chester M, Ruddell B. Electric grid vulnerabilities to rising air temperatures in Arizona. *Procedia Engineering*. 2016;**145**:1346-1353. DOI: 10.1016/j.proeng.2016.04.173
- [52] Mistry J, Keel B. Guidelines For Electric System Planning. Oper Sect Plan Guidel Doc. 2013. http://www.oatioasis.com/SRP/SRPdocs/Guidelines_for_Electric_System_Planning_10_13.pdf [Accessed January 1, 2017]
- [53] Bartos M, Chester M. Supplementary information for “impacts of climate change on electric power supply in the western united states”. 2015
- [54] Wan H. Increasing thermal rating by risk analysis. *IEEE Transactions on Power Apparatus and Systems*. 1999;**14**:815-828. DOI: 10.1109/59.780891
- [55] Sen PK, Pansuwan S, Malmedal K, Martinoo O, Transformer Overloading SMG. Assessment of Loss-of-Life for Liquid-Filled Transformers. Tempe, AZ. 2011
- [56] North American Electric Reliability Corporation. State of Reliability. Atlanta, GA. 2013:2015
- [57] Denning R. Applied R&M Manual for Defence Systems. 2012. http://www.academia.edu/6628321/Applied_R_and_M_Manual_for_Defence_Systems_Part_C_-_R_and_M_Related_Techniques_CHAPTER_7_DERATING_CONTENT [Accessed January 1, 2017]
- [58] APS. Integrated Resource Plan. 2014:2014. http://www.oatioasis.com/AZPS/AZPSdocs/2014-04-01_Integrated_Resource_Plan.pdf [Accessed January 1, 2017]
- [59] US Census Bureau 2010 Census Interactive Population Map. 2017. <https://www.census.gov/2010census/popmap/> [Accessed June 14, 2017]
- [60] LADWP. Power Integrated Resource Plan. 2016
- [61] Burillo D, Chester M, Pincetl S, Fournier E, Reich K, Hall A. Climate Change in Los Angeles County: Grid Vulnerability to Extreme Heat.

California's Fourth Climate Change Assessment. California Energy Commission. Publication number: CCCA4-CEC-2018-013. 2018

[62] Carrasco JM, Franquelo LG, Bialasiewicz JT, Member S, Galván E, Guisado RCP, et al. Power-electronic systems for the grid integration of renewable energy sources: A survey. *IEEE*. 2006;**53**:1002-1016

[63] Ochoa LF, Harrison GP. Minimizing energy losses: Optimal accommodation and smart operation of renewable distributed generation. *IEEE*. 2011;**26**:198-205. DOI: 10.1109/TPWRS.2010.2049036

[64] Bridge G, Bouzarovski S, Bradshaw M, Eyre N. Geographies of energy transition: Space, place and the low-carbon economy. *Energy Policy*. 2013;**53**:331-340. DOI: 10.1016/j.enpol.2012.10.066

[65] Fthenakis V, Chul H. Land use and electricity generation: A life-cycle analysis. *Renewable and Sustainable Energy Reviews*. 2009;**13**:1465-1474. DOI: 10.1016/j.rser.2008.09.017

[66] Penn I. California invested heavily in solar power. Now there's so much that other states are sometimes paid to take it. *Los Angeles Times*. 2017. <http://www.latimes.com/projects/la-fi-electricity-solar/> [Accessed February 15, 2018]

[67] PG&E. Final PG&E Generator Interconnection Unit Cost Guide. 2012. https://www.pge.com/pge_global/common/pdfs/for-our-business-partners/interconnection-renewables/Unit-Cost-Guide.pdf [Accessed January 1, 2017]

[68] Mason T, Curry T, Wilson D. Capital Costs for Transmission and Substation Recommendations for WECC Transmission Expansion Planning. WECC. 2012. https://www.wecc.biz/Reliability/1210_BV_WECC_

[TransCostReport_Final.pdf](#) [Accessed February 27, 2018]

[69] St. John J. FERC Allows Energy Storage to Play in Nationwide Wholesale Markets. 2018. https://www.greentechmedia.com/amp/article/ferc-energy-storage-wholesale-markets?__twitter_impression=true [Accessed February 21, 2018]

[70] Ruddell BL, Salamanca F, Mahalov A. Reducing a semiarid city's peak electrical demand using distributed cold thermal energy storage. *Applied Energy*. 2014;**134**:35-44. DOI: 10.1016/j.apenergy.2014.07.096

[71] Bush J, Ruddell B. Field Testing an Ice Storage Air Conditioner in Phoenix, Arizona. In: EPRI. 2015

[72] SCE. EER & SEER As Predictors of Seasonal Cooling Performance. South Calif Edison Des Eng Serv. 2003. <http://doe2.com/Download/DEER/SEER%2BProgThermostats/EER-SEER Overview.pdf>

[73] Kumar S, Mathur J, Mathur S, Singh MK, Loftness V. An adaptive approach to define thermal comfort zones on psychrometric chart for naturally ventilated buildings in composite climate of India. *Building and Environment*. 2016;**109**:135-153. DOI: 10.1016/j.buildenv.2016.09.023

[74] Parsons K. Human Thermal Environments—The Effects of Hot, Moderate, and Cold Environments on Human Health, Comfort and Performance. 2nd ed. New York, NY: Taylor and Francis; 2003. DOI: 10.1201/b16750

[75] Grabel MH. Utility Rate Cases: The Indiser's Perspective, Arizona Energy Futures Conference; 2016. pp. 1-14

[76] (CPUC). California's Next Step Decoupling "Plus". 2016. <http://www.fishnick.com/pge/>

Decoupling_Explained.pdf [Accessed October 20, 2016]

[77] PG&E. How PG&E Makes Money. 2016. https://www.pge.com/en_US/residential/rate-plans/how-rates-work/learn-how-rates-are-set/how-pge-makes-money/how-pge-makes-money.page? [Accessed October 21, 2016]

[78] Bhatti M. From consumers to prosumers: Housing for a sustainable future. *Housing Studies*. 1993;8:98-108. DOI: 10.1080/02673039308720753

[79] Wang D. California is Proof that Energy Efficiency Works | Greentech Media. Green Tech Media. 2013. <https://www.greentechmedia.com/articles/read/California-Is-Proof-That-Energy-Efficiency-Works> [Accessed October 21, 2016]

[80] Brijs T, De Jonghe C, Hobbs BF, Belmans R. Interactions between the design of short-term electricity markets in the CWE region and power system flexibility. *Applied Energy*. 2017;195:36-51. DOI: 10.1016/j.apenergy.2017.03.026

[81] Lave LB. Improving the management of environmental health. *Environmental Health Perspectives*. 1985;62:359-363

[82] APS. Residential Rate Plans. 2017. <https://www.aps.com/en/ourcompany/ratesregulationsresources/serviceplaninformation/Pages/residential-sheets.aspx> [Accessed March 15, 2017]

[83] SRP. Residential Price Plans. 2017. <https://www.srpnet.com/menu/electricres/priceplans.aspx> [Accessed March 15, 2017]

[84] LADWP. Electric Rate Schedules. 2016. <https://ladwp.com/ladwp/faces/ladwp/aboutus/a-financesandreports/a-fr-electricrates/a-fr-er-electricrateschedules;jsessionid=v7vPYKqTKr3hMPFJps1Y8hGyTXvcLLmKQyhK3L>

2MMbJNgRQJ5Khy!545368516?_adf.ctrl-state=cs0kc1rp1_4&_afrLoop=268583008846984&_afrWindowMode [Accessed March 15, 2017]

[85] SCE. Residential Rates | Rates & Pricing Choices | SCE Tariff Books | Regulatory Information | Home—SCE. 2017. [Accessed March 15, 2017]

[86] Albadi MH, El-Saadany EF. A summary of demand response in electricity markets. *Electric Power Systems Research*. 2008;78:1989-1996. DOI: 10.1016/j.epr.2008.04.002

[87] Aghaei J, Alizadeh MI. Demand response in smart electricity grids equipped with renewable energy sources: A review. *Renewable and Sustainable Energy Reviews*. 2013;18:64-72. DOI: 10.1016/j.rser.2012.09.019

[88] NC Clean Energy Technology Center. Database of State Incentives for Renewables & Efficiency—DSIRE. 2017. <http://www.dsireusa.org/> [Accessed March 1, 2017]

[89] Greening LA, Greene DL, Difiglio C. Energy efficiency and consumption—The rebound effect—A survey. *Energy Policy*. 2000;28:389-401. DOI: 10.1016/S0301-4215(00)00021-5

[90] Burillo D, Chester M, Ruddell B. Electric Power Infrastructure Vulnerabilities to Heat Waves from Climate Change. In: Arizona State University. 2018

Edited by Kenneth Eloghene Okedu

The target readers for this book are academics and engineers working in universities, research institutes and industry sectors wishing to enhance their knowledge about power system stability. Readers of this book should gain technical ideas and special experience with detailed information about small signal stability, dynamics, modeling, power oscillations and electrical power infrastructures relating to power system stability. The contents of this book provide many solutions to problems that can be integrated into larger research findings and projects. The book addresses some power system stability studies such as an overview of power systems and stability criteria, applications of the trajectory sensitivity theory to small signal stability, power system small signal stability in grid connected smart park, power system dynamics and modeling. The book also describes some recent developments in power oscillations due to ferroresonance, sub synchronous resonance and effects of climate change in electric power infrastructures.

Published in London, UK

© 2019 IntechOpen
© Nenov / iStock

IntechOpen

